Wastewater Electrolysis Cell for Environmental Pollutants Degradation and Molecular Hydrogen Generation

Thesis by

Kangwoo Cho

In Partial Fulfillment of the Requirements

for the degree of

Doctor of Philosophy

CALIFORNIA INSTITUTE OF TECHNOLOGY

Pasadena, California

2015

(Defended August 28, 2014)

Dedicated to…

my lovely wife Soojeon

ACKNOWLEDGEMENTS

When I took some coffee breaks with friendly squirrels on campus, I used to imagine the moment I write this section, and that moment is now in front of me. Over the last four years of my graduate study in Caltech, I feel myself getting solid both in theory and experiments with respect to environmental chemistry and energy science. I was sincerely happy and watched my enthusiasm soar as I plowed through these fields. My experience of Caltech deeply encouraged me to devote my entire carrier to enhancing the science and technology for environments. I would like to express my gratitude to a number of people who have helped me to get through the Environmental Science and Engineering PhD program at Caltech

First of all, my foremost gratitude should be given to my academic advisor, Professor Michael R. Hoffmann. Without a doubt, he would be the world's best advisor if the *Times Higher Education* compiled a ranking for advisors. Professor Hoffmann has given me a lot of freedom and inspiration to discover my own path of research. He has been always supportive and encouraged me with excessive compliments which were often more than I deserved. Among many other virtues as a mentor, I have to point out his valuable comments stemming from his boundless knowledge on a variety of topics in environmental science, as well as his friendship and kind consideration for my personal life in Pasadena. Prof. Hoffmann allowed me numerous opportunities to teach graduate level classes and to participate in conferences, which definitely cultivated my academic abilities. I also wish to thank the committee members for my qualification exam, candidacy exam, and thesis defense, which include Prof. William A. Goddard III, Prof. John H. Seinfeld, Prof. Mitchio Okumura, Prof. Jess F. Adkins, Prof. Paul O. Wennberg, and Prof. Jared Renton Leadbetter.

It was my great honor to make team efforts with the former, current, and future Hoffmann Group members. I enjoyed collaborating with the 'Gates Team', specifically Daejung Kwon, Dr. Yan Qu, Dr. Pei Xiong, Dr. Su Young Ryu, Clement Cid, Cody Finke, Asghar Aryanfar, Dr. Penvipha Satsanarukkit, and many others. The field experience in India will be especially unforgettable. I believe they will continue to devote their efforts to enhance livability in developing worlds. I was lucky to get helpful advice from visiting professors Prof. Wonyong Choi, Dr. Kyung-Guen Song, Prof. Kwhang-Ho Choo, Prof. Hyunwoong Park, and Prof. Jungwon Kim. It was my pleasure to work with visiting students Jieun Shin, Joycie Jiao, Hanspeter Zöllig, and many others. Novel and penetrating comments by Dr. A. J. Colussi were always impressive during the group meeting. Many thanks are due to Dr. Nathan Dalleska for technical support at the Environmental Analysis Center and Dr. Tae-Kyu Lee in Nano-Pac for the collaboration in preparation of electrodes and reactor systems. My thanks to office mates Rifka Kameel, Francesca Riboni, Dr. Himanshu Mishra, and colleagues Dr. Yi Zhang, Dr. Dr. Yubao Zhao, and many others.

I also want to acknowledge the Bill and Melinda Gates Foundation for the financial support for this study and DOW Chemicals for recognizing my work with the 2012 SISCA award. I owed my graduate study to many people in the Korea Institute of Science and Technology, including Dr. Kyu-Hong Ahn, Dr. Seockheon Lee, Dr. Kyung-Guen Song, and Dr. Seok Won Hong.

Finally, I would like to thank my wife Soojeon Yoo for always being next to me. My parents and parents-in-law gave us constant support and bore the long-distance trip to visit us. None of my academic progress and happy life in Pasadena would have been possible without my family.

ABSTRACT

This study proposes a wastewater electrolysis cell (WEC) for on-site treatment of human waste coupled with decentralized molecular H_2 production. The core of the WEC includes mixed metal oxides anodes functionalized with bismuth doped TiO_2 (BiO_x/TiO_2). The BiO_x/TiO_2 anode shows reliable electro-catalytic activity to oxidize Cl^- to reactive chlorine species (RCS), which degrades environmental pollutants including chemical oxygen demand (COD), protein, NH_4^+, urea, and total coliforms. The WEC experiments for treatment of various kinds of synthetic and real wastewater demonstrate sufficient water quality of effluent for reuse for toilet flushing and environmental purposes. Cathodic reduction of water and proton on stainless steel cathodes produced molecular H_2 with moderate levels of current and energy efficiency. This thesis presents a comprehensive environmental analysis together with kinetic models to provide an in-depth understanding of reaction pathways mediated by the RCS and the effects of key operating parameters. The latter part of this thesis is dedicated to bilayer hetero-junction anodes which show enhanced generation efficiency of RCS and long-term stability.

Chapter 2 describes the reaction pathway and kinetics of urea degradation mediated by electrochemically generated RCS. The urea oxidation involves chloramines and chlorinated urea as reaction intermediates, for which the mass/charge balance analysis reveals that N_2 and CO_2 are the primary products. Chapter 3 investigates direct-current and photovoltaic powered WEC for domestic wastewater treatment, while Chapter 4 demonstrates the feasibility of the WEC to treat model septic tank effluents. The results in Chapter 2 and 3 corroborate the active roles of chlorine radicals ($Cl\cdot/Cl_2^{-}\cdot$) based on *iR*-compensated anodic

potential (thermodynamic basis) and enhanced pseudo-first-order rate constants (kinetic basis). The effects of operating parameters (anodic potential and [Cl^-] in Chapter 3; influent dilution and anaerobic pretreatment in Chapter 4) on the rate and current/energy efficiency of pollutants degradation and H_2 production are thoroughly discussed based on robust kinetic models. Chapter 5 reports the generation of RCS on $Ir_{0.7}Ta_{0.3}O_y/Bi_xTi_{1-x}O_z$ hetero-junction anodes with enhanced rate, current efficiency, and long-term stability compared to the $Ir_{0.7}Ta_{0.3}O_y$ anode. The effects of surficial Bi concentration are interrogated, focusing on relative distributions between surface-bound hydroxyl radical and higher oxide.

TABLE OF CONTENTS

LIST OF FIGURES

LIST OF TABLES

Chapter 1

INTRODUCTION

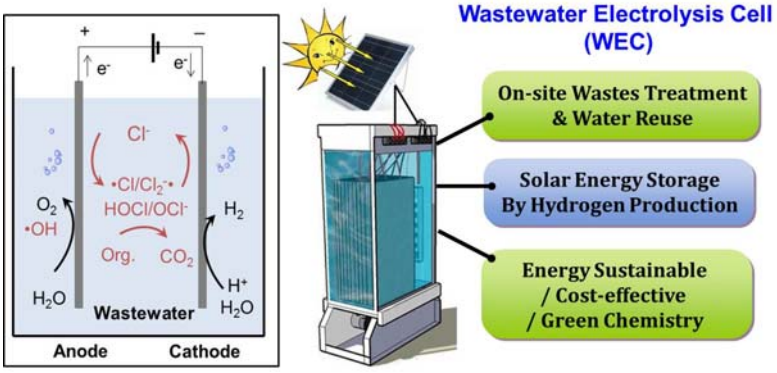

1.1. HUMAN NEEDS

Current world water crisis manifests that more than 2.5 billion people worldwide lack access to improved sanitation and waste disposal facilities, most often in developing areas such as South Asia, Indonesia and Africa.[1] In these emerging countries, human waste and open defecation are major sources of waterborne diseases. The biochemical oxygen demand (BOD) from human waste discharge into receiving waters is becoming a threat to biodiversity.[2] Consequently, there have been growing demands for research and development to find breakthroughs in on-site wastewater treatment and water reuse technologies. When considering the deficiency of underground infrastructures, water treatment and reuse practices suitable to use in the developing world should be self-contained with reduced consumptions of water, energy, and capital costs.[3,4] Even in the developed world, a growing need for sustainability and water treatment capacity along with an increase in population density has forced water treatment criteria more stringent in order to enhance livability and water use efficiency.[5] Corresponding demands for reduction in the total maximum daily loads of pollutants also drive towards on-site wastewater treatment practices due to difficulties in building or retrofitting a centralized wastewater treatment plant.[4]

On the other hand, extensive efforts are underway to develop renewable energy sources with negligible carbon footprints. Electrochemical water splitting is often used for the production of molecular hydrogen via alkaline and solid oxide electrolysis that have current efficiencies for a hydrogen production up to 67%.[6] The dominant fraction of the hydrogen production cost is coming from the electricity consumption and partially the

operational costs for chemicals including potassium hydroxide or other solid electrolytes. The US department of energy[7] established a goal to reduce the total hydrogen production cost by virtually 50% in within the next 10 years. Therefore, a different strategy to finding an alternative electrolyte is required to reduce the electricity and chemical reagents consumption for molecular hydrogen production.

1.2. TECHNOLOGYCAL BACKGROUND

1.2.1. Wastewater Electrolysis Cell. A well-designed wastewater electrolysis cell (WEC, Figure 1.1) can provide a feasible approach for self-sustainable on-site wastewater treatment with simultaneous decentralized H_2 production. Chloride ion is a ubiquitous, naturally occurring anion providing electric conductivity and, when employing saline wastewater as a background electrolyte for electrochemical water splitting, the chloride ion is oxidized to reactive chlorine species (RCS, $Cl\cdot$, Cl_2, and conjugate species) to remove environmental pollutants including organics, ammonium ion, and coliform bacteria.[8] This green chemistry that acts without external chemicals can be totally driven by photovoltaic (PV) panels,[9] which makes the PV-powered WEC (PWEC) a traditional infrastructure-free approach.[10] Simultaneously with the wastewater treatment, solar energy storage is possible by cathodic production of H_2, which can be utilized as a secondary energy source for the PWEC or for other domestic living purposes.[11] By this dual-functioning approach, one can reduce the cost of electrolytic H_2 production, particularly the cost for electrolyte and electricity, by saving energy for water treatment. Recent statistics suggest that handling water and wastewater occupied up to 4% of total electricity consumption in

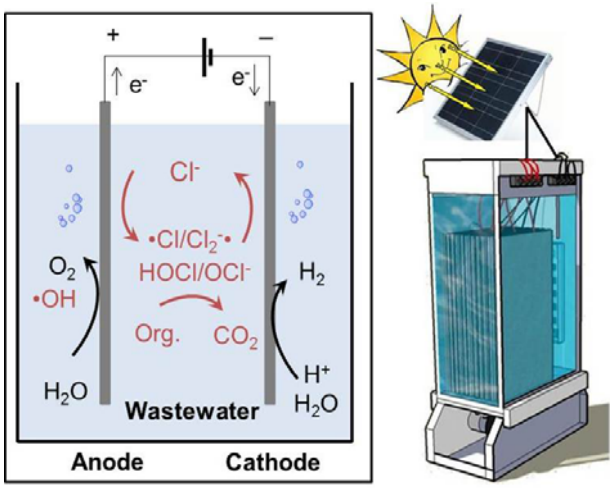

Figure 1.1. Schematic diagram of photovoltaic-powered wastewater electrolysis cell for on-site waste treatment for reuse with simultaneous solar energy storage by hydrogen production.

the US and the collection and treatment of wastewater consume up to 5 Wh of electricity per gallon of wastewater in California.[12]

1.2.2. Electrochemical Degradation of Environmental Pollutants. The electrochemical system has often been used for treatment of high-salinity wastewater such as dye (textile) wastewater, landfill leachate, olive mill wastewater, tannery wastewater, livestock industry wastewater, and reverse osmosis concentrates, among many other usages. In addition, degradations (mostly oxidative) of non-biodegradable or recalcitrant environmental pollutants (pesticides, pharmaceuticals and personal care products, polycyclic aromatic hydrocarbons, and other aliphatic/phenolic compounds) have been widely investigated in electrochemical cells, usually employing laboratory-generated electrolyte (substrates of interest in background electrolyte). More thorough reviews on the electrochemical wastewater treatment can be found in recent reports by Panizza and Cerisola,[13] Martinez-Huitle and Ferro,[14] and Chaplin.[15]

Electrochemical wastewater treatment systems with a wide array of electrodes have conventionally categorized the electro-catalytic anodes into the following two groups: active electrodes and non-active anodes. Since the non-active anodes actually do catalyze heterogeneous oxidation of environmental pollutants, these terminologies should be interpreted in terms of electro-catalytic activity for oxygen evolution reaction (OER). In other words, the most common non-active anodes include SnO_2, PbO_2, and boron-doped diamond (BDD), which show relatively high over-potential for OER. In contrast, mixed metal oxides electrodes based on IrO_2 or RuO_2 have the lowest OER over-potential and are referred to as active anodes in the field of electrochemical wastewater treatment.

Based on the mechanistic point of view, on the other hand, electrochemical pollutants oxidation is referred to either as direct oxidation or indirect oxidation. Despite some discrepancy among researchers, direct oxidation generally corresponds to heterogeneous oxidation of target pollutants on the anode surface, while indirect oxidation accounts for homogeneous oxidation of pollutants often mediated by reactive oxygen species (ROS) and the RCS. In spite of a possibility of direct electron transfer from the target pollutants to the anode, the heterogeneous direct oxidation has been almost exclusively ascribed to the surface bound ROS, particularly hydroxyl radical (·OH). When the anode surface under a potential bias is able to liberate free ROS, as reaction intermediates or byproducts of OER, the indirect oxidation can take place via mediation of homogeneous ·OH, H_2O_2, and O_3. However, it is difficult to distinguish the direct oxidation by surface-bound ROS from the indirect oxidation by free ROS, due to the short life and low yield of free ROS. Therefore, the RCS generated in the presence of a chloride ion (usually in 10 mM to 100 mM range) in the electrolyte has been appreciated as the primary mediator of indirect oxidation.

1.2.3. Molecular H_2 Production from (PV-Powered) Electrolysis of Wastewater. A wastewater electrolysis cell may prove to be a promising approach for decentralized H_2 production with simultaneous on-site wastewater treatment. Hoffmann and co-workers[8,9,16-18] have investigated the electrolytic H_2 production from model organics containing solutions or real wastewater (domestic or industrial wastewater) in circum-neutral pH. In these reports, inexpensive stainless steel was employed as a cathode. The cathodic current efficiency and energy efficiency of H_2 production have been reported to vary widely depending on the electrolyte composition (NaCl or Na_2SO_4 background, electrical conductivity, concentration of electron donating substrates other than water), cell configuration (distance between anode and cathode, geometric area), and operating condition (applied cell voltage). The reported values ranged from 40 to 80% for current efficiency and from 15 to 60% for energy efficiency. The major scavenging reactions for H_2 production include reduction of RCS (to chloride ion) in NaCl background and reduction of oxygen (to superoxide radical and its dissociation products). The current efficiency for H_2 production was usually higher in the $NaSO_4$ background than in the NaCl background. In the NaCl background solution, a presence of electron donating substrates enhances the current and energy efficiency of H_2 production. For example, batch injections of small amounts of organics including urea, phenol, and other oxidizable organics sharply enhanced the production of H_2. The RCS competing with water and proton to accept electrons can be readily quenched by the organics to enhance the H_2 production. The energy efficiency of H_2 production decreased as the electrical conductivity decreased or applied cell voltage (or current) increased, primarily owing to the increase in ohmic energy loss. Park *et al.*[9,17] would be the first to attempt electrolytic H_2 production from dilute

aqueous solutions, which was solely powered by photovoltaic panels. In these reports, the sequential energy losses in the PV panel and the electrolysis cell resulted in net energy conversion efficiency about 1% (2.5% energy efficiency for solar light to direct current and 30~60% energy efficiency for the direct current to H_2).

1.2.4. Mixed Metal Oxides Anodes. Electrochemical water oxidation on metal oxides (MO_x) anodes has long been believed to initiate from a formation of surface bound hydroxyl radical ($MO_x(\cdot OH)$).[19] The oxygen evolution activity is largely coming from the transition of the surface bound hydroxyl radicals to the chemisorbed active oxygen (MO_{x+1}).[19] The $MO_x(\cdot OH)$ is a strong oxidant (standard redox potential of free ·OH is 2.8 V versus Normal Hydrogen Electrode) and, as a rule of thumb, prefers oxidation of pollutants or chloride ion to the OER. Boron doped diamond, SnO_2, and PbO_2 are well known anode materials which can provide both the direct pollutants oxidation and indirect oxidation with a presence of chloride ions. Owing to the high OER overpotential for these non-active anodes, the resulting current efficiency of pollutants oxidation sometimes approached unity, which could be mitigated by mass transport limitation. However, a concomitant large kinetic barrier for the initial water discharge ($MO_x(\cdot OH)$ formation) requires relative large energy consumption and limits their application for H_2 production and energy storage purposes. On the contrary, the higher oxides favor liberation of the lattice active oxygen to molecular O_2 and a direct oxidation of pollutants is relatively sluggish. Therefore, indirect oxidation mediated by RCS plays more important roles for the anode materials undergoing facile redox oxide transition. RuO_2 or IrO_2 based metal oxides anodes have been widely employed as active anodes with relatively low OER overpotentials. Compared to the non-active anodes, the current efficiencies for the

pollutants oxidation are mostly lower on the active anodes, but more pronounced energy efficiency can be achieved owing to the low kinetic barrier to the formations of MO_{x+1}. However, the high material cost for these precious metals is a major barrier for commercialization. A pictorial illustration of the direct and indirect oxidation of pollutants on metal oxide anodes is given in Figure 1.2.

Current discussion can be more elaborated on the volcano plot suggested by Trasatti[20] which describes a relation between the OER overpotential and the enthalpy change in redox transition from lower to higher oxides (Figure 1.3). It has been reported that the enthalpy change in the oxides transition is well correlated with the bond strength between the oxide ion and the central metal ion.[21] The electrodes for direct oxidation would be located in the

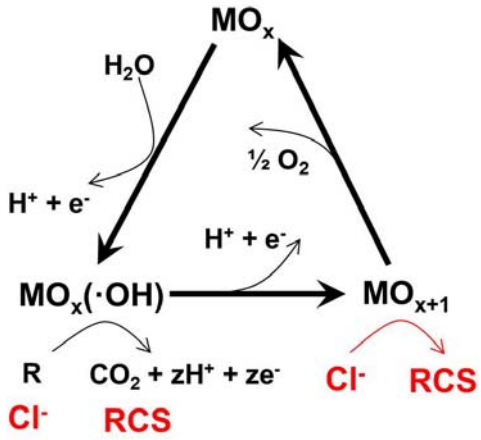

Figure 1.2. A schematic diagram of direct oxidation of organics (R) and indirect oxidation mediated by reactive chlorine species (RCS) on metal oxide (MO_x) electrodes.[19] $MO_x(\cdot OH)$ and MO_{x+1} stand for surface-bound hydroxyl radical and higher oxide, respectively.

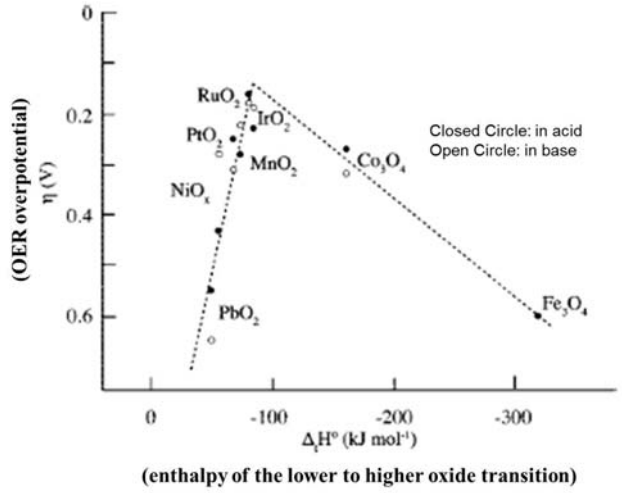

Figure 1.3. Volcano plot of the overpotential of oxygen evolution reaction (OER) for various types of metal oxide electrode as a function of enthalpy change for lower to higher oxide. Reproduced from Trasatti.[20]

left-hand side of the apex (*e.g.*, PbO_2) and the formation of the higher oxides requires large energy input. Therefore, the initial water discharge is rate determining and weakly coordinated hydroxyl radicals are subject to reactions with aqueous solutes (R or Cl^-) with relatively high current efficiencies.[22] The summit of the volcano is occupied by active anode materials (RuO_2 and IrO_2) whose nearly optimal M-O bond strengths allow for facile OER. On the other hand, the metal oxides in the right-hand side of the apex (*e.g.*, Co_3O_4 and Fe_3O_4) undergo the oxide transition too easily and the liberation of active oxygen is the rate determining step.

1.2.5. Hetero-junction Anodes with BiO_x/TiO_2 Functionalities. The core components of the wastewater electrolysis cells investigated in this study include hetero-junction anodes sequentially coated with a series of mixed metal oxides. The electrodes were prepared by sequential thermal decomposition of mixed oxides of Ti and Bi on Ti base plates pretreated

with IrO_2, Ta_2O_5, SnO_2, and Bi_2O_3, as shown in Table 1.1.[23] Based on an electron probe microanalysis, the outer surface of the electrode is dominantly composed of bismuth, titanium, and oxygen, to be designated as BiO_x/TiO_2 electrode.[24] The hetero-junction electrode fabrication is expected to bring about a shift in heterogeneous kinetics. In particular, the surface BiO_x/TiO_2 functionality can provide active sites for hydroxyl radical formation while the underlying precoat layer based on IrO_2 would reduce the kinetic barrier for water discharge. Also, the hetero-junction design should minimize losses of precious IrO_2, while the seal-coat layer based on SnO_2 is believed to enhance the conductivity of the electrode.[23]

Table 1.1. Fabrication procedure of BiO_x/TiO_2 hetero-junction electrodes used in this study (Chapter 2 – 4).[23]

Layer	Nominal Composition	Precursor	Annealing[a]	Repeat
Overcoat (O)	TiO_2/Bi_2O_3 (Ti:Bi = 70:30 mol%)	175 mM Ti-Glycolate Complex + 75 mM bismuth citrate in 225 mM NH_4OH	500 ºC	4
			250 ºC	2
			250 ºC[c]	2
Slurrycoat (Sl)	Bi-doped TiO_2 (Ti:Bi = 96:4 mol%)	300 mM Bi-doped TiO_2 (Bi:Ti = 4:96) in water (pH 11)	250 ºC[b]	7
Sealcoat (S)	SnO_2/Bi_2O_3 (Sn:Bi = 90:10 mol%)	225 M $SnCl_4 \cdot 5H_2O$ + 12.5 mM Bi_2O_3 in 0.5 M HCl	425 ºC	4
Precoat (P)	IrO_2/Ta_2O_5 (Ir:Ta = 67:33 mol%)	73 mM $H_2IrCl_6 \cdot nH_2O$ + 27 mM $TaCl_5$ in 4 M HCl	525 ºC	6

[a] Annealing time is 10 min except for the final annealing (1 h).

[b] Brush of Sl precursor and 4 V% O precursor before annealing.

[c] Brush 50 V& O precursor before annealing.

A series of investigations on the BiO_x/TiO_2 anodes noted reliable indirect oxidation of various types of environmental pollutants (model phenol compounds,[8,9,17,18] urea,[25] arsenite,[26] industrial wastewater,[18] and domestic wastewater[16]) and stability during a long-term electrolysis in circum-neutral pH. Nevertheless, the preparation procedure is actually the outcome of technical trial-and-error, and somewhat complicated, as shown in Figure 1.4. Therefore, it needs further modification to be a simplified preparation method. In addition, the core nature of each layer relevant to the activity and stability is not fully understood.

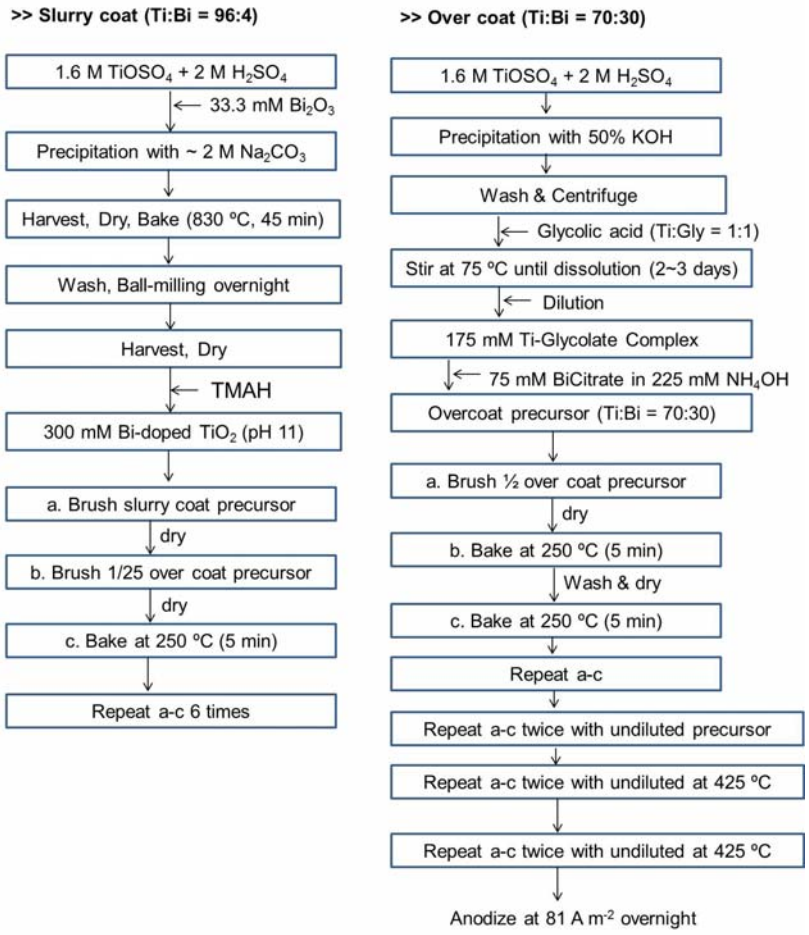

Figure 1.4. Detailed fabrication procedure for slurry coat and overcoat described in Table 1.1.[23]

1.3. OBJECTIVES AND POTENTIAL CONTRIBUTIONS OF THE THESIS

The objectives of this study are to develop a wastewater electrolysis cell which includes hetero-junction anodes as core components for potential application to toilet wastewater treatment, and to provide an underlying scientific background particularly for the redox transformation of environmental pollutants and molecular hydrogen production.

This study can be distinguished from the previous works by using bismuth doped titanium dioxide (BiO_x/TiO_2) anode, which shows reliable electrocatalytic activity and stability in long-term operation. In addition, simultaneous molecular hydrogen production along with waste treatment is another unique feature of this study, and the multi-functional approach of the electrochemical system can be denoted as wastewater electrolysis cell. In the electrochemical wastewater treatment system, the complex reaction networks involve heterogeneous and homogeneous ROS and RCS depending on the operating condition. Therefore, there has been a controversy on the primary oxidants which account for the mineralization of environmental pollutants. While the previous reports generally infer the existence of various reactive oxidants based on the cell voltage, this study employs potentiostatic electrolysis with precise monitoring of anodic potential and ohmic loss. The experimental approach of this study allows more plausible explanations for the role of various oxidants in comparison with their thermodynamic redox potentials. Comprehensive environmental analyses coupled together with kinetic models are expected to provide in-depth knowledge related with various redox reactions mediated by the chloride ion present in human waste.

1.4. THESIS OVERVIEW

This thesis consists of the following six chapters. The overall composition of the thesis is illustrated in Figure 1.5.

- Chapter 1 – Introduction
- Chapter 2 – Urea degradation by electrochemically generated reactive chlorine species: Products and reaction pathways
- Chapter 3 – Effects of anodic potential and chloride ion on overall reactivity in electrochemical reactors designed for solar-powered wastewater treatment
- Chapter 4 – Electrochemical treatment of human waste coupled with molecular hydrogen production
- Chapter 5 – $Bi_xTi_{1-x}O_z$ functionalized hetero-junction anode with an enhanced reactive chlorine generation efficiency in dilute aqueous solutions
- Chapter 6 – Outlook for the future

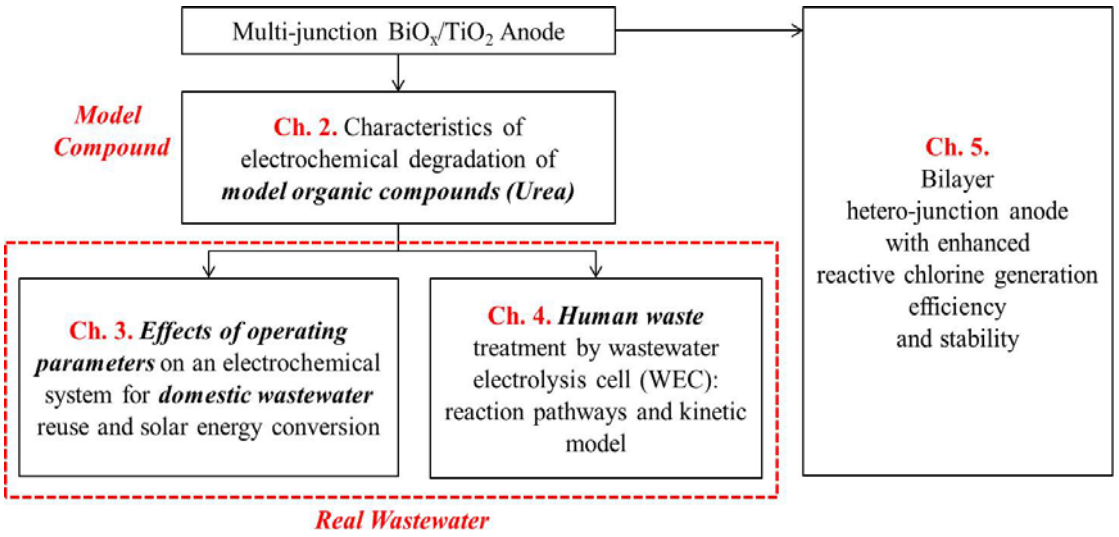

Figure 1.5. Overall composition of this thesis

1.5. REFERENCES

(1) *UN-water global annual assessment of sanitation and drinking-water (GLAAS) 2012 report: the challenge of extending and sustaining services*; World Health Organization: Switzerland, 2012.; http://www.un.org/waterforlifedecade/pdf/glaas_report_2012_eng.pdf.

(2) Grant, S. B.; Saphores, J. D.; Feldman, D. L.; Hamilton, A. J.; Fletcher, T. D.; Cook, P. L. M.; Stewardson, M.; Sanders, B. F.; Levin, L. A.; Ambrose, R. F.; Deletic, A.; Brown, R.; Jiang, S. C.; Rosso, D.; Cooper, W. J.; Marusic, I. Taking the "Waste" out of "Wastewater" for human water security and ecosystem sustainability. *Science* **2012,** *337* (6095), 681-686.

(3) *Onsite wastewater treatment systems manual*; EPA/625/R-00/008; United States Environmental Protection Agency: Washington, D.C., 2002.; nepis.epa.gov/Adobe/PDF/P100FS7K.pdf.

(4) *Guidelines for water reuse*; EPA/600/R-12/618; United States Environmental Protection Agency: Washington, D.C., 2012.; nepis.epa.gov/Adobe/PDF/P100FS7K.pdf.

(5) *Clean Watersheds Needs Survey: Report to Congress*; EPA-832-R-10-002; United States Environmental Protection Agency: Washington, DC., 2008.; water.epa.gov/scitech/datait/databases/cwns/upload/cwns2008rtc.pdf.

(6) *The Fuel Cell Technologies Program Multi-Year Research, Development, and Demonstration Plan*; United States Department of Energy: Washington, D.C., 2012.; http://energy.gov/eere/fuelcells/fuel-cell-technologies-office-multi-year-research-development-and-demonstration-plan.

(7) *2013 Annual Progress Report: DOE Hydrogen and Fuel Cells Program*; DOE/CO-102013-4260; United States Department of Energy: Washington, D.C., 2013.; http://www.hydrogen.energy.gov/annual_progress13.html.

(8) Park, H.; Vecitis, C. D.; Hoffmann, M. R. Electrochemical water splitting coupled with organic compound oxidation: The role of active chlorine species. *J Phys Chem C* **2009,** *113* (18), 7935-7945.

(9) Park, H.; Vecitis, C. D.; Hoffmann, M. R. Solar-powered electrochemical oxidation of organic compounds coupled with the cathodic production of molecular hydrogen. *J Phys Chem A* **2008,** *112* (33), 7616-7626.

(10) Cho, K.; Qu, Y.; Kwon, D.; Zhang, H.; Cid, C. A.; Aryanfar, A.; Hoffmann, M. R. Effects of anodic potential and chloride ion on overall reactivity in electrochemical reactors designed for solar-powered wastewater treatment. *Environ Sci Technol* **2014,** *48* (4), 2377-2384.

(11) Cho, K.; Kwon, D.; Hoffmann, M. R. Electrochemical treatment of human waste coupled with molecular hydrogen production. *Rsc Adv* **2014,** *4* (9), 4596-4608.

(12) *Energy Demands on Water Resources: Report to Congress on the Interdependency of Energy and Water*; United States Department of Energy: Washington D.C., 2006.

(13) Panizza, M.; Cerisola, G. Direct and mediated anodic oxidation of organic pollutants. *Chem Rev* **2009,** *109* (12), 6541-6569.

(14) Martinez-Huitle, C. A.; Ferro, S. Electrochemical oxidation of organic pollutants for the wastewater treatment: direct and indirect processes. *Chem Soc Rev* **2006,** *35* (12), 1324-1340.

(15) Chaplin, B. P. Critical review of electrochemical advanced oxidation processes for water treatment applications. *Environ Sci-Proc Imp* **2014,** *16* (6), 1182-1203.

(16) Park, H.; Choo, K.; Park, H.; Choi, J.; Hoffmann, M. R. Electrochemical oxidation and microfiltration of municipal wastewater with simultaneous hydrogen production: Influence of organic and particulate matter. *Chemical Engineering Journal* **2013,** *215-216* (15), 802-810.

(17) Park, H.; Vecitis, C. D.; Choi, W.; Weres, O.; Hoffmann, M. R. Solar-powered production of molecular hydrogen from water. *J Phys Chem C* **2008,** *112* (4), 885-889.

(18) Choi, J.; Qu, Y.; Hoffmann, M. R. SnO_2, IrO_2, Ta_2O_5, Bi_2O_3, and TiO_2 nanoparticle anodes: electrochemical oxidation coupled with the cathodic reduction of water to yield molecular H_2. *J Nanopart Res* **2012,** *14* (8).

(19) Comninellis, C. Electrocatalysis in the electrochemical conversion/combustion of organic pollutants for waste-water treatment. *Electrochim Acta* **1994,** *39* (11-12), 1857-1862.

(20) Trasatti, S. Electrocatalysis in the anodic evolution of oxygen and chlorine. *Electrochim Acta* **1984,** *29* (11), 1503-1512.

(21) Rossmeisl, J.; Qu, Z. W.; Zhu, H.; Kroes, G. J.; Norskov, J. K. Electrolysis of water on oxide surfaces. *J Electroanal Chem* **2007,** *607* (1-2), 83-89.

(22) Walter, M. G.; Warren, E. L.; McKone, J. R.; Boettcher, S. W.; Mi, Q. X.; Santori, E. A.; Lewis, N. S. Solar water splitting cells. *Chem Rev* **2010,** *110* (11), 6446-6473.

(23) Weres, O. Electrode with surface comprising oxides of titanium and bismuth and water purification process using this electrode. U.S. Patent 7,494,583 B2, Feb. 24, 2009.

(24) Park, H.; Bak, A.; Ahn, Y. Y.; Choi, J.; Hoffmannn, M. R. Photoelectrochemical performance of multi-layered BiO_x-TiO_2/Ti electrodes for degradation of phenol and production of molecular hydrogen in water. *J Hazard Mater* **2012,** *211*, 47-54.

(25) Kim, J.; Choi, W. J. K.; Choi, J.; Hoffmann, M. R.; Park, H. Electrolysis of urea and urine for solar hydrogen. *Catal Today* **2013,** *199*, 2-7.

(26) Kim, J.; Kwon, D.; Kim, K.; Hoffmann, M. R. Electrochemical production of hydrogen coupled with the oxidation of arsenite. *Environ Sci Technol* **2014,** *48* (3), 2059-2066.

Chapter 2

UREA DEGRADATION BY ELECTROCHEMICALLY GENERATED REACTIVE CHLORINE SPECIES: PRODUCTS AND REACTION PATHWAYS

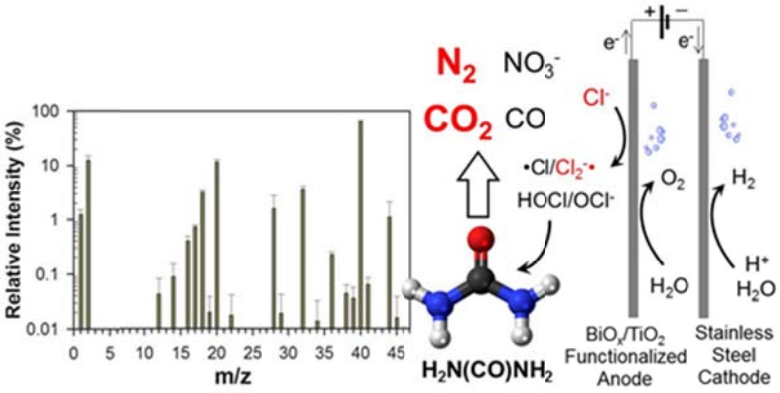

ABSTRACT

This study investigated the transformation of urea by electrochemically-generated reactive chlorine species (RCS). Solutions of urea with chloride ions were electrolyzed using a bismuth doped TiO_2 (BiO_x/TiO_2) anode coupled with a stainless steel cathode at applied anodic potentials (E_a) of either +2.2 V or +3.0 V versus the normal hydrogen electrode. In NaCl solutions, the current efficiency of RCS generation was near 30% at both potentials. In divided cell experiments, the pseudo-first-order rate of total nitrogen decay was an order of magnitude higher at E_a of +3.0 V than at +2.2 V due to the generation of dichlorine radical ($Cl_2^{-}\cdot$) ions. Quadrupole mass spectrometer analysis of the reactor head-space revealed that N_2 and CO_2 are the primary gaseous products of the oxidation of urea, whose urea-N was completely transformed into N_2 (91%) and NO_3^- (9%). The higher reaction selectivity with respect to N_2 production can be ascribed to a low operational ratio of RCS to N. The mass-balance analysis recovered urea-C as CO_2 at 77%, while CO generation most likely accounts for the residual carbon. In light of these results, we propose a reaction mechanism involving chloramines and chloramides as reaction intermediates, where the initial chlorination is the rate-determining step in the overall sequence of reactions.

2.1. INTRODUCTION

Urea is the most abundant nitrogen (N) carrier in human excreta,[1-3] and therefore is the dominant source of N in domestic wastewater. In spite of the relatively low toxicity of urea, there is a growing concern that excessive N loading from toilet wastewater is leading to the eutrophication of surface waters. Major cities located in sensitive coastal areas are experiencing algal blooms in estuary waters that appear to be correlated to nutrient loading from household septic systems.[4] During transport through sanitary sewer systems, urea-N is readily converted to NH_4^+-N via enzymatic hydrolysis by urease. In septic systems, the pH can rise to 9 due to the protonation of ammonia released during the enzymatic hydrolysis.[5] Due to the heavy loading of N in human waste, various groups are exploring source separation in order to harvest the urine at a reduced volume before discharge into a large volume disposal system.[2] In this respect, one can envision an on-site method for removing the N loading due to urea and thus avoiding problems resulting from the extended storage of toilet wastewater. Current demands on total maximum daily load reductions may require decentralized wastewater treatment methods, due to limited options for expanding the capacity of centralized wastewater treatment plants. The Bosch-Meiser process used to produce urea also discharges wastewater loaded with residual urea (< 30% of products[1]) and thus requires a direct urea treatment technology other than the methods of adsorption or biological treatment that are currently employed.[6]

When compared to biological nitrogen removal processes (nitrification or Anammox) for urine treatment whose hydraulic retention times range up to a few days,[2] electrochemical treatment can be an efficient way to accomplish urea degradation at

relatively fast reaction rates (retention time within a few hours[6,7]). Operational flexibility and energy sustainability can also be achieved when using a renewable energy source (*e.g.*, photovoltaic-panel[8]). Botte and co-workers[9-11] investigated nickel (II) hydroxide based electro-catalysts to facilitate a direct electron transfer from urea-N to anodes operating in a strong alkaline solution (*e.g.*, 1 to 5 M of KOH). Other electrochemical systems have explored mixed metal oxide anodes based on RuO_2, IrO_2, and PtO_2, to treat urea (< 0.2 M) with near equi-molar amount of chloride ion.[6,7,12,13] In these systems, free reactive chlorine (HOCl or OCl^-) appeared to be the primary oxidant leading to urea degradation, while chloramines were often observed as reaction intermediates.[12]

There appears to be a reasonable consensus that N_2 and CO_2 are the eventual products during chlorination of urea,[7,13] although there are reports of N_2O (nitrous oxide) as a final N-containing product.[14] However, little data can be found on the exact speciation of the potential array of gaseous products. On the other hand, we recently demonstrated that electrochemically generated chlorine radicals can rapidly reduce the chemical oxygen demand in domestic wastewater.[15] In this case, the reactive chlorine species (RCS) is used as a collective term for the sum of free chlorines and chlorine radicals such as the chlorine atom ($Cl\cdot$) and chlorine radical anion ($Cl_2^{-}\cdot$).

With these considerations in mind, we now report on the details of N transformation during urea degradations via RCS generated on hetero-junction anodes functionalized with bismuth-doped titanium dioxide (BiO_x/TiO_2). Parallel analyses of products generated in the aqueous phase and gas phase allowed for mass and charge balance determinations of the nitrogenous and carbonaceous species. The effects of applied

anodic potential (E_a) on the rates of total nitrogen (TN) decay and products formation were also explored in order to assess the detailed roles of chlorine radicals during urea oxidation. The degradation of urea by electrochemically generated RCS seems to resemble the 'chemical (most often using NaOCl)' chlorination mechanisms[14] (the process used to investigate the formation of chlorinated byproducts in swimming pools). However, we note that the differences in operational molar ratios of RCS to N as well as the chlorine radical generation rates change the kinetic parameters and the selectivity towards the final products in the electrolytic urea degradation.

2.2. EXPERIMENTAL SECTION

2.2.1. Preparation of BiO_x/TiO_2 Anode and Electrolysis Cell. In a typical preparation,[15,16] Ti metal sheets (0.5 mm thick, pretreated by sand-blasting, degreasing, and etching) were doubly coated sequentially with mixed metal oxide layers by repetitive thermal decomposition of Ir/Ta solution (73 mM H_2IrCl_6 and 27 mM $TaCl_5$ in 4 M HCl; anneal at 525 °C), Sn/Bi solution (225 mM $SnCl_4$ and 12.5 mM Bi_2O_3 in 0.5 M HCl; at 425 °C), Ti/Bi slurry (*ca.* 300 mM Bi-doped TiO_2; at 250 °C), and Ti/Bi solution (225 mM Ti-Glycolate complex and 25 mM bismuth citrate in 75 mM NH_4OH; at 425°C).

Single compartment electrolysis cells (working volume of 60 mL) were prepared using a BiO_x/TiO_2 anode and stainless steel cathode pair (3 × 2 cm^2, 5 mm gap) with a Ag/AgCl/Sat. KCl reference electrode (BaSi Inc., USA) whose Vycor® glass tip was 2 mm apart from the anode center. For divided cell configuration, a Pt wire encapsulated in a tube with Vycor® glass frit separator was used as a cathode. A schematic diagram of

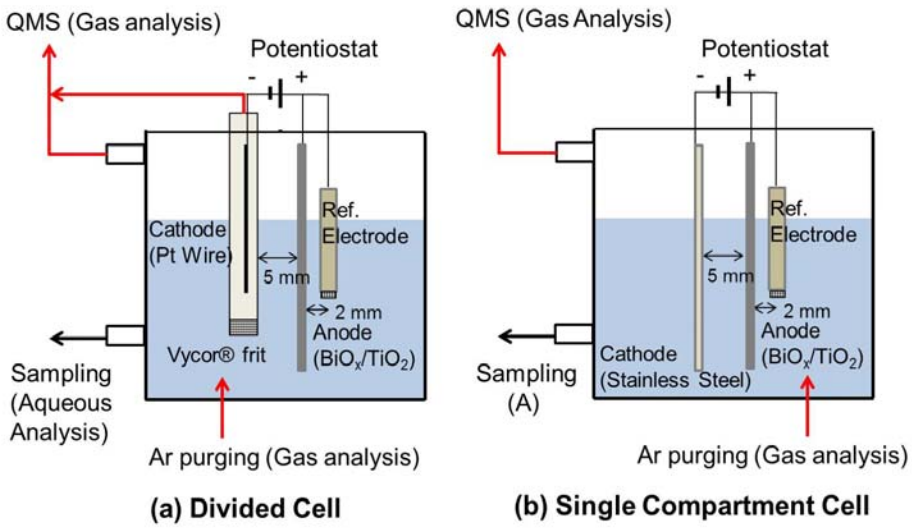

Figure 2.1. Schematic diagram of electrolysis cells (working volume: 60 mL) used in this study.

each electrolysis cell is shown in Figure 2.1. The frit separator reduces interferences of cathodic reactions to estimate more reliable kinetic parameters, while an increased electrical resistance of the divided cell decreases the response current density (J) at a given E_a. All electrochemical experiments were performed under potentiostatic conditions driven by a SP-50 potentiostat (Bio-Logics, USA).

2.2.2. Potentiostatic Electrolysis of NaCl Solutions with or without Urea. The rate and current efficiency of RCS generation were estimated in the single compartment cell with 50 mM NaCl solutions. The RCS evolution rates were measured in terms of total chlorine (Cl_{DPD}) concentrations at a fixed time interval (2 min) three times. The relatively short reaction duration (6 min) was intended to minimize the oxidation or reduction of RCS, which would cause a non-linear increase of [RCS] with time.[16,17] These experiments were repeated with E_a varying from 1.5 to 3.0 V versus the normal hydrogen electrode (NHE).

The current efficiency for the RCS generation (η_{RCS}) was estimated by the following equation:

$$\eta_{\mathrm{RCS}} = \frac{2\,VF\,d[Cl_{DPD}]}{I\,dt} \tag{2.1}$$

where, V is electrolyte volume (0.06 L), F is Faraday constant (96485.3 C mol^{-1}), [Cl_{DPD}] is the concentration of RCS (M), I is current (A), and t is electrolysis time (sec).

The electrochemical urea degradation experiments were performed in a divided cell (E_a: 2.2 V or 3.0 V NHE, 3 h) or in a single compartment cell (E_a: 3.0 V NHE, 6 h). The reaction solution contained 41.6 mM (2.5 g L^{-1}) of urea in the presence of 50 mM NaCl (electrical conductivity: 5.6 ± 0.1 mS cm^{-1}). The initial [urea] was in accordance with a recipe for synthetic urine[18] assuming 10-fold dilution by flushing. The molar ratio of urea-N to Cl^- (close to 1.7) was compatible with operational ranges in analogous literature,[6,12] while it was less than half of the observed ratios for fresh urine.[2] We rationalize the low urea-N/Cl^- ratio by the scenario either of moderate storage before treatment (decreasing [urea]) or reuse of treated effluent as flushing water (increasing [Cl^-]). Urea solutions with 50 mM Na_2HPO_4 (7.4 ± 0.1 mS cm^{-1}) were also tested in the divided cell as control experiments, to evaluate urea oxidation by a direct electron transfer from urea to the semiconductor anode. Small aliquots of electrolyte were sampled periodically to monitor the speciation of aqueous-phase N. Gaseous products in the reactor headspace were analyzed by HPR-20 gas analysis system (Hiden Analytical, USA) with a heated quartz inert capillary inlet under continuous purging of Ar gas (*ca.* 7 mL min^{-1}).

2.2.3. Analytical Methods. The pH, conductivity and electrical resistance of solutions before and after the electrolysis were determined using a pH meter (Mettler Toledo, USA), a conductivity meter (VWR International, USA), and the current interruption function of the potentiostat with a current bias of 200 mA, respectively. The [urea] was determined using a hydrolysis method employing Jack Bean Urease as described previously.[16] However, the measured values of [urea] were reliable only for the control experiments due to interferences of RCS with urease activity.[20] The principal ions of interest (Cl^-, ClO_3^-, NO_2^-, NO_3^-, NH_4^+) were quantified by DX-500 ion chromatography system (Dionex, USA), equipped with the anion-exchange column Ionpac AS 19 and the cation-exchange column Ionpac CS 16. [TN] were determined using low range (0.5 to 25 mg N L^{-1}) TN reagent kits (Hach, USA) according to absorbance at 420 nm in the UV-VIS spectrophotometer (Agilent, USA) after digestion. The [Cl_{DPD}] was measured with DPD (N,N-diethyl-p-phenylenediamine)/KI reagents (Hach, USA) based on the absorbance at 530 nm. It has been reported that, in urea chlorination, the Cl_{DPD} accounts for chlorinated urea species as well as inorganic chloramines.[21] Analogous measurements with DPD reagents (Hach, USA) were performed to quantify the fraction of free chlorine in the Cl_{DPD}. The gaseous products underwent 70 eV electron impact ionization, and fragments (m/z 1 to 300) were analyzed using a quadrupole mass spectrometer (QMS) in a vacuum (< 5.0×10^{-6} Torr) generated by a turbo pump. The volume percent in the headspace gas was assumed to be directly proportional to the ion current measured by the QMS. Quantification of the gases of interest was based on the relative ion current intensities of characteristic m/z (14 for N_2, 44 for CO_2) and the volumetric flow rate of total gaseous products measured with a mass flow-meter (Bronkhorst, USA). The limit of

detection, defined as three times the standard deviation of the relative ion intensities under injection of blank gas (Ar), was estimated to be *ca.* 100 ppm for m/z 1 to 46 (except fragments from Ar) and 1 ppm for m/z 47 to 300. Additional details are given in Supporting Information.

2.3. RESULTS AND DISCUSSION

2.3.1. RCS Generation on BiO_x/TiO_2 Anode. Figure 2.2 shows the RCS generation profiles obtained with the BiO_x/TiO_2 anode in 50 mM NaCl solutions with circum-neutral pH. The Cl_{DPD} in absence of N compounds accounts for RCS, although it should exist predominantly as free chlorine due to the short life of the chlorine radicals. Cl^- oxidation in terms of the specific RCS generation rate monotonically increased along with J as the E_a increased from 1.5 to 3.0 V NHE (corresponding to cell voltages ranging from 2.5 to 6.0 V). The dependency of J on E_a was nominally linear in dilute chloride solutions due to resistances between anode and the reference electrode; *i.e.*, iR-drop attenuates the exponential response of J described by the Butler-Volmer formulation.[15] The η_{RCS} was below 10% at E_a of 1.5 V NHE (slightly higher than the redox potential of the Cl_2/Cl^- couple), and increased to 24 – 30% at higher potentials. The losses in current efficiency (> 70%) can be dominantly ascribed to the oxygen evolution reaction. In the case of the mixed metal oxide (BiO_x/TiO_2) anode, the surface titanol (*i.e.*, >TiOH) groups provide the active sites for surface hydroxyl radical formation, while the redox transitions of BiO_x (III/V) or underlying IrO_x (IV/VI) serve as electron sinks.[15]

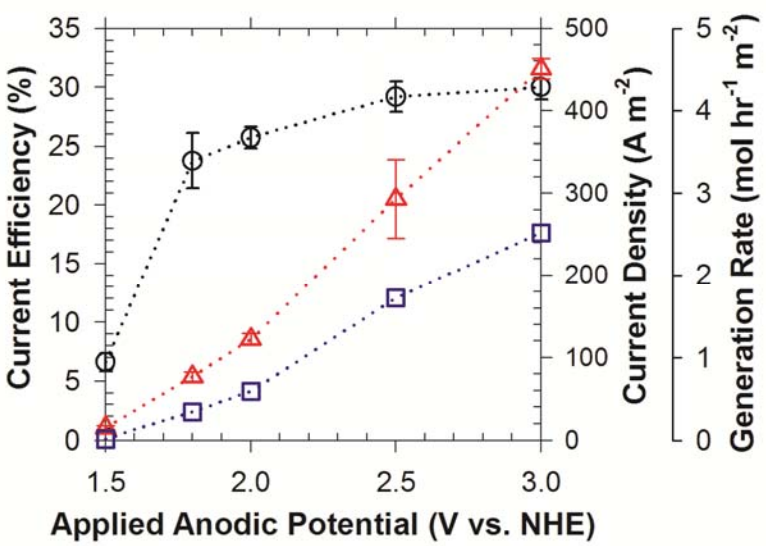

Figure 2.2. Current efficiency (circle) and rate (square) of reactive chlorine generation together with current density (triangle) on average as functions of applied anodic potential during potentiostatic electrolysis of 50 mM NaCl solutions in single compartment cell; anode: BiO_x/TiO_2 (6 cm^2), cathode: stainless steel (6 cm^2). Error bars represent the standard deviations for three samples collected with 2 min intervals.

In this study, the current efficiencies were quasi-constant at potentials higher than 1.8 V NHE. These observations have the following implications; i) the power efficiency for RCS generation should decrease along with E_a, and ii) one can expect a linear dependence of the RCS generation rate on J under the experimental conditions of this study.

2.3.2. Aqueous and Gaseous Products Formed During Urea Degradation. Figure 2.3 shows the transformation of nitrogen during electrolysis of urea solutions with Cl^- in the divided cell. Urea degradation was negligible in a phosphate electrolyte or under E_a of

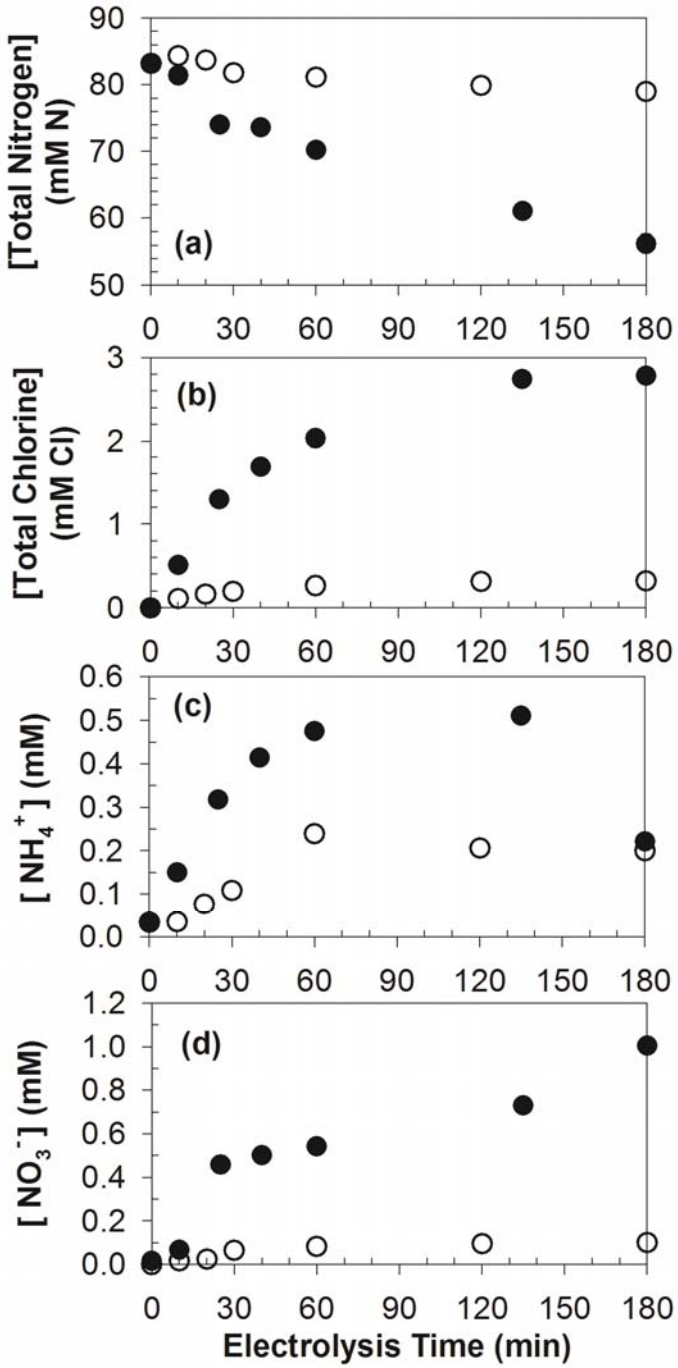

Figure 2.3. Time profiles of (a) total nitrogen, (b) total chlorine (Cl_{DPD}), (c) NH_4^+, and (d) NO_3^- concentration during potentiostatic electrolysis of 41.6 mM urea solutions with 50 mM Cl^- (60 mL) in divided cell; anode: BiO_x/TiO_2 (6 cm^2), cathode: Pt wire in frit separator, applied anodic potential: 2.2 V NHE (empty circle), 3.0 V NHE (filled circle).

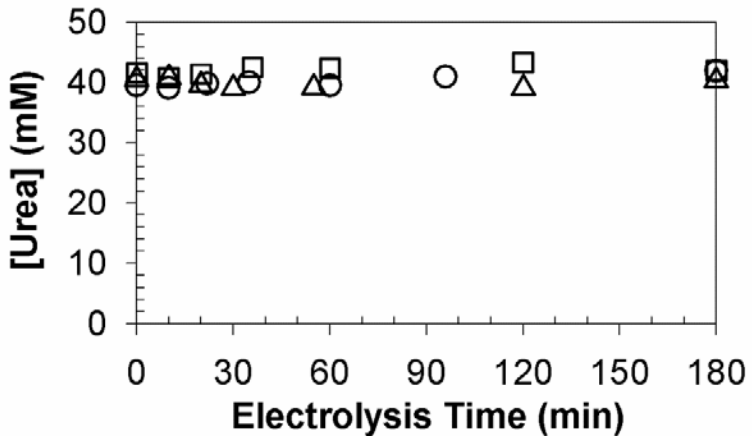

Figure 2.4. Time profiles of urea concentration during control electrolysis of 41.6 mM urea solutions in a divided cell; E_a: (circle) 2.2 V NHE with 50 mM Na_2HPO_4, (triangle) 3.0 V NHE with 50 mM Na_2HPO_4, (square) 1.3 V NHE with 50 mM NaCl, anode: BiO_x/TiO_2 (6 cm^2), cathode: Pt wire in frit separator.

1.3 V NHE in a chloride background (Figure 2.4). These results indicate that a direct electron transfer from urea-N to surface sites on the anode is negligible. The [Cl_{DPD}] was consistently below the detection limit in these control experiments so that a potential interference of reactive oxygen species could be ruled out in subsequent electrolysis experiments. We recently reported[15,16] that, on the BiO_x/TiO_2 anode, the surface bound hydroxyl radicals are readily quenched by redox transitions of Bi(III/IV) to form higher oxides which prefer oxygen evolution to reactive oxygen species generation.[16]

The aqueous products from the electrolytic degradation of urea included NH_4^+, NO_3^-, chloramines (*i.e.*, NH_2Cl, $NHCl_2$, NCl_3), and chlorinated urea. Concentrations of free chlorine were below the detection limit, indicating that the chloramines and chloramides primarily account for the measured Cl_{DPD}. The time profiles of the aqueous products were compatible with the previous reports on chemical urea oxidation by NaOCl.[14] These

suggested that urea is sequentially chlorinated to tetrachlorourea which is oxidized further to produce CO_2 and inorganic chloramines.[3,14] The reversible hydrolysis of chloramines will yield NH_4^+ depending on the pH and the [RCS].[22,23] In addition, the inorganic chloramines are believed to undergo base catalyzed disproportionation to produce gaseous N as in breakpoint chlorination[24], while $NHCl_2$ is further oxidized to NO_3^-.[22] The overall chemical reaction is known to be limited by the first chlorination step of urea, whereas subsequent reactions proceed at much faster rates.[3,14]

At circum-neutral pH, the nominal second-order rate constant for the reaction of urea with free chlorine was determined to be 0.63 M^{-1} s^{-1}.[25] In contrast, the bimolecular reaction between $NHCl_2$ and NCl_3 has a rate constant of 5.6×10^3 M^{-1} s^{-1},[22] while the reaction between NH_2Cl and NCl_3 has a bimolecular rate constant of 1.4×10^2 M^{-1} s^{-1}. In this study, the rate-limiting step in the reaction sequence was found to be the initial reaction between urea and RCS as well. The evolution of gaseous nitrogen appeared to correspond directly to the 'urea + RCS ⟶ reaction intermediates', since the rate of urea degradation was correlated with the rate of TN decay. The sums of Cl_{DPD}, NH_4^+, and NO_3^- concentrations were much smaller than the reduced TN concentrations, which in turn should account for the production of gaseous N species.

Figure 2.5 shows the relative intensities of the ion fragments for the gas products in the single compartment cell experiments. Based on the NIST/EPA/NIH Mass Spectral Library (NIST11), the major peaks in the mass spectrum (m/z 1 to 46) consisted of H_2 (m/z 1 and 2), O_2 (m/z 34, 32 and 16), H_2O (m/z 16 to 19), CO_2 (m/z 44 to 46, 28, 22, 16,

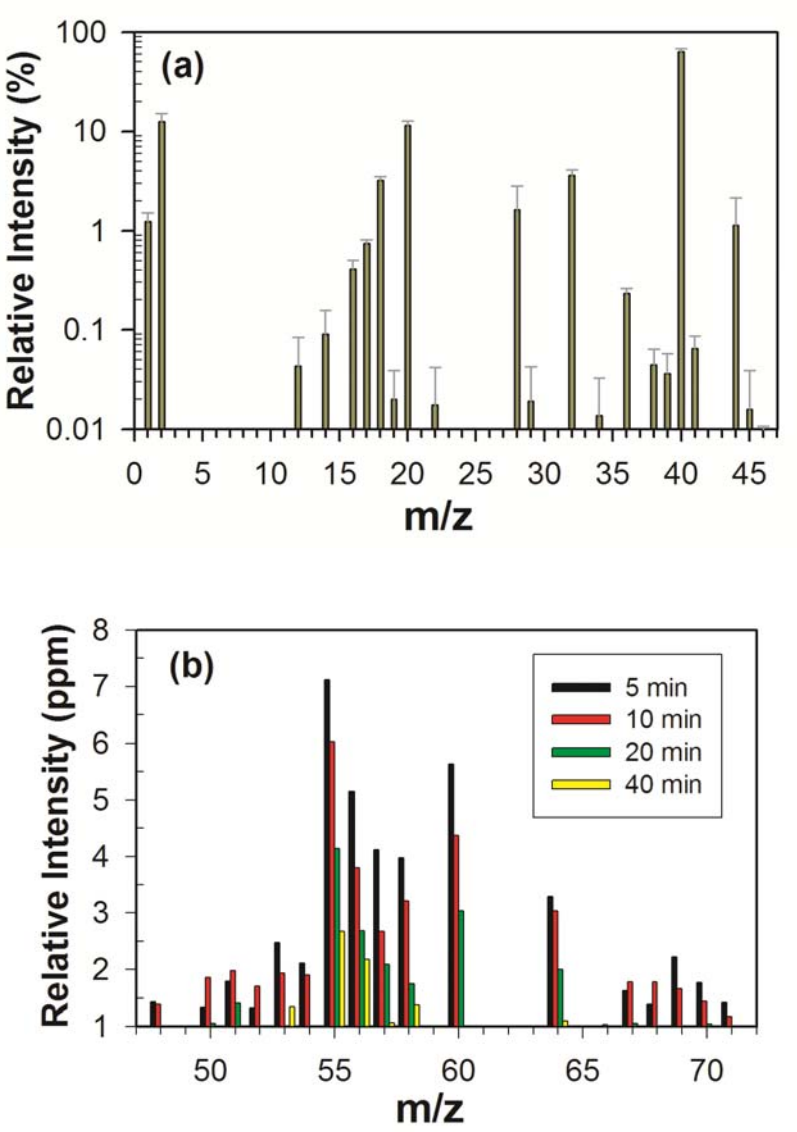

Figure 2.5. Relative intensities of ion fragments in quadrupole mass spectrometer analysis of gaseous products during potentiostatic electrolysis of 41.6 mM urea solutions with 50 mM Cl^- (60 mL) in single compartment cell; anode: BiO_x/TiO_2 (6 cm^2), cathode: stainless steel (6 cm^2), applied anodic potential: 3.0 V NHE. Error bars represent the standard deviations of periodic measurement (detection interval: 1 min).

and 12), N_2 (m/z 29, 28 and 14), and Ar (m/z 40, 38, 36 and 20). From the mass spectral analysis, N_2 appears to be the principal gaseous N product in urea degradation. A negligible signal at m/z 30 (*i.e.*, N_2O) indicates that nitrous oxide is a trace-level product. On the other hand, the ratios of mean signal intensities from H_2 to those from O_2 were much higher than the stoichiometric ratio in water splitting (2:1). This implies that non-stoichiometric water splitting was taking place. Heterogeneous Cl^- oxidation appears to be the main scavenging reaction of oxygen generation at the electrode surface.[26] This process in turn increases the bulk solution pH during electrolysis. Considering that the intensity of m/z 15 was below the detection limit, a stripping of dissolved NH_3 is not apparent due to the low [NH_4^+] in solution (*vide infra*).

2.3.3. Urea Degradation Kinetics in a Divided Cell. As an extension of our recent work,[15] we argue that the electrochemical transformation of urea is accelerated by generation of chlorine radical species. The mean current density at applied potential, E_a, at 3.0 V NHE (83 A m^{-2}) was 3.6 times higher than at 2.2 V NHE (23 A m^{-2}). If the heterogeneous RCS generation is rate limiting, then the formation rates of NO_3^- or N_2 should be proportional to J, given the comparable values of η_{RCS} as shown in Figure 2.2. However, the apparent pseudo first-order decay rate of TN (k_{TN}) in Figure 2.3a was estimated to be 4.4×10^{-6} s^{-1} and 4.0×10^{-5} s^{-1}. The increase of k_{TN} with E_a (9 times) exceeds the proportionality as predicted by the values of J (3.6 times). In addition, the initial rates of Cl_{DPD} evolution in Figure 2.3b increased by more than an order of magnitude under the higher potential bias (5.5×10^{-8} M s^{-1} and 7.8×10^{-7} M s^{-1}, respectively, by linear regression to the initial three data points).

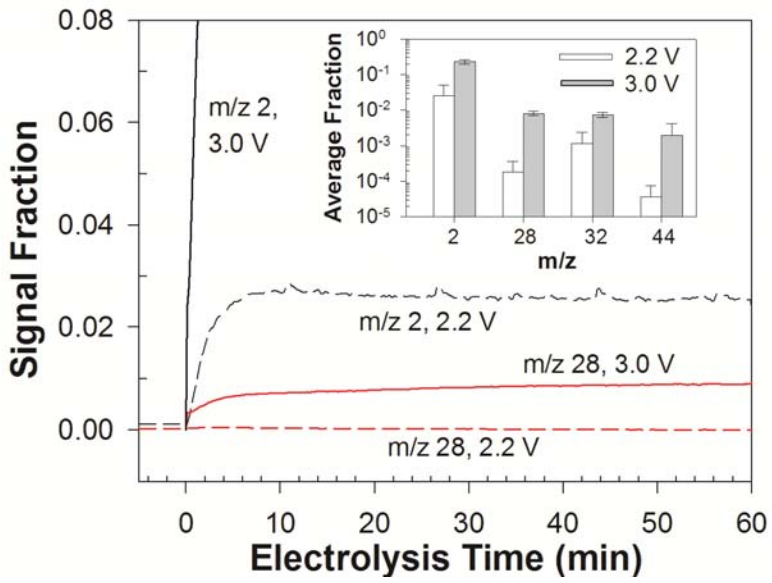

Figure 2.6. Time profiles of relative intensities for ion fragments m/z 2 and 28 in quadrupole mass spectrometer analysis during potentiostatic electrolysis of 41.6 mM urea solutions with 50 mM Cl^- (60 mL) in divided cell; E_a: 2.2 V NHE (dashed line), 3.0 V NHE (solid line), anode: BiO_x/TiO_2 (6 cm^2), cathode: Pt wire in frit separator. Inset figure shows the relative intensities on average for ion fragments m/z 2, 28, 32, 44 for the initial 1 h.

The measurement of gaseous products in a divided cell (Figure 2.6) further supports the enhanced N_2 generation with increasing applied potential. When the E_a was set at 3.0 V NHE, mass fragments appeared immediately at m/z 2 (H_2), 32 (O_2), and m/z 28 (N_2 and CO_2). When the potential was set at 2.2 V NHE, in contrast, the generation of N_2 and CO_2 were minimized, while the oxygen/hydrogen signals were found to be in good agreement with the current density. These combined observations demonstrate that the urea degradation is limited by the homogeneous reaction between urea and RCS.

The chemical reaction network for the electrochemical oxidation of urea mediated by RCS can be summarized in terms of three kinetically significant steps. They are i)

heterogeneous RCS generation, ii) the initial reactions of RCS with urea, and iii) subsequent oxidation reactions involving the initial reaction intermediate (expressed as Cl_{DPD}) to produce N_2. Given this simplification, the governing equations can be written as eq 2.2 and 2.3:

$$-\frac{d[\mathrm{TN}]}{dt} = 2\left(\sum_i k_{1i}[\mathrm{RCS_i}]\right)[\mathrm{Urea}] = k_{TN}[\mathrm{TN}],\ k_{TN} = \sum_i k_{1i}[\mathrm{RCS_i}] \tag{2.2}$$

$$\frac{d[\mathrm{Cl_{DPD}}]}{dt} = k_{TN}[\mathrm{Urea}] - k_2^*[\mathrm{Cl_{DPD}}],\ k_2^* = \sum_i k_{2i}[\mathrm{RCS_i}] \tag{2.3}$$

where k_{1i} and k_{2i} represent the second order rate constants for the reaction of reactive chlorine species *i* (RCS_i) with urea and reaction intermediates (Cl_{DPD}), respectively. The presence of the most abundant reaction intermediates should justify the usage of Cl_{DPD} as an effective summation term. The pseudo-steady-state concentrations of RCS_i allow for the introduction of collective constants, k_{TN} and k_2^*. Eq 2.3 corresponds to the situation in which the initial oxidation of urea is the slow rate-determining step compared with the following steps. In this case, monochlorourea was presumed to be the primary Cl_{DPD}, since sequential chlorination would provide more acidic amido-N moieties which undergo more facile hydrogen abstraction.[14] Use of the divided cell reactor should minimize other RCS-quenching reactions, such as cathodic RCS reduction and anodic chlorate formation. For example, the final chlorate concentrations in the divided cell experiments were less than 1% of the initial chloride concentration, primarily owing to the relatively low current density (*vide infra*). The above set of simplified equations describes the [TN] versus time in terms of a simple pseudo first-order decay profile

(when 2[Urea] ~ [TN]). Non-linear regressions to the observed [Cl_{DPD}] predicted k_2^* of 5 × 10^{-4} sec^{-1} at 2.2 V NHE and 7 × 10^{-4} sec^{-1} at 3.0 V NHE.

The bulk solution pH increased up to 9.5 after the divided cell experiments, due to the non-stoichiometric water splitting. The pK_a of HOCl (7.5) and the solution pH suggest that OCl^- would be the dominant oxidant at the E_a of 2.2 V NHE. However, an acidic environment in anode vicinity would allow for contributions of Cl_2, which was reported to have higher reactivity to urea than HOCl and OCl^-.[14] Although our simplified kinetic approach could not provide rate constants of individual RCS, the collective kinetic parameters (k_{TN}, k_2*) qualitatively indicate a shift in RCS speciation. The iR-compensated anodic potential at E_a of 3.0 V NHE (Table 2.1) was greater than the equilibrium potential needed to liberate 'free' chlorine radical species ($Cl\cdot/Cl_2^-\cdot$).[15,26] In this case, the urea degradation would be initiated by hydrogen abstraction or electrophilic addition of chlorine atom by radicals, whose bimolecular rate coefficients are expected to be much higher than those by free chlorine. Considering the [$Cl_2^-\cdot$]/[$Cl\cdot$] ratio with [Cl^-]

Table 2.1. The ohmic drop compensated anodic potential ($E_a - iR$) and current density (J) on average during the electrolysis of 41.6 mM urea solutions with 50 mM chloride (60 mM) under variable cell types and applied potentials (E_a).

Cell Type	E_a (V, NHE)	$E_a - iR$ (V, NHE)	J (A m^{-2})
Divided	2.2	1.73 (3.1)	23.8 (20)
	3.0	2.24 (4.7)	83.3 (14)
Single Compartment	3.0	2.05 (3.5)	458 (7.5)

of 50 mM (7×10^3 using K_{eq} of 1.4×10^3 M^{-1}), the dichlorine radical anion is expected to be the major radical species under our operating conditions.[26] The reactivity between urea and $Cl_2^{-}\cdot$ has not been reported in literature. As a reference, apparent rate constants of free chlorine reacting with primary amines are in the order of 10^4 M^{-1} s^{-1},[25] while the reactivity of dichlorine radical has been reported up to 10^7 M^{-1} s^{-1}.[27] Nevertheless, the increases of k_{TN} and k_2^* with E_a were within similar orders of magnitude, indicating that the roles of free chlorine should not be ignored even under the radical generation. The $Cl_2^{-}\cdot$ radicals in the aqueous phase are expected to be rapidly disproportionated to free chlorine with diffusion-limited second-order rate constants (> 10^9 M^{-1} s^{-1}).[26]

2.3.4. Urea Transformation Characteristics in Single Compartment Cell. Additional experiments were performed in a single compartment cell with a paired electrode module (E_a: 3.0 V NHE) to investigate the transformation efficiency in a practical setup. As shown in Figure 2.7, the [Cl_{DPD}] followed a typical profile of the breakpoint chlorination; *i.e.*, an initial rise with chloramines/chloramides production, subsequent decrease by chloramine disproportionation to N_2 until the breakpoint is achieved after 4 h, followed by subsequent further increase of free chlorines. Free chlorine concentration was inappreciable until 4 h of electrolysis, while almost superimposable to [Cl_{DPD}] for the last sample (after 6 h). [NH_4^+] showed a peak (0.7 mM) at 3 h of electrolysis and decayed to be negligible along with the dismutation of chloramines. Consequently, the initial urea-N was almost completely transformed into nitrate and N_2 after 6 h, where the residual [TN] (~ 8 mM) roughly coincided with the [NO_3^-]. Figure 2.7c shows molar flow rate of N_2 and CO_2 quantified by volumetric gas flow rate and the observed QMS output signals of

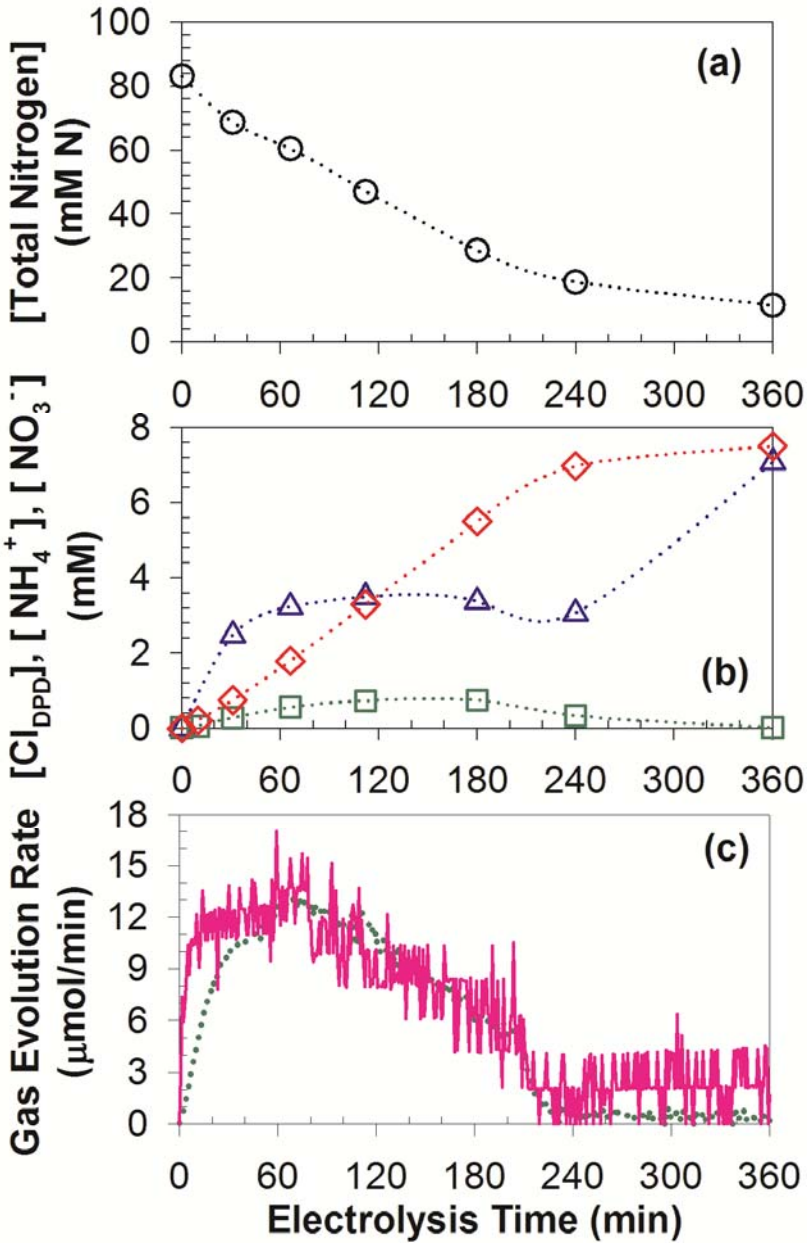

Figure 2.7. Time profiles of total nitrogen (circle), total chlorine (triangle), ammonium (square), and nitrate (diamond) concentration together with molar flow rate of N_2 (solid line) and CO_2 (dotted line) during potentiostatic electrolysis of 41.6 mM urea with 50 mM Cl^- (60 mL) in single compartment cell; anode: BiO_x/TiO_2 (6 cm^2), cathode: stainless steel (6 cm^2), applied anodic potential: 3.0 V.

characteristic m/z ratios. The generation rates of these major gas products followed exponential relationships as predicted by the pseudo first-order kinetic analysis. A mass balance analysis for N indicated that 5 mmol of urea N is transformed into 4.56 mmol N as N_2 (91%) and 0.45 mmol N as NO_3^- (9%). The total amount of CO_2 in the gas products was quantified to be 1.92 mmol, somewhat smaller than the carbon input (2.50 mmol). Furthermore, the signal response at m/z 28 was greater than the expected sum by the characteristic m/z signals of N_2 and CO_2. These observations indicate that CO is being formed as a minor carbon-containing product.

Greater selectivity for gaseous N species than for NO_3^- has been reported previously in the electrochemical oxidation of urea[5,7,8] and NH_4^+[23,28]. A lower selectivity toward NO_3^- is beneficial with respect to the chlorine demands exerted by urea which, in turn, should be proportional to the energy consumption in electrochemical systems. Stoichiometric chlorine demands range from 3 to 8 mol mol^{-1} of Cl_2/urea depending on the selectivity. On the contrary, chemical urea chlorinations[3,14] under initial chlorine dosage exceeding 1 mol mol^{-1} of Cl_2/urea have reported much higher relative yields of NO_3^- (up to 40%). The nitrate yields appeared to monotonically increase with the applied chlorine dosage (3 ~ 10 mol mol^{-1} of Cl_2/urea), with observed chlorine demands up to 5 mol mol^{-1} of Cl_2/urea.[3] The NO_3^- is believed to be produced from dichloramine oxidation by RCS,[12,22] which should be more sensitive to the RCS concentration than N_2 generation reactions among chloramines. Therefore, a low yield for NO_3^- in the electrolytic urea degradation can be attributed to a presumable low RCS/urea ratio with pseudo steady-state concentration of RCS. The present results have some practical implications for control of selectivity towards N_2 and NO_3^- in treatment of N-containing wastewater. The

electrochemical urea chlorination with greater selectivity to N_2 can be broadly deployed for remediation of N-rich wastewater (black water from toilet and livestock industry, landfill leachate), aiming at N loading reduction. When focusing on N recovery for fertilizer production, increasing J is expected to elevate the nitrate yield,[29] which is consistent with our observations in this study. In the divided cell experiments under lower J (Figure 2.3), the nitrate yield was estimated to be 3.7% at E_a of 3.0 V NHE. An external RCS generation in a multi-component reactor with flow regulation can be another feasible approach to enhance the nitrate yield.

Despite the higher TN decay rate with respect to the electrolysis time, the magnitude of the TN decrease per unit of passed charge was lower in the single compartment cell than in the divided cell (Figure 2.8) at a given E_a. The lower current efficiency in the absence of the fritted-glass separator can be attributed to quenching reactions of RCS such as cathodic reversion to Cl^- and further oxidation to ClO_3^-.[15,16] When the total passed charge (5936 C) in the single compartment cell experiment was compared with the theoretically required charge for the observed products, the current efficiency was estimated to be 22% for N_2 (6 e^- transfer per molecule), 5.9% for NO_3^- (8 e^-), 7.0% for ClO_3^- (6 e^-), and 1.4% for residual Cl_{DPD} (2 e^-), respectively. The sum of anodic current efficiency (36%) slightly exceeds the η_{RCS} measured in NaCl solutions (30%, Figure 2.2), supporting the hypothetic CO generation as an electron source. The nominal energy consumption in the single compartment cell electrolysis (6 h) was 186 kJ L^{-1}, considerably greater than in biological nitrogen removal process (*ca.* 5 kJ L^{-1}).[2] The relatively intensive energy requirement of electrochemical approaches can be mitigated

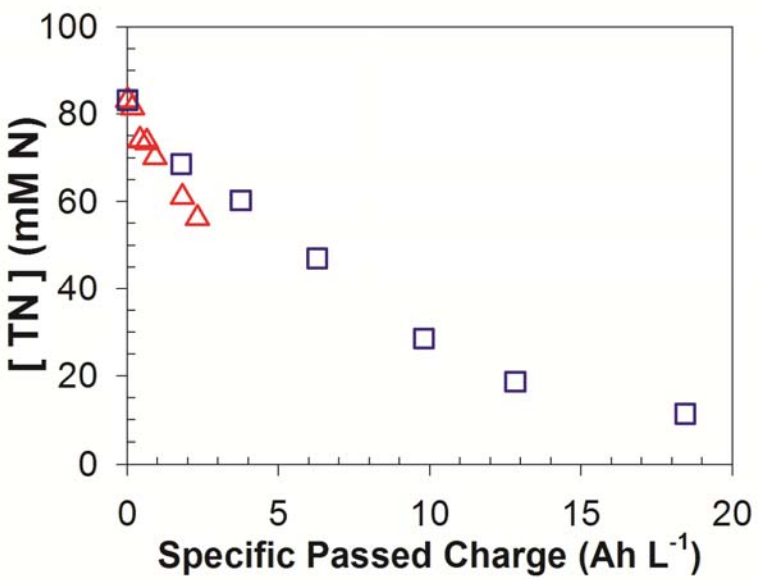

Figure 2.8. Total Nitrogen (TN) concentrations as functions of specific passed charges during potentiostatic electrolysis of 41.6 mM urea solutions with 50 mM Cl^- (60 mL) in a divided (triangle) and single compartment (square) cell; E_a: 3.0 V NHE, anode: BiO_x/TiO_2 (6 cm^2).

by their compatibility with renewable energy sources. For example, our recent report[15] estimated that about 3.5 m^2 of a photovoltaic panel can achieve break-even energy balance in an electrochemical system designed to treat wastewater from a community toilet for 30 users.

2.3.5. Byproducts Formation. The electrolytic urea degradation in the single compartment cell showed that ClO_3^- is a dominant aqueous-phase byproduct, most likely formed by the heterogeneous oxidation of free chlorine (HOCl and ClO^-).[15,16] The [ClO_3^-] increased almost linearly with the electrolysis time (or specific amount of charge passed) until the breakpoint, after which the generation was accelerated (Figure 2.9). The [ClO_3^-] profiles versus specific passed charges did not show a noticeable deviation between the

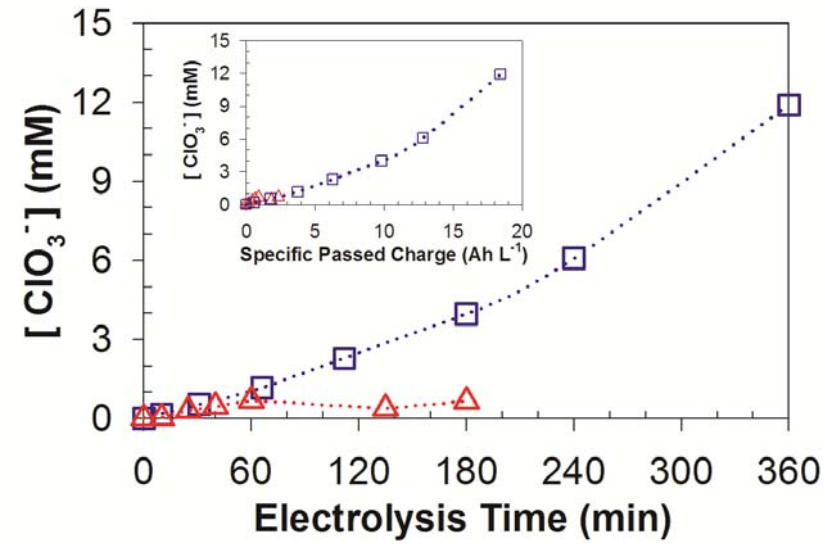

Figure 2.9. Evolutions of ClO_3^- concentration as functions of electrolysis times and (inset) specific passed charges during potentiostatic electrolysis of 41.6 mM urea solutions with 50 mM Cl^- (60 mL) in a divided (triangle) and single compartment (square) cell; E_a: 3.0 V NHE, anode: BiO_x/TiO_2 (6 cm^2).

single component and divided cell. Therefore, the current efficiency of chlorate production is likely more sensitive to the relative amount of potential electron donors to RCS, than it is to *J*. In this study, the ClO_3^- was a stable byproduct without an appreciable concentration of perchlorate ion (ClO_4^-). The ClO_4^- has often been observed by oxidation of ClO_3^- on a boron doped diamond anode.[29] In light of the standard redox potential of the ClO_4^-/ClO_3^- couple (1.19 at pH 0), the production of ClO_4^- is likely to be kinetically limited in our operational condition.

This study could not clearly identify the volatile chlorinated compounds other than NH_2Cl from a time lapse QMS measurement (detection interval: 1 min) of the gas products (Figure 2.5b). The molecular ion signals from m/z 72 to 300 were always lower than the limit of detection (1 ppm). Weak peaks at m/z 51 and 53 could be assigned to

$NH_2{}^{35}Cl$ and $NH_2{}^{37}Cl$. Their maximum ion intensities were always observed at the start-up and then decayed to below the detection limit within 1 h. The peak cluster at m/z 48 to 52 and 64 corresponded to chloromethane ($CH_3{}^{35}Cl$ and $CH_3{}^{37}Cl$), chloroethane ($C_2H_5{}^{35}Cl$), and their fragments. The other detected signals could not be explained in terms of the chlorinated compounds in the database, although they most likely followed fragmentation characteristics of condensed alkanes and alkenes (C_4H_8, C_4H_{10}, C_5H_{10}, and C_5H_{12}), methyl isocyanate (CH_3NCO), oxalic acid ($H_2C_2O_4$), and acetic acid (CH_3COOH). However, these compounds with reduced oxidation states of carbon are not likely to evolve from urea chlorination. Despite a lack of mass spectral data in the library, we suspect that these peak clusters with minor fractions might be ascribed to chlorinated carbamic acids or chlorinated hydrazines as potential reaction intermediates (*vide infra*).

Volatile disinfection byproducts reported in chlorinated swimming pools[30-32] include inorganic chloramines, CNCl, $CHCl_3$, nitriles, and halonitroalkanes, depending on precursor composition and applied Cl_2/N ratio.[32] Owing to the simple molecular structure of urea with fully oxidized carbon, volatile byproducts from chemical urea chlorination were almost exclusively chloramines.[30,33] Although the appreciable chlorinated byproducts from RCS mediated urea oxidation were limited to ClO_3^- and NH_2Cl in this study, a wide array of organics present in human wastes pose a risk of toxicity from other chlorinated byproducts. The harmful byproducts potentially formed during electrochemical treatment of human wastes may limit the reusability of the effluent to non-potable purposes and require post-treatment units. Further investigation is necessary to identify the matrix of by-products and their toxicity in more realistic situations.

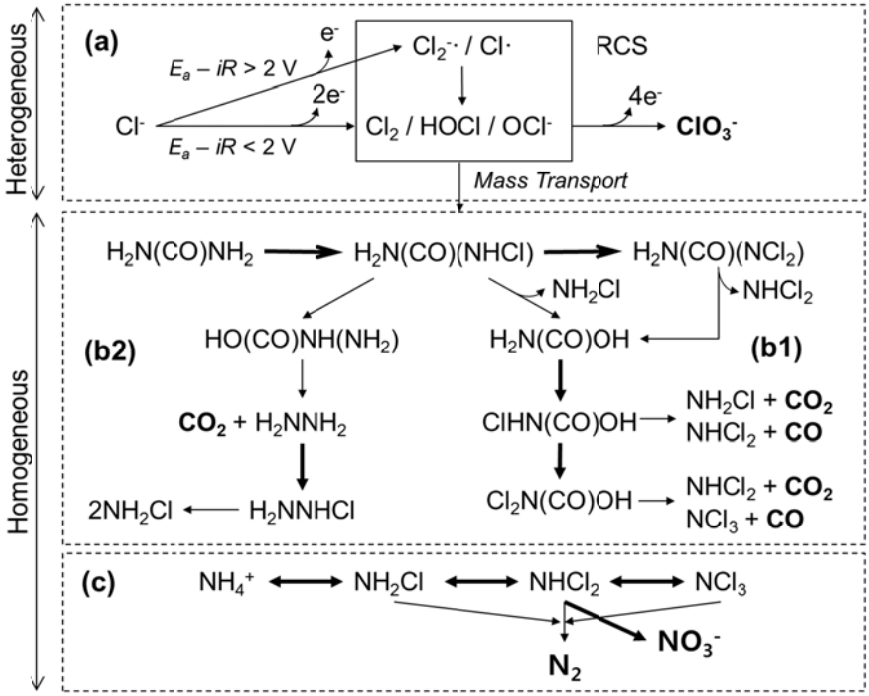

Figure 2.10. Proposed reaction pathways of urea degradation by electrochemically generated reactive chlorine species (RCS); (a) Cl^- oxidation on BiO_x/TiO_2 anode to produce RCS and ClO_3^-, (b1) chlorinated carbamic acids mediated chloramines and CO_2 (CO) generation, (b2) chlorinated hydrazine mediated chloramines and CO_2 generation, and (c) chloramine mediated N_2 and NO_3^- generation. Bold arrows in (b) and (c) represent redox reactions involving the RCS while the final products are specified in bold characters.

2.3.6. Urea Degradation Pathways. Based on the experimental findings, we propose reaction pathways between urea and electrochemically generated RCS as shown in Figure 2.10. The evolution of $[Cl_{DPD}]$ supports chloramines and chloramides as the reaction intermediates. The initial chlorination step appears to be the rate determining since the electron-withdrawing effects of substituted Cl would reduce the bond strength of neighboring amido hydrogen. The overall rate appears to be accelerated by chlorine radicals via hydrogen atom abstraction and rapid addition. A radical driven cleavage of carbonyl double bond or resonance stabilized C-N bond should be minimized in the

initial step, since the dominant carbon end product was observed to be CO_2. The dichlorourea or even monochlorourea will undergo rapid hydrolysis rather than further chlorine substitution,[34] via a pattern similar to base catalyzed haloform reaction, to produce mono-/di-chloramine and carbamic acid. Further chlorinations of the carboxylic intermediates produce more chloramines, CO_2 and presumably CO as a minor product. A generation of hydrazine by a Hoffmann rearrangement of monochlorourea is also feasible,[6] where CO is unlikely to form. The inorganic chloramines undergo a breakpoint chlorination pathway to produce dominantly N_2 or further oxidation to NO_3^- with a lower yield.

2.4. SUPPORTING INFORMATION

2.4.1. Quantification of Molar Flow Rates of Gas Products. The m/z values of 14 and 44 were chosen as characteristic m/z for N_2 and CO_2, respectively. Potential interferences from CO_2, CO and N_2O prohibited the ion intensity of m/z 14 to be used for N_2 quantification. Based on the negligible signal at m/z 30, an interference of N_2O to the signal at m/z 44 was assumed to be marginal. The signal fraction of each characteristic m/z was calculated by the ratio to the sum of ion intensities (m/z 1 to 300). Based on the fragmentation profiles of standard N_2 and CO_2 provided by the supplier, the volume fractions were calculated by the following equations:

$$F_{N_2} = \frac{1080}{72} \frac{I_{14}}{\sum_{1}^{300} I_i} F_T \quad \text{(m/z 28:14:29 = 1000:72:8)} \tag{2.4}$$

$$F_{CO_2} = \frac{1199}{1000}\frac{I_{44}}{\sum_{1}^{300} I_i} F_T \quad \text{(m/z 44:28:16 = 1000:114:85)} \tag{2.5}$$

where, I_i is ion intensity of fragment m/z *i*, while F_{N2}, F_{CO2}, and F_T represent the molar flow rate of N_2, CO_2, and total gaseous products, respectively. F_T was calculated by converting the observed volumetric flow rate using ideal gas law, while considering conversion factors of the major gas components (1.4 for Ar, *ca.* 1 for H_2, O_2, N_2, H_2O).

$$F_T = \left(\frac{X_{Ar}}{1.4} + \frac{1 - X_{Ar}}{1} \right)^{-1} \frac{P}{RT} Q_{obs} \tag{2.6}$$

where, X_{Ar} is the volumetric fraction of Ar, Q_{obs} is the observed volumetric flow rate of total gaseous products, P is the operational pressure (1 atm), R is the gas constant, and T is the operational temperature (293 K).

2.4.2. Measurement of Urea Concentration. Figure 2.11 shows the evolution of the urea concentration under variable current density conditions, which was measured by urease hydrolysis method.[16] The measured urea concentration dropped off for the first sample under potential bias, whose further decrease was marginal. The required charge for the decrease in urea concentration for the initial 10 min exceeded the total passed charge, even when assuming one electron transfer for the urea transformation. The presence of reactive chlorine species (RCS), even with a trace concentration, would inhibit the activity of the enzyme urease.[20] In addition, the RCS was found to interfere in the spectrometric urea analysis by diacetylmonoxime.[35] The color generation by the reagent addition appeared to increase with the electrolysis time.

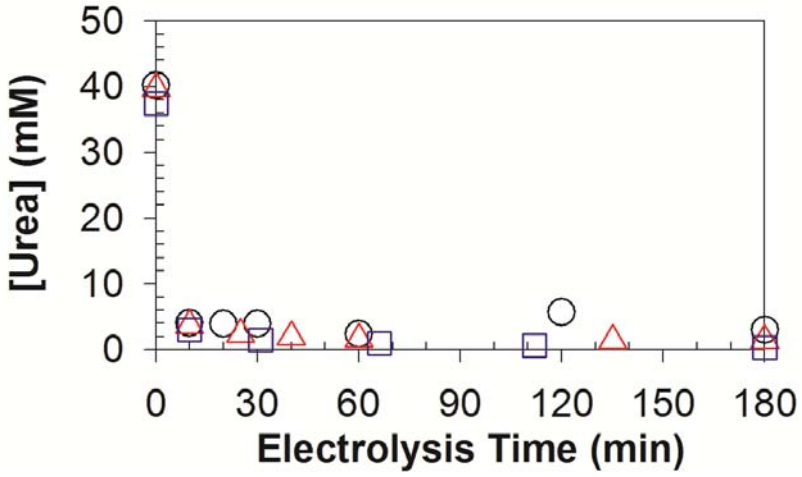

Figure 2.11. Time profiles of urea concentration during potentiostatic electrolysis of 41.6 mM urea solutions with 50 mM Cl^- (60 mL) as control; E_a: (circle) 2.2 V NHE in divided cell, (triangle) 3.0 V NHE in divided cell, (square) 3.0 V NHE in single compartment cell.

2.5. REFERENCES

(1) Rollinson, A. N.; Jones, J.; Dupont, V.; Twigg, M. V. Urea as a hydrogen carrier: a perspective on its potential for safe, sustainable and long-term energy supply. *Energy & Environmental Science* **2011,** *4* (4), 1216-1224.

(2) Maurer, M.; Pronk, W.; Larsen, T. A. Treatment processes for source-separated urine. *Water Research* **2006,** *40* (17), 3151-3166.

(3) De Laat, J.; Feng, W. T.; Freyfer, D. A.; Dossier-Berne, F. Concentration levels of urea in swimming pool water and reactivity of chlorine with urea. *Water Research* **2011,** *45* (3), 1139-1146.

(4) *Clean watersheds needs survey: report to congress*; EPA-832-R-10-002; United States Environmental Protection Agency: Washington, DC., 2008.; water.epa.gov/scitech/datait/databases/cwns/upload/cwns2008rtc.pdf.

(5) Amstutz, V.; Katsaounis, A.; Kapalka, A.; Comninellis, C.; Udert, K. M. Effects of carbonate on the electrolytic removal of ammonia and urea from urine with thermally prepared IrO_2 electrodes. *Journal of Applied Electrochemistry* **2012,** *42* (9), 787-795.

(6) Simka, W.; Piotrowski, J.; Robak, A.; Nawrat, G. Electrochemical treatment of aqueous solutions containing urea. *Journal of Applied Electrochemistry* **2009,** *39* (7), 1137-1143.

(7) Hernlem, B. J. Electrolytic destruction of urea in dilute chloride solution using DSA electrodes in a recycled batch cell. *Water Research* **2005,** *39* (11), 2245-2252.

(8) Kim, J.; Choi, W. J. K.; Choi, J.; Hoffmann, M. R.; Park, H. Electrolysis of urea and urine for solar hydrogen. *Catalysis Today* **2013,** *199*, 2-7.

(9) Boggs, B. K.; King, R. L.; Botte, G. G. Urea electrolysis: direct hydrogen production from urine. *Chemical Communications* **2009,** (32), 4859-4861.

(10) Vedharathinam, V.; Botte, G. G. Understanding the electro-catalytic oxidation mechanism of urea on nickel electrodes in alkaline medium. *Electrochimica Acta* **2012,** *81*, 292-300.

(11) Yan, W.; Wang, D.; Botte, G. G. Electrochemical decomposition of urea with Ni-based catalysts. *Applied Catalysis B-Environmental* **2012,** *127*, 221-226.

(12) Jara, C. C.; Di Giulio, S.; Fino, D.; Spinelli, P. Combined direct and indirect electroxidation of urea containing water. *Journal of Applied Electrochemistry* **2008,** *38* (7), 915-922.

(13) Simka, W.; Piotrowski, J.; Nawrat, G. Influence of anode material on electrochemical decomposition of urea. *Electrochimica Acta* **2007,** *52* (18), 5696-5703.

(14) Blatchley, E. R.; Cheng, M. M. Reaction mechanism for chlorination of urea. *Environmental Science & Technology* **2010,** *44* (22), 8529-8534.

(15) Cho, K.; Qu, Y.; Kwon, D.; Zhang, H.; Cid, C. A.; Aryanfar, A.; Hoffmann, M. R. Effects of anodic potential and chloride ion on overall reactivity in electrochemical reactors designed for solar-powered wastewater treatment. *Environmental Science & Technology* **2014,** *48* (4), 2377-2384.

(16) Cho, K.; Kwon, D.; Hoffmann, M. R. Electrochemical treatment of human waste coupled with molecular hydrogen production. *Rsc Advances* **2014,** *4* (9), 4596-4608.

(17) Bergmann, M. E. H.; Koparal, A. S. Studies on electrochemical disinfectant production using anodes containing RuO_2. *Journal of Applied Electrochemistry* **2005,** *35* (12), 1321-1329.

(18) Wilsenach, J. A.; Schuurbiers, C. A. H.; van Loosdrecht, M. C. M. Phosphate and potassium recovery from source separated urine through struvite precipitation. *Water Research* **2007,** *41* (2), 458-466.

(19) Revilla, M.; Alexander, J.; Glibert, P. M. Urea analysis in coastal waters: comparison of enzymatic and direct methods. *Limnology and Oceanography-Methods* **2005,** *3*, 290-299.

(20) Ikematsu, M.; Kaneda, K.; Iseki, M.; Yasuda, M. Electrochemical treatment of human urine for its storage and reuse as flush water. *Science of the Total Environment* **2007,** *382* (1), 159-164.

(21) Shang, C.; Gong, W. L.; Blatchley, E. R. Breakpoint chemistry and volatile byproduct formation resulting from chlorination of model organic-N compounds. *Environmental Science & Technology* **2000,** *34* (9), 1721-1728.

(22) Jafvert, C. T.; Valentine, R. L. Reaction scheme for the chlorination of ammoniacal water. *Environmental Science & Technology* **1992,** *26* (3), 577-586.

(23) Kapalka, A.; Katsaounis, A.; Michels, N. L.; Leonidova, A.; Souentie, S.; Comninellis, C.; Udert, K. M. Ammonia oxidation to nitrogen mediated by electrogenerated active chlorine on Ti/PtO_x-IrO_2. *Electrochemistry Communications* **2010,** *12* (9), 1203-1205.

(24) Bunce, N. J.; Bejan, D. Mechanism of electrochemical oxidation of ammonia. *Electrochimica Acta* **2011,** *56* (24), 8085-8093.

(25) Deborde, M.; von Gunten, U. Reactions of chlorine with inorganic and organic compounds during water treatment - Kinetics and mechanisms: A critical review. *Water Research* **2008,** *42* (1-2), 13-51.

(26) Park, H.; Vecitis, C. D.; Hoffmann, M. R. Electrochemical water splitting coupled with organic compound oxidation: The role of active chlorine species. *Journal of Physical Chemistry C* **2009,** *113* (18), 7935-7945.

(27) Neta, P.; Huie, R. E.; Ross, A. B. Rate constants for reactions of inorganic radicals in aqueous-solution. *Journal of Physical and Chemical Reference Data* **1988,** *17* (3), 1027-1284.

(28) Kim, K. W.; Kim, Y. J.; Kim, I. T.; Park, G. I.; Lee, E. H. Electrochemical conversion characteristics of ammonia to nitrogen. *Water Research* **2006,** *40* (7), 1431-1441.

(29) Peez, G.; Saiz, J.; Ibanez, R.; Urtiaga, A. M.; Ortiz, I. Assessment of the formation of inorganic oxidation by-products during the electrocatalytic treatment of ammonium from landfill leachates. *Water Research* **2012,** *46* (8), 2579-2590.

(30) Li, J.; Blatchley, E. R. Volatile disinfection byproduct formation resulting from chlorination of organic-nitrogen precursors in swimming pools. *Environmental Science & Technology* **2007,** *41* (19), 6732-6739.

(31) Judd, S. J.; Bullock, G. The fate of chlorine and organic materials in swimming pools. *Chemosphere* **2003,** *51* (9), 869-879.

(32) Weaver, W. A.; Li, J.; Wen, Y. L.; Johnston, J.; Blatchley, M. R.; Blatchley, E. R. Volatile disinfection by-product analysis from chlorinated indoor swimming pools. *Water Research* **2009,** *43* (13), 3308-3318.

(33) Schmalz, C.; Frimmel, F. H.; Zwiener, C. Trichloramine in swimming pools - Formation and mass transfer. *Water Research* **2011,** *45* (8), 2681-2690.

(34) Chattaway, F. D. The action of chlorine upon urea whereby a dichloro urea is produced. *Proceedings of the Royal Society of London Series a-Containing Papers of a Mathematical and Physical Character* **1908,** *81* (549), 381-388.

(35) Prescott, L. M.; Jones, M. E. Modified methods for determination of carbamyl aspartate. *Analytical Biochemistry* **1969,** *32* (3), 408-419.

Chapter 3

EFFECTS OF ANODIC POTENTIAL AND CHLORIDE ION ON OVERALL REACTIVITY IN ELECTROCHEMICAL REACTORS DESIGNED FOR SOLAR-POWERED WASTEWATER TREATMENT

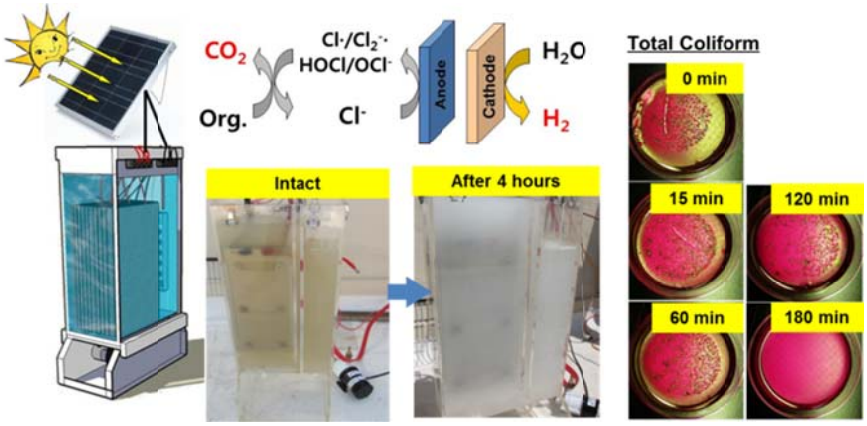

Sections reprinted with permission from Kangwoo Cho, Yan Qu, Daejung Kwon, Hao Zhang, Clement A. Cid, Asghar Aryanfar, and Michael R. Hoffmann *Environmental Science and Technology* **2014**, *48* (4), 2377-2384.

ABSTRACT

We have investigated the electrochemical treatment of real domestic wastewater coupled with the simultaneous production of molecular H_2 as a useful byproduct. The electrolysis cells employ multilayer semiconductor anodes with electroactive bismuth-doped TiO_2 functionalities and stainless steel cathodes. DC-powered laboratory-scale electrolysis experiments were performed under static anodic potentials (+2.2 or +3.0 V NHE) using domestic wastewater samples, with an added chloride ion in variable concentrations. Greater than 95% reductions in chemical oxygen demand (COD) and ammonium ion were achieved within 6 h. In addition, we experimentally determined a decreasing overall reactivity of reactive chlorine species toward COD with an increasing chloride ion concentration under chlorine radicals ($Cl\cdot$, $Cl_2^{-}\cdot$) generation at +3.0 V NHE. The current efficiency for COD removal was 12%, with the lowest specific energy consumption of 96 kWh $kgCOD^{-1}$ at the cell voltage near 4 V in 50 mM chloride. The current efficiency and energy efficiency for the H_2 generation were calculated to range from 34 to 84% and 14 to 26%, respectively. The hydrogen comprised 35 to 60% by volume of evolved gases. The efficacy of our electrolysis cell was further demonstrated by a 20 L prototype reactor totally powered by a photovoltaic (PV) panel, which was shown to eliminate COD and total coliform bacteria in less than 4 h of treatment.

3.1. INTRODUCTION

Sanitation in developing or emerging countries has been considered woefully inadequate, as illustrated by the fact that more than 1.8 million children under five years old die from waterborne diseases every year.[1] In developing countries, there is often a deficit of critical infrastructure, including electricity distribution grids and subsurface sewers that requires self-standing sanitation facilities for handling human waste. Given these circumstances, we describe and test a photovoltaic (PV) powered wastewater electrolysis cell (PWEC), which has been designed to couple the electrochemical treatment of wastewater with the production of molecular H_2 as a potentially useful byproduct. Application of modified PWEC may eventually lead to improved human sanitation in peri-urban regions, rural areas, or more remote locations that are currently lacking in conventional urban infrastructure and proper sanitation facilities.

In wastewater electrolysis cells (WEC), environmental pollutants can be eliminated either by the direct heterogeneous or indirect homogeneous oxidation pathway.[2] Surface-bound reactive oxygen species (ROS) are intermediates in O_2 evolution during water splitting, which may also result in the direct oxidation of chemical substrates.[3] ROS also reacts with chloride in wastewater to produce reactive chlorine species (RCS) such as free chlorine (Cl_2, HOCl, ClO^-) and chlorine radical species ($Cl\cdot$, $Cl_2^{-}\cdot$).[4,5] Organic substrates can be converted via reactions with RCS to CO_2 and an array of lower molecular weight carboxylic acids.[6] At the same time, with sufficient RCS generation, disinfection of fecal coliform bacteria can be achieved. Inexpensive polycrystalline photovoltaic (PV) panels can be used to convert incident solar irradiation into a direct

current (DC) potential across anode/cathode pairs to produce ROS.[7] Water oxidation at the anode is balanced in part by water/proton reduction at the cathode to produce H_2.

Electrochemical systems have often been investigated for treatment of model organic compounds or industrial wastewater using boron-doped diamond or mixed metal oxides electrode based on IrO_2 and RuO_2, mostly focusing only on anodic pollutants removal in DC-powered reactors.[3,4] In line with our previous reports[5-8] on the multifunctional approach of WEC with bismuth-doped TiO_2 anodes for wastewater treatment and molecular H_2 production, we first report the efficacy with real domestic wastewater by benchtop WEC and prototype PWEC experiments. While an existence of various reactive oxidants has been usually inferred based on the cell voltage,[5] this study employed potentiostatic electrolysis with monitoring of anodic/cathodic potential and ohmic loss. The experimental approach of this study provides more plausible explanations for the role of various oxidants in reference to their thermodynamic potentials.

3.2. EXPERIMENTAL SECTION

3.2.1. Electrode Module. The semiconductor anodes employed in this study were prepared according to a basic procedure described in our previous reports.[6,9] The procedure includes sequential thermal decomposition of mixed metal oxides including $Ir_{0.73}Ta_{0.27}O_x$, $Sn_{0.9}Bi_{0.1}O_x$, $Ti_{0.96}Bi_{0.04}O_x$, and $Ti_{0.66}Bi_{0.33}O_x$ on conductive Ti metal plates. An electron probe microanalysis[10] indicates that the outer surface of the synthesized electrodes is composed mainly of bismuth, titanium, and oxygen (BiO_x/TiO_2). The underlying layers involving the oxides of Ir, Ta, and Sn are reported to enhance the

stability and conductivity of the electrode.[9] The electrode module used for laboratory experiments consists of the BiO_x/TiO_2 anode (2.7 cm × 2 cm), stainless steel (SS) cathode (Hastelloy C-22, 2.7 cm × 2 cm), and Ag/AgCl/Sat. KCl reference electrode (BaSi Inc., USA). The distance between anode and cathode was 5 mm, while the frit tip of the reference electrode was located 2 mm apart from the center of the anode.

3.2.2. Characterization of the BiO_x/TiO_2 Anode. Cyclic voltammetry (CV) profiles were collected over a range of 0 to 2.0 V NHE by three repetitive scans (5 mV sec^{-1}) in quiescent 30 mM NaCl solution. In benchtop reactors, the electrode module was installed in a single compartment cell with working volume of 60 mL. A potentiostat (Bio-Logic, France) was used for controlling applied anodic potential (E_a) versus reference electrode, monitoring the response current (I) and the cathodic potential (E_c) versus reference electrode.

3.2.3. DC Powered Wastewater Electrolysis. Potentiostatic WEC experiments using domestic wastewater were performed under variable E_a and added electrolyte (NaCl) concentrations. The applied anodic potentials, E_a, were fixed either at 2.2 or 3.0 V NHE versus the reference electrode. The ohmic resistance between anode and reference electrode (R) was measured by current interruption method[11] with current bias of 200 mA, to estimate actual anodic potential ($E_a - iR$). Residential-strength wastewater samples were collected from the effluent line of a primary settling tank at the San Jose Creek Wastewater Treatment Plant (Whittier, CA, USA). The wastewater samples were stored at 4 ºC, and the supernatant after settling was used. The composition of the intact wastewater is given in Table 3.1. In rural areas, wastewater salinity and chloride

Table 3.1. Composition of residential-strength wastewater used in this study.

Constituent	Mean	COV (%)
pH	6.6 – 7.3	–
COD (mg L^{-1})	180	6.02
TN (mM N)	2.594	7.96
NH_4^+ (mM)	1.910	5.19
NO_3^- (mM)	< 0.01	–
Cl^- (mM)	3.880	–
ClO_3^- (mM)	< 0.01	–
Mg^{2+} (mM)	0.6387	1.96
Ca^{2+} (mM)	1.287	1.38

COV: Coefficient of Variation.

concentrations are normally higher than in urban areas.[12] Therefore, moderate amounts of NaCl were added with the added chloride concentrations ($[Cl^-]_{ext.}$) ranging from 0 to 50 mM. During the wastewater electrolysis, the wastewater electrolyte was stirred at 600 rpm by a magnetic bar (0.8 cm diameter × 1.8 cm). Over reaction durations of 200 to 230 min, gaseous products were collected in a graduated buret to determine average volumetric flow rates. The volumetric H_2 fraction in the collected gas was determined by a GC-TCD (Hewlett-Packard, USA), using a 5 V/V% H_2 standard gas for calibration.

3.2.4. Prototype PV Powered Wastewater Electrolysis. A 20 L WEC powered by a PV panel was tested in roof-top experiments in order to assess the feasibility of PV panels as the sole source of energy for COD elimination and disinfection due to *in situ* RCS generation. The PWEC system had an anode/cathode array module consisting of five doubly coated BiO_x/TiO_2 anodes and six SS cathodes (40 × 20 cm^2 each) with a distance of separation between each anode and cathode pair of 0.2 cm. A commercially available,

low-cost polycrystalline PV panel (Silicon Solar Inc., USA) was employed. More details are described in the Supporting Information. Twenty liters of wastewater with added NaCl of 50 mM was mixed with a circulation pump connected to the bottom of the reactor at the rate of 25 L min^{-1}. The $E_a - E_c$, and the current were periodically monitored using multimeters (Fluke, USA).

3.2.5. Analysis. COD and total nitrogen (TN) concentration of samples were measured based on the absorbance at 420 nm in UV-vis spectrophotometer (Agilent, USA), after digestion in a low-range dichromate digestion solution (3 – 150 mg L^{-1}, Hach, USA) and in a low-range TN reagent set (0.5 – 25 mgN L^{-1}, Hach, USA), respectively. Anions (Cl^-, ClO_3^-, NO_3^-,) and cations (NH_4^+, Ca^{2+}, Mg^{2+}) were simultaneously determined by ion chromatography (Dionex, USA), using anion-exchange column (Ionpac AS 19) and cation-exchange column (Ionpac CS 16). The total chlorine (Cl_{DPD}) was measured using DPD (N,N-diethyl-p-phenylenediamine) reagent (Hach, USA) coupled with quantification via absorbance measurements at 530 nm. A standard wastewater membrane filtration method was used to count the number of total coliforms and fecal coliforms during electrolysis (details in the Supporting Information).

3.3. RESULTS AND DISCUSSION

3.3.1. Characteristics of the BiO_x/TiO_2 Anodes. Figure 3.1 shows CV plots for the BiO_x/TiO_2 anode in a 30 mM NaCl electrolyte solution. The onset potential, which corresponds to 1 A m^{-2} of current density, initially appeared at near 1.2 V. In comparison to the reduction potential of O_2/H_2O couple at pH 7 (Table 3.2), the observed onset potential estimated oxygen evolution overpotential of 0.38 V. This value is quite

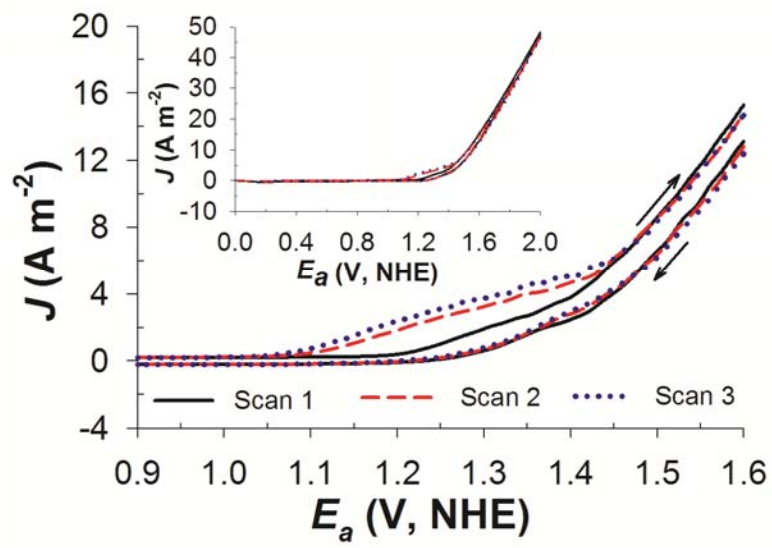

Figure 3.1. Cyclic voltammetry of the BiO_x/TiO_2 anode in 30 mM NaCl solution with three repetitive scans at a scan rate of 5 mV sec^{-1}. The full scans from 0 to 2 V NHE are shown in the inset figure.

Table 3.2. Reduction potential (E) at pH 7 and standard reduction potential (E^0) at pH 0 for several redox couples involved in the electrochemical reactions.

Redox Couple	at pH 7 (V NHE)	at pH 0 (V NHE)
O_2/H_2O	0.82	
Cl_2/Cl^-	1.36	1.36
$HOCl/Cl^-$		1.48
ClO^-/Cl^-		0.81
$Cl\cdot/Cl^-$		2.4
$Cl_2^-\cdot/Cl^-$		2.0
ClO_3^-/Cl_2	0.97	
$ClO_3^-/HOCl$	0.92	
ClO_3^-/ClO^-	0.94	

comparable to RuO_2 and IrO_2 based electrodes,[13] demonstrating that the BiO_x/TiO_2 electrode can be regarded as an active electrode for oxygen evolution. The activity may be attributed to intrinsic oxide vacancies of Bi_2O_3 in the lattice structure, which can facilitate the transition of surface-bound hydroxyl radicals to higher oxides.[14] Although a chloride oxidation peak is hidden by the large anodic wave from the oxygen evolution, chloride oxidation is generally accepted to produce Cl_2.[15,16] The Cl_2 will be in equilibrium with HOCl and ClO^- in bulk aqueous phase depending on the specific pH.[17] On the other hand, the second and third scan showed a significant decrease of the onset potential to 1.05 V, which would result from a formation of chlorate.[6] The ClO_3^- is known to be produced electrochemically either by oxidation of chloride or free chlorine (HOCl or ClO^-).[18,19] The decrease in onset potential in Figure 3.1 suggests that the chlorate is produced by the oxidation of the RCS[20] which requires four electrons for free chlorine oxidation.

As shown in Table 3.3, the current and ohmic drop between electrodes increases along with the chloride concentration and applied potential. As a result, actual anodic potential ($E_a - iR$) with 50 mM of chloride (H50) was smaller than those with lower added chloride (H10 and H30), while marginally higher than at lower E_a (L30 and L50). Another important observation was that a substantial cathodic potential is required to maintain the E_a; *i.e.*, the $E_a - E_c$ approaches about twice of the E_a. Consequently, the power consumption grows as the E_a or $[Cl^-]_{ext.}$ increases under the potentiostatic conditions.

Table 3.3. The *iR*-compensated anodic potential ($E_a - iR$), cell voltage ($E_a - E_c$), current density (J), and power consumption (P) on average under variable applied anodic potential (E_a; L: 2.2 V, H: 3.0 V NHE) and added Cl^- concentration ($[Cl^-]_{ext.}$; 0, 10, 30, 50 mM) in electrolysis experiments using domestic wastewater samples.

ID	$[Cl^-]_{ext.}$ (mM)	E_a (V NHE)	$E_a - iR$ (V NHE)	$E_a - E_c$ (V)	J (A m^{-2})	P (W)
L30	30	2.2	1.92 (2.8)	4.03 (0.94)	74.2 (19)	0.161 (20)
L50	50	2.2	1.96 (2.0)	3.88 (0.94)	89.4 (17)	0.188 (18)
H0	0	3.0	2.08 (5.8)	6.27 (1.2)	80.9 (13)	0.274 (14)
H10	10	3.0	2.24 (4.9)	5.56 (0.72)	110 (14)	0.367 (15)
H30	30	3.0	2.25 (4.8)	5.88 (0.72)	206 (14)	0.655 (15)
H50	50	3.0	2.00 (4.5)	5.37 (0.17)	296 (9.1)	0.953 (9.2)

Values in parentheses show coefficient of variation (%).

Figure 3.2 illustrates the current density as a function of $[Cl^-]$ during the wastewater electrolysis. At a given E_a and $[Cl^-]_{ext}$, the J was almost proportional to the $[Cl^-]$. Provided that the generation of RCS and oxygen accounts for the anodic electron transfer, it can be inferred that the rate of RCS generation is first-order in $[Cl^-]$, as reported previously for chlorine generation on RuO_2 anodes.[15,16] The apparent first-order kinetic on $[Cl^-]$ may also be a consequence of mass transport limitation. In addition, the rate of oxygen evolution can be also influenced by $[Cl^-]$. A decrease in $[Cl^-]$ should result in a decrease in the electrolyte conductivity and exchange current density for oxygen evolution.

3.3.2. Impact of E_a and $[Cl^-]_{ext.}$ on COD Removal. Figure 3.3 illustrates the effects of E_a on COD degradation under $[Cl^-]_{ext.}$ fixed either at 30 mM or 50 mM. Wastewater

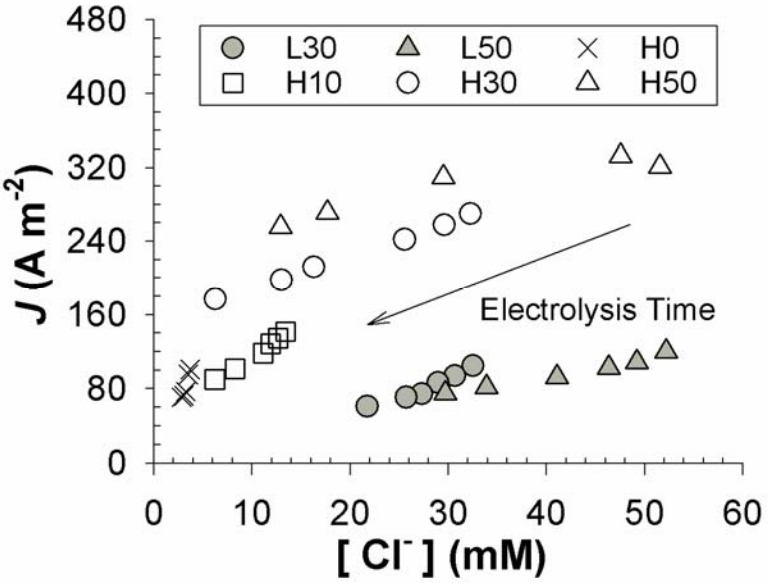

Figure 3.2. Evolution of current densities along with variations in Cl^- concentration under variable applied anodic potential (L: 2.2 V, H: 3.0 V NHE) and added Cl^- concentration (0, 10, 30, 50 mM) in electrolysis experiments using domestic wastewater samples. The arrow indicates an arbitrary varying direction as a function of time.

samples often contain refractory organics that are not detected as COD initially. The recalcitrant substrates are over time transformed by reactions with RCS to yield intermediate products that are more susceptible to the dichromate digestion, as indicated by a slight initial increase of COD.[21,22] When the COD concentration profiles were fit to pseudo-first-order kinetics, the rate constant increased with an increase in E_a. These results are consistent with COD removal in the low E_a that is limited by anodic electron transfer (heterogeneous RCS generation). Under the electron-transfer-limited regime, increasing cell voltage or the current density normally enhances the rate of pollutant degradation, except for those interfacial reactions that are controlled by mass transport.[13,20,22,23]

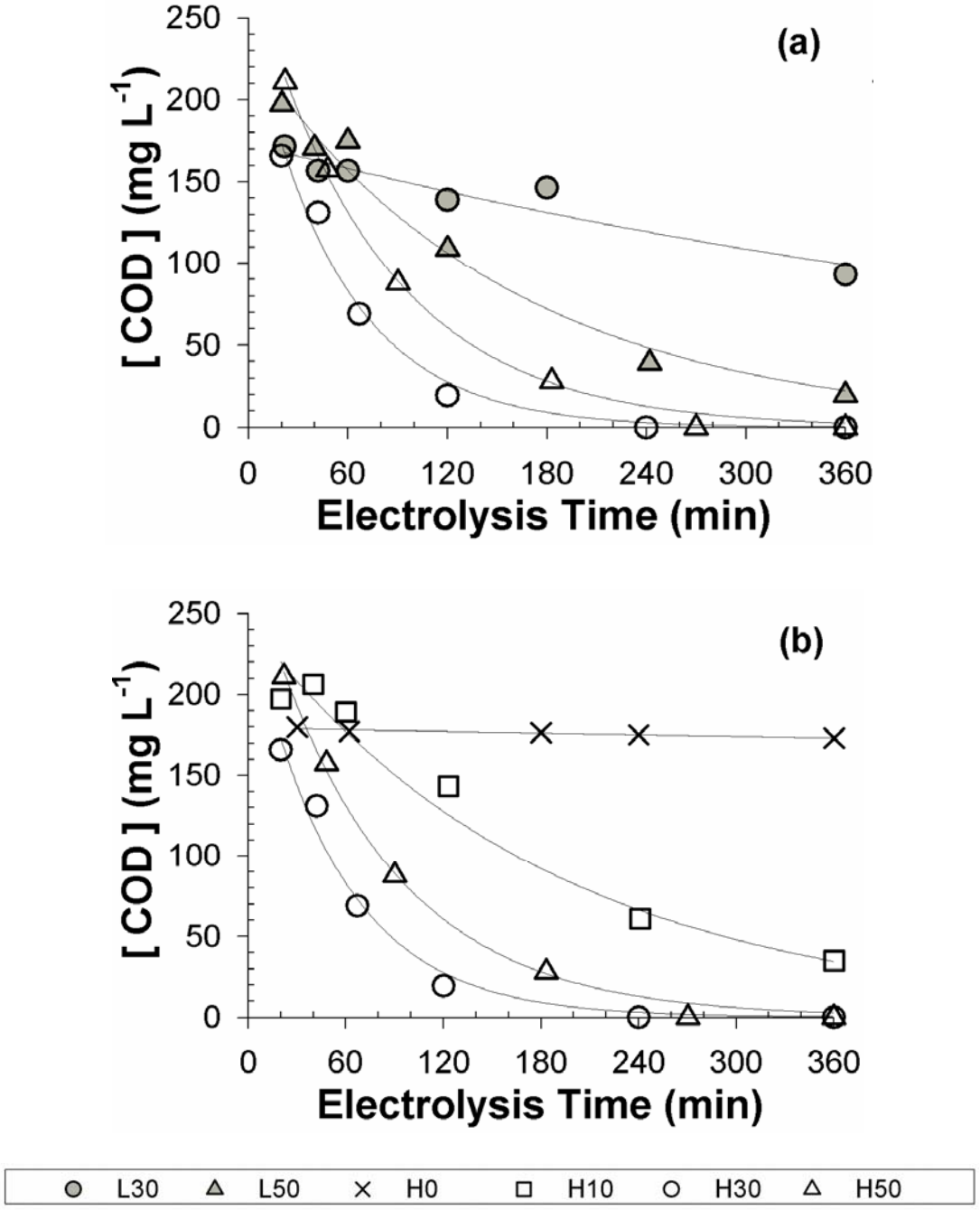

Figure 3.3. Time profiles of COD concentration under variable applied anodic potential (L: 2.2 V, H: 3.0 V NHE) and added Cl^- concentration (0, 10, 30, 50 mM) in electrolysis experiments using domestic wastewater samples. Time profile for each condition is regressed with a pseudo-first-order kinetic equation.

The effects of $[Cl^-]_{ext.}$ on COD removal at the high E_a (3.0 V NHE) are shown in Figure 3.3b. In this case, COD removal was not observed without the Cl^-, which indicates that direct oxidation via surface-bound hydroxyl radicals is a minor pathway on the BiO_x/TiO_2 electrode, as in the case of the RuO_x/TiO_2 electrode.[23-25] In contrast, elimination of measurable COD took less than 6 h with $[Cl^-]_{ext.}$ exceeding 10 mM. The pseudo-first-order rate constant for COD removal increased with increasing $[Cl^-]_{ext.}$ in the range of 10 mM to 30 mM, while a decrease in the rate of COD consumption was observed in the range of $[Cl^-]_{ext.}$ from 30 mM to 50 mM, even though there was an increase in J (Table 3.3). As a consequence, the net current efficiency (CE) for COD oxidation in H50 was smaller than in H10. This observation is contrary to some reports that increasing $[Cl^-]$ always enhances the rate and CE of COD removal[25-27] by increasing the overall rate of oxidants generation.[28] However, other studies report observed negligible[13,24,29] or adverse effects of $[Cl^-]$ in the range exceeding 30 mM, which were ascribed to pH decrease in the vicinity of the anode with increasing current density. The shift in the local pH may effectively shift the RCS speciation toward gaseous chlorine,[17] which results in a net loss of RCS. In this study, however, the bulk pH slightly increased from circum-neutral to ~9 in maximum along with the electrolysis. Therefore, we argue that there is a change in the speciation of RCS versus $[Cl^-]_{ext.}$ with corresponding shifts in the relative reactivity toward COD oxidation, which was not explained by the pH effects.

3.3.3. Impact of Cl· and Cl_2^{-}· on COD Removal. The effects of $[Cl^-]_{ext.}$ were interpreted using a simple kinetic model applied to the data of experiments H10, H30, and H50. The CV profiles (Figure 3.1) suggested that the oxidation of Cl^- produces RCS and chlorate in series. The oxidation of Cl^- and RCS as well as the homogeneous reaction

between the RCS and COD were assumed to be first order in each reactant.[19,24,27] The linear dependence of J on the [Cl^-] (Figure 3.2) is consistent with first-order kinetics for RCS generation as follows:

$$\frac{d[RCS]}{dt} = k_1[Cl^-] - k_2[RCS]_{SS}[COD] - k_3[RCS]_{SS} \approx 0 \quad (3.1)$$

$$\frac{d[COD]}{dt} = -k_2[RCS]_{SS}[COD] \approx -k_{COD}[COD] \quad (3.2)$$

$$\frac{d[ClO_3^-]}{dt} = k_3[RCS]_{SS} \approx k_{ClO_3^-} \quad (3.3)$$

$$k_2 = k_3 \frac{k_{COD}}{k_{ClO_3^-}} \quad (3.4)$$

where, k_1, k_2, and k_3 are rate constant for heterogeneous Cl^- oxidation to RCS, homogeneous reaction between RCS and COD, and heterogeneous RCS oxidation to chlorate. In addition, we assume a pseudo-steady-state condition for the rate of RCS production. The total chlorine concentration was negligible when the COD concentration was higher than 100 mg L^{-1} (Figure 3.4a). A linear relationship between [Cl^-] and [COD], indicated by eq 3.1 with quasi-constant [RCS], is supported by Figure 3.4b. Furthermore, the steady-state assumption for [RCS] is self-consistent with the decrease in [COD] versus time, which follows apparent pseudo-first-order kinetics (Figure 3.3). Therefore, the pseudo-first-order rate constant for COD removal (k_{COD}) and the pseudo-zero-order rate constant for chlorate production ($k_{ClO_3^-}$) can be expressed as the steady-state RCS concentration ($[RCS]_{SS}$) multiplied by the reactivity of the RCS toward the COD (k_2)

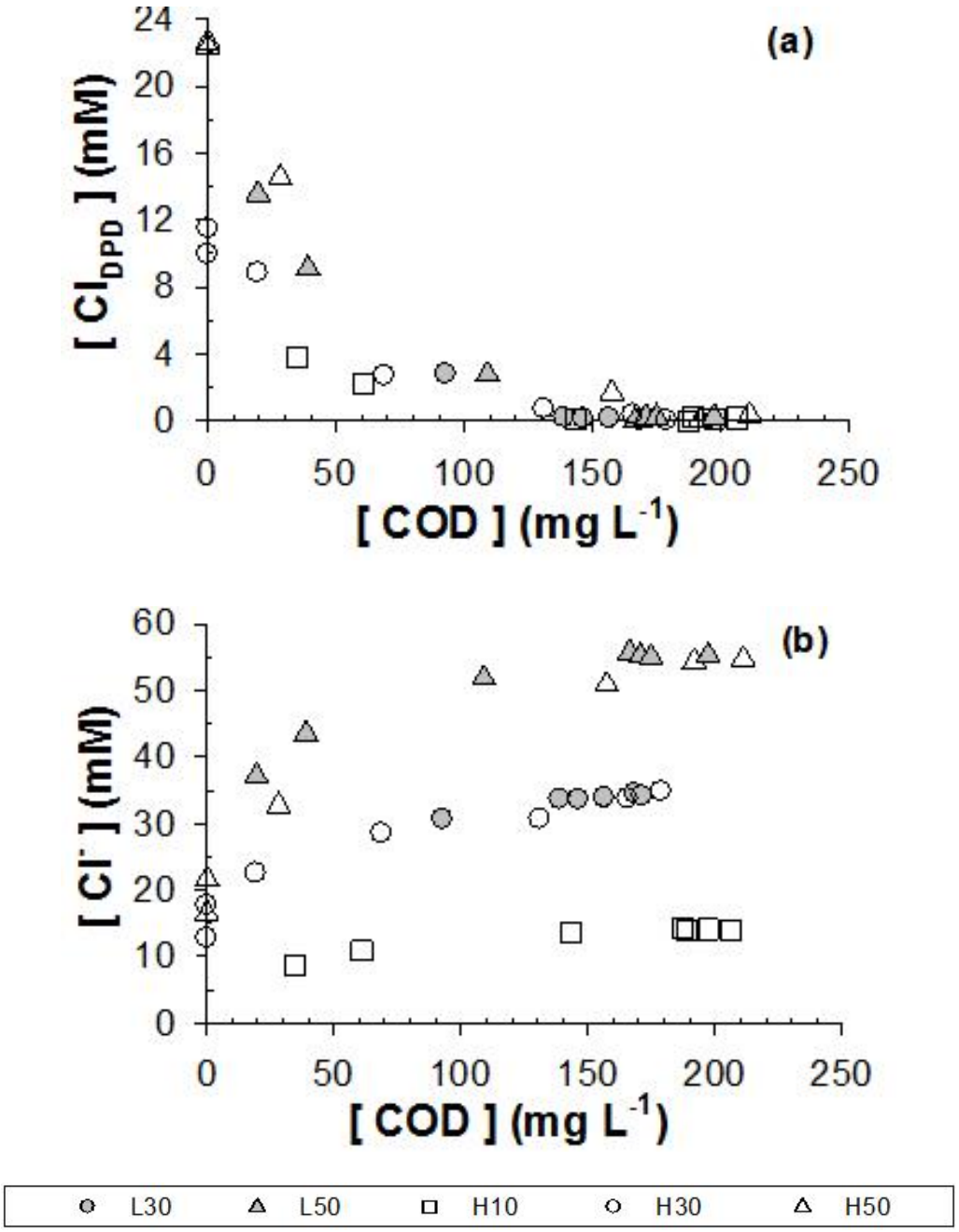

Figure 3.4. Evolutions of (a) total chlorine (Cl_{DPD}) and (b) Cl^- concentration as functions of variations in COD concentration under variable applied anodic potential (L: 2.2 V, H: 3.0 V NHE) and added Cl^- concentration (10, 30, 50 mM) in electrolysis experiments using domestic wastewater samples.

and heterogeneous rate constant (k_3), respectively. It could be argued that the heterogeneous rate constants, k_1 and k_3, should vary with the electrolysis time as given by the Butler-Volmer formulation.[11] However, relatively low variations in $E_a - iR$ (Table 3.3) are consistent with the assumption that k_1 and k_3 are essentially constant. Our recent report[6] demonstrated that the chloride oxidation kinetics are governed by consistent parameters regardless of initial chloride concentration during potentiostatic (E_a: 3 V NHE) electrolyses in NaCl solutions. The heterogeneous reactions on the metal oxide semiconductors are often controlled by rate constants between surface ROS and substrates that are independent of anodic potential.[2]

Figure 3.5 shows [ClO_3^-] increasing faster after depletion of [COD]. Nevertheless, the rate of ClO_3^- formation appeared almost constant when the steady-state assumption for [RCS] was valid, as shown in Figure 3.5 (inset). From the observed $k_{ClO_3^-}$ and k_{COD}, the k_2 / k_3 was calculated to be 1.1 mM^{-1} for H10, 0.60 mM^{-1} for H30, and 0.31 mM^{-1} for H50. Assuming that the k_3 is similar in each case, the reactivity between the RCS and COD (k_2) decreases as the $[Cl^-]_{ext.}$ increases. As shown in Table 3.3, the $E_a - iR$ values for H10 and H30 are sufficient to produce $Cl_2^-\cdot$, a stronger oxidant than free chlorine (Table 3.2). The $E_a - iR$ for H50 is close to the edge of the redox potential required for radical generation and lower than for H10 and H30 due to a higher solution resistance. Furthermore, $Cl_2^-\cdot$ is in equilibrium with Cl·, which has a redox potential higher than $Cl_2^-\cdot$.[5] Thus, under chlorine radicals generation, increasing [Cl^-] favors the formation of $Cl_2^-\cdot$ to Cl·, resulting in a net lower reactivity in terms of the rate of COD oxidation.

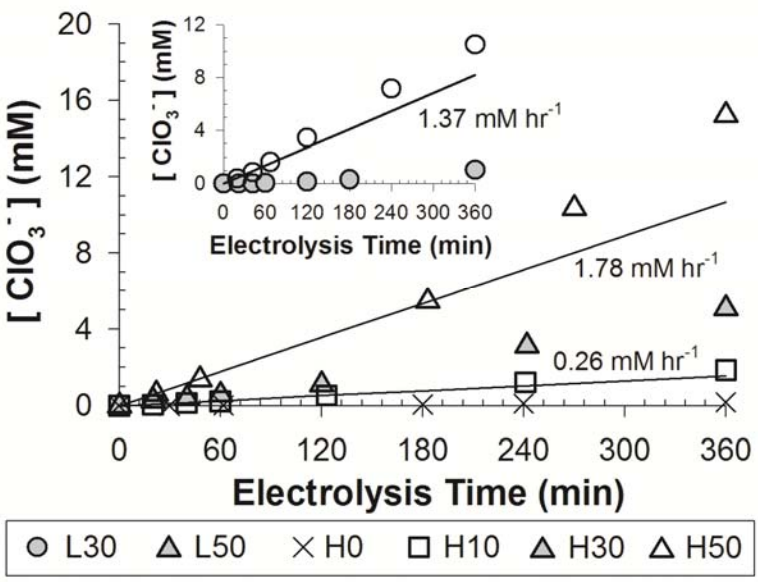

Figure 3.5. Time profiles of ClO_3^- concentration in electrolysis experiments using domestic wastewater samples under variable applied anodic potential (L: 2.2 V, H: 3.0 V NHE) and added Cl^- concentration (0, 10, 30, 50 mM). For H10, H30, and H50, regression lines for linearly increasing regions (initial 4 data points) are shown with corresponding zero-order rate constants.

3.3.4. Nitrogen Species. In the wastewater samples, the sum of $[NH_4^+]$ and $[NO_3^-]$ constituted more than 95% of [TN]. As shown in Figure 3.6a, $[NH_4^+]$ decreased to near zero within 3 h of electrolysis, except in the absence of added Cl^- (Figure 3.6a). The pseudo-first-order rate constants for NH_4^+ loss were higher than those for COD removal. A more facile oxidation of NH_4^+ than for various organic compounds (*i.e.*, COD) has also been reported for tannery wastewater[30] and landfill leachates.[28] The reaction rates of RCS generated at anode surfaces toward NH_4^+ and COD are often affected by mass transport.[31] Results show that NO_3^- increases with time but not in a normal stoichiometric relationship (Figure 3.6b). This is due to a substantial fraction of NH_4^+ that is converted to N_2. The sequential chlorination of NH_4^+ is known to produce the N_2 via breakpoint

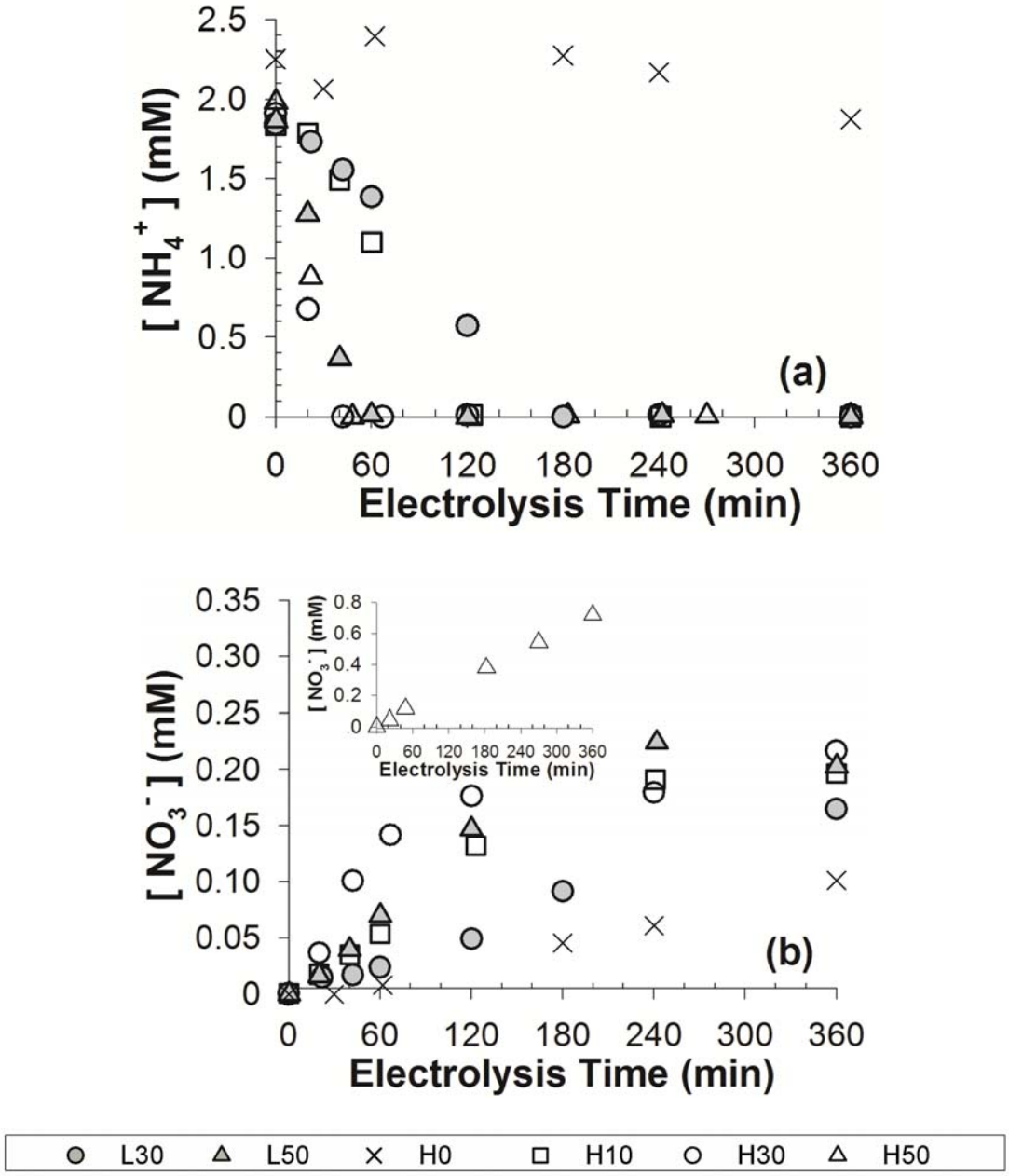

Figure 3.6. Time profiles of (a) NH_4^+ and (b) NO_3^- concentration under variable applied anodic potential (L: 2.2 V, H: 3.0 V NHE) and added Cl^- concentration (0, 10, 30, 50 mM) in electrolysis experiments using domestic wastewater samples.

chlorination.[17,28,32] For landfill leachates,[33] N_2 formation rate exceeded that of NO_3^-, especially as current densities or [Cl^-] increased.

3.3.5. CE and Energy Consumption for Anodic Reactions. The efficiency of electrochemical reactions is often expressed in terms of current efficiency, CE.[3,4] Figure 3.7 shows the general CE (eq 3.5) for the anodic reactions in the various wastewater electrolyses.

$$\text{Current Efficiency (CE) for Anodic Reaction } i\ (\%) = \frac{n_i \times F \times \left| C_i^{\,0} - C_i^{\,t} \right| \times V}{\int_0^t I dt} \times 100 \qquad (3.5)$$

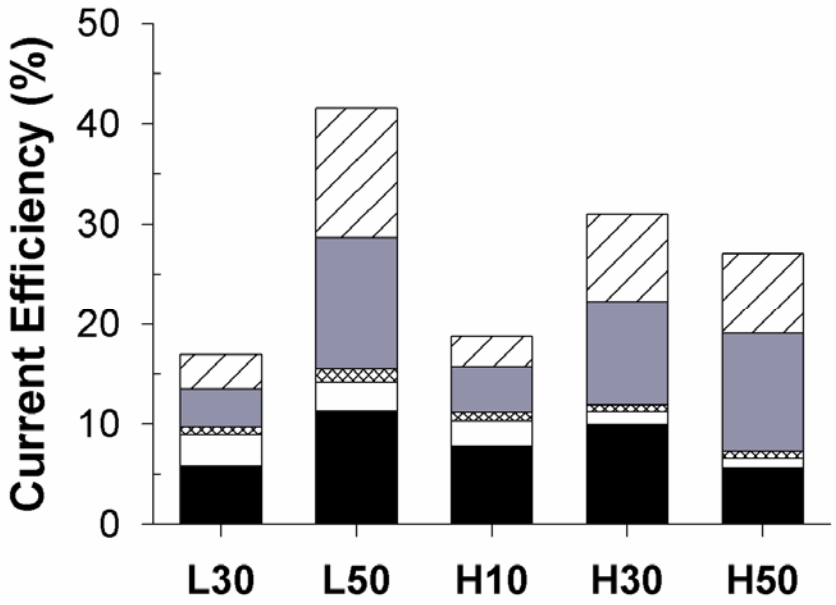

Figure 3.7. General current efficiencies for anodic reactions including COD oxidation (▬), formation of N_2 (▭), NO_3^- (▩), ClO_3^- (▬), and free chlorine (▨) under variable applied anodic potential (L: 2.2 V, H: 3.0 V NHE) and added Cl^- concentration (10, 30, 50 mM) in electrolysis experiments using domestic wastewater samples. Estimates are based on the time when COD decreases to below 30 mg L^{-1}.

where, C_i^0 and C_i^t are the concentration of species *i* (M) at the electrolysis time of zero and *t* (s), *V* is the volume of the electrolyte (0.06 L), *I* is the current (A), *F* is Faraday constant (96485.3 C mol^{-1}), and n_i is the number of electrons required to oxidize one mole of species *i*; 4 for oxidation of COD expressed in $molO_2\ L^{-1}$, 3 for NH_4^+ to N_2, 8 for NH_4^+ to NO_3^-, 6 for Cl^- to ClO_3^-, and 2 for Cl^- to Cl_2. The estimates shown in Figure 3.7 are based on the time when COD first declined to below 30 mg L^{-1}, a typical criteria for water reuse.[34]

The CE for COD oxidation has been known to decrease with the electrolysis time in case of direct oxidation limited by diffusion to the anode surface[29] or galvanostatic electrolysis due to a decrease in substrate concentration.[24] In our case, the differential concentrations of COD, NH_4^+, NO_3^-, and ClO_3^- are correlated with the specific passed charge (coulomb per unit volume); *i.e.*, consistent CE's with the electrolysis time. The decrease of the COD removal rate along with the [COD] was compensated by the decrease in *J*, which was proportional to $[Cl^-]$. The linear relation between the [COD] and $[Cl^-]$ also contributes to the apparent self-consistent current efficiencies.

At lower anodic potentials (L30 and L50), in which the heterogeneous RCS generation is limiting, the increase in $[Cl^-]_{ext.}$ significantly enhanced the CE. In contrast, at higher potentials, where homogeneous reactions between RCS and COD become important, the CE for COD removal was the highest in the wastewater sample H30. Oxidation of NH_4^+ to NO_3^- and N_2 were minor fractions (~ 10%) of the anodic charge transfer due to the small initial $[NH_4^+]$. The CE's for the observed residual chlorine were similar to those for ClO_3^- production and COD loss. The sum of the RCS mediated

reactions was below 40%. The loss in CE's can be attributed to O_2 evolution and RCS reduction at the cathode.

Table 3.4 summarizes the times required to reduce COD to be below 30 mg L^{-1} (t_{COD30}), as well as [COD], [NO_3^-], [ClO_3^-], [Cl_{DPD}], and corresponding specific energy consumption (SEC) for COD removal at t_{COD30}. The SEC was calculated as follows:

$$\text{Specific Energy Consumption (kWh kgCOD}^{-1}) = \frac{\int_0^t (E_a - E_C) \times I \, dt}{([COD]^0 - [COD]^t) \times V} \times 1000 \qquad (3.6)$$

where, $E_a - E_c$ and I are cell voltage (V) and current (A), $[COD]^0$ and $[COD]^t$ are COD concentration (mg L^{-1}) at the electrolysis time of zero and t (h), and V is electrolyte volume (0.06 L). For galvanostatic electrolyses, an increasing [Cl^-] decreases the SEC by decreasing the cell voltage.[13,25,27] Under potentiostatic conditions, however, the SEC

Table 3.4. Sampling time when COD below 30 mg L^{-1} was observed (t_{COD30}), concentration of COD, NO_3^-, ClO_3^- and total chlorine at t_{COD30}, and specific energy consumption (SEC) for unit COD removal at t_{COD30} under variable applied anodic potential (L: 2.2 V, H: 3.0 V NHE) and added Cl^- concentration (10, 30, 50 mM) in electrolysis experiments using domestic wastewater samples.

ID	L30	L50	H10	H30	H50
t_{COD30} (min)	> 360	240	360	120	180
[COD] (mg L^{-1})	93	13	11	19	28
[NO_3^-] (mM)	0.16	0.22	0.20	0.18	0.38
[ClO_3^-] (mM)	1.0	3.1	1.9	3.4	7.1
[Cl_{DPD}] (mM)	2.8	9.1	3.7	8.8	14.5
SEC (kWh $kgCOD^{-1}$)	232	96	209	176	320

value has been reported to increase with [Cl^-] or conductivity via an increase in J.[26] Under both electrolytic conditions, increasing the cell voltage or current density for a given electrolyte composition normally increases the SEC.[22] In this regard, H30 gave the best space-time yield and SEC for COD removal at the high E_a. However, an increase in cell voltage and J at E_a of 3.0 V NHE requires larger energy consumption compared to E_a of 2.2 V NHE. Thus, the minimal energy usage was obtained with $[Cl^-]_{ext.}$ of 50 mM at E_a of 2.2 V NHE, which corresponds to a cell voltage of about 4 V.

3.3.6. Hydrogen Production. The generation rate of total gaseous products, the H_2 volumetric fraction, and the H_2 molar flow rate increased with increasing current density (Table 3.5). The fraction of H_2 was ~ 40% in L30 and L50, and ~ 60% in higher E_a. Other gaseous products would include O_2, H_2O, N_2, and CO_2.[7] The CE and energy efficiency of H_2 generation were calculated as follows.

Table 3.5. Hydrogen evolution for a given duration (200 – 230 min) under variable applied anodic potential (L: 2.2 V, H: 3.0 V NHE) and added Cl^- concentration (10, 30, 50 mM) in electrolysis experiments using domestic wastewater samples; current density, flow rate of total gas products, volumetric fraction of hydrogen, molar flow rate of hydrogen, current efficiency, and energy efficiency for hydrogen generation.

ID	L30	L50	H10	H30	H50
Current Density (A m^{-2})	66.7	82.6	103	179	289
Total Gas Flow (mL min^{-1})	0.320	0.253	0.453	0.907	1.720
H_2 Fraction (%)	35.1	41.1	52.6	54.3	59.2
H_2 Generation Rate (μmol min^{-1})	5.02	4.64	10.7	22.0	45.4
Current Efficiency (%)	44.8	33.5	55.4	73.2	84.1
Energy Efficiency (%)	18.0	14.0	16.9	18.5	26.0

$$\text{Current Efficiency for } H_2 \text{ production (\%)} = \frac{2 \times F \times Q_{H_2} \times t}{\int I \, dt} \times 100 \quad (3.7)$$

$$\text{Energy Efficiency for } H_2 \text{ production (\%)} = \frac{3600 \times (78\ Wh\ mol^{-1}) \times Q_{H_2} \times t}{\int (E_a - E_c) \times I \, dt} \times 100 \quad (3.8)$$

where, $E_a - E_c$ and I are cell voltage (V) and current (A), Q_{H_2} is H_2 molar production rate (mol sec^{-1}), t is time for gas collection (sec), and F is Faraday constant (96485.3 C mol^{-1}). The CE for H_2 generation was below 50% at low E_a and then increased with increasing J up to 84% at higher E_a. The remaining fraction of electron transfer at the cathode can be attributed to the combined reduction of RCS and O_2.[5,8,35] In particular, a reduction of the RCS would reduce the current efficiency both for desired anodic and cathodic reactions. We previously estimated[7,8,21] the CE for hydrogen generation to be from 50% to 90% depending on cell voltage and, more importantly, the relative concentration of organic electron doners to chloride. An augmented presence of electron donors significantly increases the CE for H_2 generation via quenching the RCS. The energy efficiency for H_2 production was estimated to be from 14% to 26%. Higher energy efficiencies up to 46% have been reported under lower cell voltages (~ 3 V)[7] or under a photoelectrocatalytic operation of the BiO_x/TiO_2 anode.[10] H_2 generated as a primary by-product in WEC or PWEC can be used in either a proton exchange membrane (PEM) or solid-state fuel cell. Therefore, a moderate reduction in the SEC is expected when utilizing the produced H_2 as a back-up energy source for the PWEC.

3.3.7. Prototype (20 L) PV Powered Wastewater Electrolysis. If a PV panel DC output is connected directly to an electrolysis reactor, then the cell voltage and current will be

affected by the electrolyte conductivity, temperature, and solar intensity. The $E_a - E_c$ and J values are determined by the characteristic *I–V* curve of a PV panel at a given incident solar radiation, the panel temperature, and the resistance of the electrolysis cell.[36] We had previously reported[8] a solar energy conversion efficiency below 2% when using a PV panel that was directly connected to an electrolysis cell containing industrial wastewater. In order to increase the solar energy conversion efficiency, we employed a rechargeable lead acid battery regulated by a charge controller to generate an electrical energy output of ~ 84 W (12 V × 7 A), while maintaining a constant cell voltage.

For the solar roof-top experiment, 50 mM of NaCl was added to a domestic wastewater sample to maintain a cell voltage of 3.9 V on average, which was close to the operating condition of the least energy consumption in the benchtop experiments (L50). The current was 16.7 A, corresponding to a current density of 20.9 A m^{-2}. The larger-scale prototype reactor, with the PV panel as a power source, had a similar rate of COD removal with L50; for the initial [COD] of 180 mg L^{-1} was reduced to 21 mg L^{-1} after 4 h of reaction. We also confirmed that *in-situ* generation of free chlorine[18,37] leads to the disinfection of the total coliform and fecal coliform bacterial load (Figure 3.8). The initial bacterial concentration was 7.8×10^5 CFU 100 mL^{-1} for total coliforms and 8.0×10^4 CFU 100 mL^{-1} for fecal coliforms. A majority of the coliforms (50 – 80 %) were eliminated within 30 min. Complete disinfection was observed after 3 h of electrolysis along with a significant decrease in [COD].

The effluents from the scaled-up PWEC would be of sufficient water quality to be reclaimed for nonpotable purposes.[34] On the other hand, further anodic oxidation of the

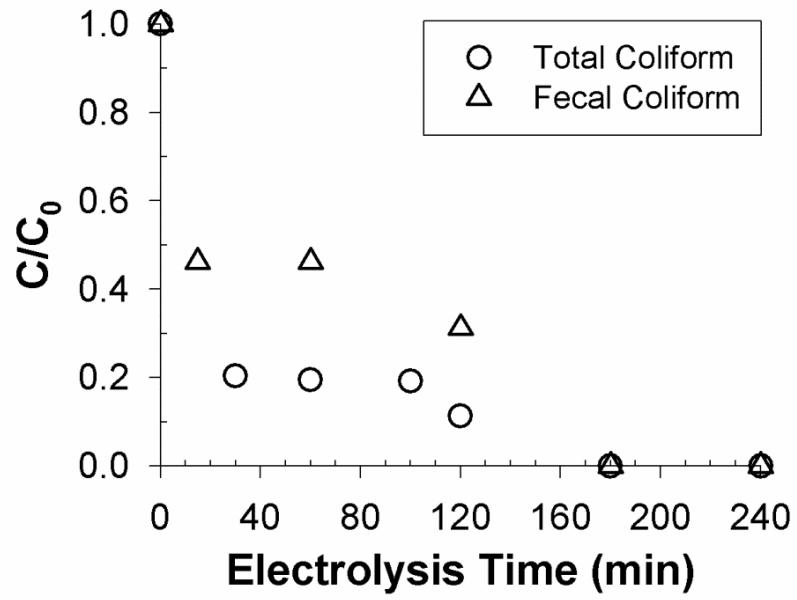

Figure 3.8. Time profiles for normalized concentration of total and fecal coliform during photovoltaic-powered wastewater electrolysis cell (PWEC, 20 L) experiment using domestic wastewater (cell voltage: 4.9 V, added Cl^- concentration: 50 mM).

RCS leads to the production of ClO_3^-, which has potential environmental health risks.[19] In the benchtop WEC (L50), the $[ClO_3^-]$ after 4 h of electrolysis was 3.0 mM. At this concentration, the reuse of the treated water would be restricted to a closed-loop recycled water system to be used for toilet flushing and for wash water. A mass balance analysis for chlorine species indicates that the sum of Cl^-, Cl_{DPD}, and ClO_3^- concentration deviate the initial chloride concentration by no more than 0.1 mM. Therefore, chlorinated byproducts other than ClO_3^- would be in a trace-level concentration.

Well-designed PWEC could be utilized within self-contained toilet facilities to provide suitable decentralized wastewater treatment systems. The energy consumption per unit volume of wastewater was estimated to be 13 Wh L^{-1} for the 20 L PWEC with a retention time of 4 h. We estimate that, for a community toilet with 30 users in a remote

rural area, the wastewater flow rate would be approximated at 120 L day^{-1}, assuming a low water usage (1.0 L d^{-1} $capita^{-1}$ for urine with 3.0 L d^{-1} $capita^{-1}$ for flushing).[12,38] With an average energy output from solar irradiation of 56 W m^{-2} over 8 h per day, the daily available solar energy is calculated to be 448 Wh day^{-1} m^{-2}. At this energy level, the total exposed surface area of polycrystalline PV panels that would be required for continuous operation of the PWEC would be virtually 3.5 m^2.

3.4. SUPPORTING INFORMATION

3.4.1. Electrochemical Methods. Before all electrochemical experiments, the electrodes were rinsed with acetone and a large amount of Milli-Q water. The electrode module was allowed to equilibrate with the electrolyte solution in an open circuit for 30 min while monitoring the open circuit potential of anode and cathode. As a routine procedure, the pH, conductivity and the ohmic resistance between anode and reference electrode (R) were measured before and after the electrochemical experiments. The pH and conductivity of the samples were monitored using a pH meter (Mettler Toledo, USA) and a portable conductivity meter (VWR International, USA). As shown in Figure 3.9, the conductivity increased while R decreased monotonically as the added chloride concentration increased. The anodic potentials were converted into NHE scale using E_a (NHE) = E_a (Ag/AgCl) + 0.197 V.

3.4.2. Prototype PV-powered Wastewater Electrolysis. The solar panel had a peak power output of 180 W with an open circuit voltage of 25.9 V, a short circuit current of 6.95 A, and an active surface area of 1.50 m^2 (0.95 m × 1.57 m), respectively. Incident solar irradiation was measured using a pyranometer (Apogee, USA) which ranged from

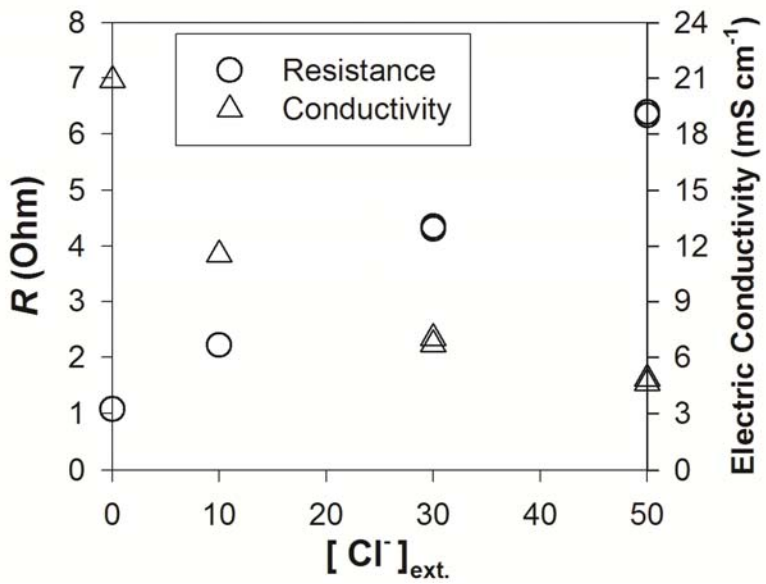

Figure 3.9. Ohmic resistance between anode and reference electrode (*R*) and electric conductivity of bulk electrolyte as functions of added Cl^- concentration ($[Cl^-]_{ext.}$) in bench-top electrolysis experiments using domestic wastewater samples.

1,000 W m^{-2} (noontime) to 600 W m^{-2} depending on the solar zenith angle. A 12 V rechargeable battery that was regulated using a charge controller was used to store excess solar energy. The voltage of the battery was controlled in order to adjust the cell voltage to be 3.9 V. The main oxidants at this cell voltage should be free chlorine species (HOCl considering the bulk pH ~ 6) since the actual anodic potential was not high enough to generate chlorine radicals. In scaling-up the WEC, an inevitable increase of ohmic voltage loss caused a reduction in current density when compared to the bench-top experiment. In these circumstances, an adjustment of electrode configuration was required to keep the free chlorine generation rate. In particular, the electrolyte volume-to-electrode surface area ratio was adjusted to 2.5 cm (20,000 cm^3 / 8,000 cm^2) while the

distance among electrodes was reduced to 2 mm, to achieve a current per unit electrolyte volume comparable with laboratory WEC (L50).

3.4.3. Analysis of Total and Fecal Coliform Concentration. In our sampling procedure, a 0.45 μm membrane filter was used to collect a microbial sample. The filter membrane is then placed on an 'mEndo' agar LES media for total coliform and an 'mFC' agar for fecal coliform for selective growth. The media plates were incubated at 35 °C for total coliform and 44.5 °C for fecal coliform for 24 h in order to promote discrete colonies. The concentration of total and fecal coliform bacteria in the wastewater was estimated in terms of CFU 100 mL^{-1} (Colony Forming Units per 100 mL).

3.5. REFERENCES

(1) *Sick Water? The central role of wastewater management in sustainable development. A rapid response assessment*; United Nations Environment Programme, UN-HABITAT, GRID-Arendal: Birkeland, 2010.; www.grida.no/publications/rr/sickwater/.

(2) Comninellis, C. Electrocatalysis in the electrochemical conversion/combustion of organic pollutants for waste-water treatment. *Electrochimica Acta* **1994,** *39* (11-12), 1857-1862.

(3) Martinez-Huitle, C. A.; Ferro, S. Electrochemical oxidation of organic pollutants for the wastewater treatment: direct and indirect processes. *Chemical Society Reviews* **2006,** *35* (12), 1324-1340.

(4) Panizza, M.; Cerisola, G. Direct And mediated anodic oxidation of organic pollutants. *Chemical Reviews* **2009,** *109* (12), 6541-6569.

(5) Park, H.; Vecitis, C. D.; Hoffmann, M. R. Electrochemical water splitting coupled with organic compound oxidation: The role of active chlorine species. *Journal of Physical Chemistry C* **2009,** *113* (18), 7935-7945.

(6) Cho, K.; Kwon, D.; Hoffmann, M. R. Electrochemical treatment of human waste coupled with molecular hydrogen production. *RSC Advances* **2014**, *4*, 4596-4608.

(7) Park, H.; Vecitis, C. D.; Hoffmann, M. R. Solar-powered electrochemical oxidation of organic compounds coupled with the cathodic production of molecular hydrogen. *Journal of Physical Chemistry A* **2008,** *112* (33), 7616-7626.

(8) Choi, J.; Qu, Y.; Hoffmann, M. R. SnO_2, IrO_2, Ta_2O_5, Bi_2O_3, and TiO_2 nanoparticle anodes: Electrochemical oxidation coupled with the cathodic reduction of water to yield molecular H_2. *Journal of Nanoparticle Research* **2012,** *14* (8).

(9) Weres, O. Electrode with surface comprising oxides of titanium and bismuth and water purification process using this electrode. U.S. Patent 7,494,583 B2, Feb. 24, 2009.

(10) Park, H.; Bak, A.; Ahn, Y. Y.; Choi, J.; Hoffmannn, M. R. Photoelectrochemical performance of multi-layered BiO_x-TiO_2/Ti electrodes for degradation of phenol and production of molecular hydrogen in water. *Journal of Hazardous Materials* **2012,** *211*, 47-54.

(11) Bard, A. J.; Faulkner, L. R., *Electrochemical methods : fundamentals and applications*. 2nd ed.; Wiley: New York, 2001.

(12) Siegrist, R.; Witt, M.; Boyle, W. C. Characteristics of rural household wastewater. *Journal of the Environmental Engineering Division-Asce* **1976,** *102* (3), 533-548.

(13) Malpass, G. R. P.; Miwa, D. W.; Mortari, D. A.; Machado, S. A. S.; Motheo, A. J. Decolorisation of real textile waste using electrochemical techniques: Effect of the chloride concentration. *Water Research* **2007,** *41* (13), 2969-2977.

(14) Shuk, P.; Wiemhofer, H. D.; Guth, U.; Gopel, W.; Greenblatt, M. Oxide ion conducting solid electrolytes based on Bi_2O_3. *Solid State Ionics* **1996,** *89* (3-4), 179-196.

(15) Trasatti, S. Progress in the understanding of the mechanism of chlorine evolution at oxide electrodes. *Electrochimica Acta* **1987,** *32* (3), 369-382.

(16) Santana, M. H. P.; De Faria, L. A. Oxygen and chlorine evolution on RuO_2+TiO_2+CeO_2+Nb_2O_5 mixed oxide electrodes. *Electrochimica Acta* **2006,** *51* (17), 3578-3585.

(17) Deborde, M.; von Gunten, U. Reactions of chlorine with inorganic and organic compounds during water treatment - Kinetics and mechanisms: A critical review. *Water Research* **2008,** *42* (1-2), 13-51.

(18) Czarnetzki, L. R.; Janssen, L. J. J. Formation of hypochlorite, chlorate and oxygen during NaCl electrolysis from alkaline-solutions at an RuO_2/TiO_2 anode. *Journal of Applied Electrochemistry* **1992,** *22* (4), 315-324.

(19) Jung, Y. J.; Baek, K. W.; Oh, B. S.; Kang, J. W. An investigation of the formation of chlorate and perchlorate during electrolysis using Pt/Ti electrodes: The effects of pH and reactive oxygen species and the results of kinetic studies. *Water Research* **2010,** *44* (18), 5345-5355.

(20) Scialdone, O.; Randazzo, S.; Galia, A.; Silvestri, G. Electrochemical oxidation of organics in water: Role of operative parameters in the absence and in the presence of NaCl. *Water Research* **2009,** *43* (8), 2260-2272.

(21) Park, H.; Choo, K.; Park, H.; Choi, J.; Hoffmann, M. R. Electrochemical oxidation and microfiltration of municipal wastewater with simultaneous hydrogen production: Influence of organic and particulate matter. *Chemical Engineering Journal* **2013,** *215-216* (15), 802-810.

(22) Fernandes, A.; Pacheco, M. J.; Ciriaco, L.; Lopes, A. Anodic oxidation of a biologically treated leachate on a boron-doped diamond anode. *Journal of Hazardous Materials* **2012,** *199*, 82-87.

(23) Miwa, D. W.; Malpass, G. R. P.; Machado, S. A. S.; Motheo, A. J. Electrochemical degradation of carbaryl on oxide electrodes. *Water Research* **2006,** *40* (17), 3281-3289.

(24) Panizza, M.; Cerisola, G. Olive mill wastewater treatment by anodic oxidation with parallel plate electrodes. *Water Research* **2006,** *40* (6), 1179-1184.

(25) Malpass, G. R. P.; Miwa, D. W.; Machado, S. A. S.; Olivi, P.; Motheo, A. J. Oxidation of the pesticide atrazine at DSA (R) electrodes. *Journal of Hazardous Materials* **2006,** *137* (1), 565-572.

(26) Gotsi, M.; Kalogerakis, N.; Psillakis, E.; Samaras, P.; Mantzavinos, D. Electrochemical oxidation of olive oil mill wastewaters. *Water Research* **2005,** *39* (17), 4177-4187.

(27) Costa, C. R.; Olivi, P. Effect of chloride concentration on the electrochemical treatment of a synthetic tannery wastewater. *Electrochimica Acta* **2009,** *54* (7), 2046-2052.

(28) Chiang, L. C.; Chang, J. E.; Wen, T. C. Indirect oxidation effect in electrochemical oxidation treatment of landfill leachate. *Water Research* **1995,** *29* (2), 671-678.

(29) Panizza, M.; Delucchi, M.; Cerisola, G. Electrochemical degradation of anionic surfactants. *Journal of Applied Electrochemistry* **2005,** *35* (4), 357-361.

(30) Szpyrkowicz, L.; Kaul, S. N.; Neti, R. N.; Satyanarayan, S. Influence of anode material on electrochemical oxidation for the treatment of tannery wastewater. *Water Research* **2005,** *39* (8), 1601-1613.

(31) Szpyrkowicz, L.; Kelsall, G. H.; Kaul, S. N.; De Favei, M. Performance of electrochemical reactor for treatment of tannery wastewaters. *Chemical Engineering Science* **2001,** *56* (4), 1579-1586.

(32) Kapalka, A.; Katsaounis, A.; Michels, N. L.; Leonidova, A.; Souentie, S.; Comninellis, C.; Udert, K. M. Ammonia oxidation to nitrogen mediated by electrogenerated active chlorine on Ti/PtO_x-IrO_2. *Electrochemistry Communications* **2010,** *12* (9), 1203-1205.

(33) Peez, G.; Saiz, J.; Ibanez, R.; Urtiaga, A. M.; Ortiz, I. Assessment of the formation of inorganic oxidation by-products during the electrocatalytic treatment of ammonium from landfill leachates. *Water Research* **2012,** *46* (8), 2579-2590.

(34) *Guidelines for water reuse*; EPA/600/R-12/618; United States Environmental Protection Agency: Washington, D.C., 2012.; nepis.epa.gov/Adobe/PDF/P100FS7K.pdf.

(35) Kim, J.; Choi, W. J. K.; Choi, J.; Hoffmann, M. R.; Park, H. Electrolysis of urea and urine for solar hydrogen. *Catalysis Today* **2013,** *199*, 2-7.

(36) Valero, D.; Ortiz, J. M.; Exposito, E.; Montiel, V.; Aldaz, A. Electrochemical wastewater treatment directly powered by photovoltaic panels: Electrooxidation of a

dye-containing wastewater. *Environmental Science & Technology* **2010,** *44* (13), 5182-5187.

(37) Bergmann, M. E. H.; Rollin, J.; Iourtchouk, T. The occurrence of perchlorate during drinking water electrolysis using BDD anodes. *Electrochim. Acta* **2009,** *54* (7), 2102-2107.

(38) *Onsite wastewater treatment systems manual*; EPA/625/R-00/008; United States Environmental Protection Agency: Washington, D.C., 2002.; nepis.epa.gov/Adobe/ PDF/P100FS7K.pdf .

Chapter 4

ELECTROCHEMICAL TREATMENT OF HUMAN WASTE COUPLED WITH MOLECULAR HYDROGEN PRODUCTION

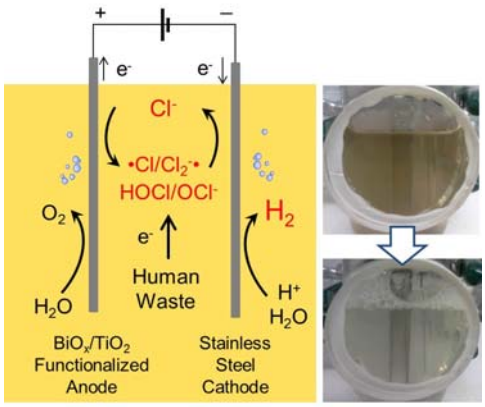

Sections reprinted with permission from Kangwoo Cho, Daejung Kwon, and Michael R. Hoffmann *RSC Advances* **2014**, *4*, 4596-4608.

ABSTRACT

We have developed a wastewater treatment system that incorporates an electrolysis cell for on-site wastewater treatment coupled with molecular hydrogen production for use in a hydrogen fuel cell. Herein, we report on the efficacy of a laboratory-scale wastewater electrolysis cell (WEC) using real human waste for the first time with a semiconductor electrode utilizing a mixed particle coating of bismuth oxide doped titanium dioxide (BiO_x/TiO_2). A comprehensive environmental analysis has been coupled together with a robust kinetic model under the chemical reaction limited regime to investigate the role of various redox reactions mediated by chloride present in human waste. The oxidative elimination of the *chemical oxygen demand* (COD) and ammonium ion can be modelled using empirical, pseudo-first-order rate constants and current efficiencies (CE). In combination with an anaerobic pre-treatment step, human waste containing high-levels of COD, protein, and color are eliminated within 6 h of batch treatment in the WEC. The reactor effluent has residual inorganic total nitrogen (TN) concentration of ~ 40 mM. The CE and specific energy consumption were 8.5% and 200 kWh $kgCOD^{-1}$ for the COD removal, 11% and 260 for kWh $kgTN^{-1}$ for the TN conversion. The CE and energy efficiencies (EE) for hydrogen production were calculated to be 90% and 25%, respectively.

4.1. INTRODUCTION

There has been an increasing awareness of an emerging crisis with respect to water resources due to global population growth and climate change. Close to 80% of the world's population is threatened by water scarcity, due primarily to a deficit of safe drinking water and water for personal sanitation.[1] It is estimated that 2.7 billion people lack access to sufficient water for human sanitation (*i.e.*, for personal hygiene) and proper waste disposal.[2] The direct discharge of untreated human waste and open defecation are major sources of waterborne diseases. Furthermore, the biochemical oxygen demand (BOD) generated by the discharge of human waste into receiving waters is becoming a threat to biodiversity. As a consequence, research has been focused on approaches to enhance the water safety and productivity for non-consumptive uses by technological improvement in wastewater treatment and reuse practices.[2,3] However, a lack of infrastructures in the developing world and highly interrelated water-energy nexus[3] require the water treatment and reuse practices to be on-site, energy sustainable, and economical with a minimal use of hydraulic retention time (HRT) and material costs.

In order to address some of these problems, we are exploring the use of electrochemical reactors or wastewater electrolysis cells (WEC) that have been designed to provide on-site wastewater treatment for water recycling and reuse coupled with energy storage. Electrochemical water oxidation to oxygen on metal oxides anodes is known to initiate by formation of surficial hydroxyl radicals and/or by direct electron transfer to surface-bound holes,[4-6] which can be used for the ‘direct’ oxidation of environmental contaminants. Wastewater with a sufficient level of electrical conductivity

(σ), such as dye wastewater and landfill leachate, has been investigated extensively for the electrochemical removal of pollutants.[4,6] The near ubiquitous presence of chloride (Cl^-) in the high-salinity wastewater often leads to the homogeneous 'indirect' oxidation via production of reactive chlorine species (RCS) including free chlorine (Cl_2, HOCl, ClO^-)[4,6] and chlorine radicals ($Cl\cdot$, $Cl_2^-\cdot$).[7] The existence of chloride has been frequently reported to reduce specific energy consumption (SEC) for electrochemical oxidation of chemical pollutants by increasing σ and substrate degradation rates at a given current (or potential).[8-14]

Energy conversion and storage are possible due to electron transfer to water or proton to produce hydrogen at the cathodes. This can lead to a much lower carbon footprint when compared to the steam reformation of methane to produce hydrogen.[7,15,16] Under a sufficient solar irradiation, the WEC can be powered by an appropriate size of photovoltaic (PV) panels,[7,15,17-19] to allow for a sustainable and traditional-infrastructure-free approach to human waste treatment coupled with the generation of an energy-rich by-product (*e.g.*, H_2). Therefore, a PV-powered WEC (PWEC) has the potential to address the global needs for energy, water, and human health by using green chemistry without additional chemical reagents (*e.g.*, O_3, H_2O_2, $S_2O_8^{2-}$, etc.) to achieve a high-degree of BOD reduction.

It is possible to achieve energy efficient hydrogen production[20] coupled with chemical contaminant oxidation[21,22] when utilizing electrochemically active anodes with high oxygen evolution reaction (OER) rates. Intrinsic cost-effectiveness and mechanical/chemical inertness are also important considerations for the proper design of

electrodes.[5,20] Electrodes with high OER overpotentials (η), based on SnO_2, PbO_2, and BDD (Boron Doped Diamond), have been used exclusively for the direct electrochemical oxidation.[4,6,23] In spite of superior current efficiencies for organic compound oxidation, these electrodes would not be suitable for energy conversion due to the lack of electrocatalytic activity and large energy losses.[21,22] Facile O_2/Cl_2 evolution at active novel Pt group metal oxides (RuO_2 and IrO_2) and combined usage with inert metal oxides (TiO_2, Ta_2O_5, and SnO_2) to increase corrosion resistance allowed their applications for water splitting, chlor-alkali production, and wastewater electrooxidation.[5,20,24,25] However, the high material cost of low-abundance metals (*i.e.*, Ru and Ir) is a major limitation for their commercial application.[20] The electrocatalytic OER activity has long been ascribed to a reversible redox transition within the potential energy window of water splitting.[5,20] In this regard, the pseudo-capacitance and dielectric permittivity of Bi_2O_3 provide a less costly approach for OER systems and for use in Faradaic supercapacitors.[26] Accelerated ion conductivity due to the intrinsic (disordered) oxygen vacancies and high polarizability due to the presence of $6s^2$ lone pair in Bi enables Bi_2O_3 to be applied as a solid oxide fuel cell electrolyte.[27] Based on the promising characteristics of this earth abundant metal oxide, our previous reports[7,15,16,18,19] have demonstrated the feasibility of Bi-doped TiO_2 (BiO_x/TiO_2) electrodes for use in the WEC.

Herein, we report on the efficacy of the WEC equipped with the BiO_x/TiO_2 anode as a novel, dual-functioning approach for treatment and/or reuse of liquid human waste coupled with the simultaneous production of molecular hydrogen. Human urine is often a source of chloride present in domestic wastewater, which in turn can be oxidized to RCS, resulting in further organic compound oxidation and disinfection. The complex reaction

network involved in chloride mediated indirect oxidation[4,6] and the large number of operational variables that include current, applied cell voltage, pre-treatment, influent dilution, fluid-flow, and mixing[28] require reliable kinetic models in order to explore the role of each operational parameter. Consistent with the electrocatalytic behavior of our BiO_x/TiO_2 composite electrodes, a simple kinetic model is derived based on the measured rate constants for pollutant degradation, current efficiency, and specific energy consumption.

4. 2. EXPERMIENTAL SECTION

4.2.1. BiO_x/TiO_2 Electrode Preparation. The multi-layered semiconductor electrodes were prepared by sequential deposition of mixed metal oxides[29] as follows: (i) an anti-passivation layer of IrO_2/Ta_2O_5 with a molar ratio of 73:27 (Ir:Ta), (ii) a sealing coat of SnO_2/Bi_2O_3 at Sn:Bi of 9:1, (iii) a slurry deposition of bismuth oxide doped TiO_2 (BiO_x/TiO_2) nanoparticles with Bi:Ti of 1:24, and (iv) BiO_x/TiO_2 thin film (over-coat) deposition at a molar ratio of 1:2 (Bi:Ti). Each thermal decomposition procedure requires a specific precursor composition, heat treatment, and repetition as described in the Supporting Information. In a recent report, we showed that the electrodes as prepared are dominated by the elemental composition of Ti, Bi, and O in electrochemically active outermost surface;[18] thus we will refer to our composite anodes as BiO_x/TiO_2 electrode. The anti-passivation layer together with the sealing coat is known to enhance the robustness and electric conductivity.[29]

4.2.2. Electrochemical Setup. The electrode modules used in this study consisted of a BiO_x/TiO_2 anode, a stainless steel (SS, Hastelloy C-22) cathode, and an

Ag/AgCl/Saturated KCl reference electrode (BaSi Inc., USA). The effective area of the anode and cathode was 5.4 cm^2 (2.7 cm × 2 cm). The distance between anode and cathode was 5 mm, while the reference electrode was located as close as possible to the anode. Hereafter, the electrochemical potentials are always expressed in terms of the normal hydrogen electrode (NHE). The electrochemical cells were powered by a potentiostat (SP-50, Bio-Logic, France) in which the applied anodic potential (E_a) was adjusted with continuous monitoring of the response current (i) and cathodic potential (E_c).

4.2.3. Electrode Characterization. The cyclic voltammetry (CV) data were collected using either a 50 mM NaCl or a 50 mM $NaClO_4$ electrolyte solution under quiescent conditions for three cycles consecutively without open-circuit resting. The scan rate and scan range were fixed at 5 mV sec^{-1} and 0 – 3 V, respectively. The chrono-amperometric data were collected in stirred solutions with 10, 30, and 50 mM NaCl, where the E_a was varied from 1.5 to 3.5 V in 0.5 V increments. The resulting data were stored for 10 min at each E_a while resting the system in an open circuit for 5 min before adjustment of each potential increment. The CV and chrono-amperometric experiments were performed in a single compartment cell with working volume of 275 mL. In order to assess the direct oxidation efficacy of the BiO_x/TiO_2 electrode, a bulk potentiostatic electrolysis (E_a: 3 V) was performed in 47.5 mL KH_2PO_4 solution (5.3 mM), whose small fraction (2 mL) was sequentially replaced with 10 mM NaCOOH solution in 10 min intervals without a change in σ. The variations in I and $[HCO_2^-]$ were monitored as functions of electrolysis time.

4.2.4. Wastewater Sample Preparation. Table 4.1 shows the average composition of urine collected from an Asian male (Age: 30) and domestic wastewater (DWW). The DWW was obtained at San Jose Creek Wastewater Treatment facility (tertiary treatment) operated by the Sanitation Districts of Los Angeles County (USA). Samples were collected after a primary settling tank and stored in 4 ºC before usage.

To simulate septic tank effluents (STEs), the urine was mixed with the DWW with a volumetric ratio of 1:3 and anaerobically incubated at 35 °C for 2 days (conventional HRT in septic tanks[30]). Under these conditions, the high-molecular-weight organic compounds in urine can be biodegraded into lower molecular weight fragments by the microorganisms present in wastewater. Pre-treated urine was further diluted with the DWW with the mixing ratio of 1:9 (STE1), 1:4 (STE2), and 1:1 (STE3), which produced

Table 4.1. Composition of the as-received domestic wastewater (DWW), urine, and model septic tank effluent (STE 1-4, see Supporting Information for details).

Constituent	DWW	Urine	STE1	STE2	STE3	STE4
pH	7.1	6.6	8.9	9.0	9.1	9.0
Conductivity (mS cm^{-1})	1.1	24	2.3	3.5	7.0	8.8
COD (mg L^{-1})	180	5300	310	480	900	460
TN (mM N)	2.6	410	13	25	61	66
Urea (mM)	< 0.01	159	2.4	1.1	5.8	7.4
NH_4^+ (mM)	1.9	21	12	24	38	44
NO_3^- (mM)	< 0.01	1.1	0.01	0.10	0.01	0.10
Cl^- (mM)	3.9	180	6.7	10	21	33
Protein (mg BSA L^{-1})	75	2300	160	250	520	280
Carbohydrate (mg glucose L^{-1})	35	530	16	39	63	23
Organic Acids (mM)	< 0.01	6.9	0.02	1.6	3.1	0.09

variable concentrations of mixed organic waste and chloride, as shown in Table 4.1. Since the microbial concentration in DWW should be much smaller than in a septic tank, digested urine after 7 days of incubation was also tested without further dilution (STE4).

4.2.5. WEC Experiments. The WEC setup consists of the electrode module in a single compartment electrolysis cell equipped with a side-branch sampling port and a gas outlet port on top. Initial working electrolyte and corresponding headspace volumes in the reactor were 55 mL and 20 mL, respectively. Potentiostatic electrolyses (E_a: 3 V) were performed in 30 and 50 mM NaCl solutions for 3 h to investigate the chloride oxidation kinetics in the absence of organic matter. The WEC experiments using urine (with and without dilution) and STEs proceeded for 6 h, again with constant E_a (3 V). Small aliquots of the electrolyte were collected for analyses without changing the working electrode surface area. During the middle (80 – 110 min) and the end phase (300 – 330 min) of the electrolyses, the sampling port was sealed with a rubber stopper for 30 min to introduce the headspace gas into a graded burette. The average total volumetric flow rate of gaseous products (Q) was monitored and the molar flow rate of hydrogen (F_{H2}) was scaled based on the volumetric fraction of hydrogen (X_{H2}), which was determined by a GC/TCD (Gas Chromatography with Thermal Conductivity Detector).

4.2.6. Chemical Analyses. The pH and conductivity were monitored using a Mettler Toledo EL20 pH meter and VWR portable conductivity meter. In order to determine the chemical oxygen demand (COD), samples were digested in a low range dichromate digestion solution (3 – 150 mg L^{-1}) in a COD reactor (DRB-200, Hach, USA) and quantified based on the absorbance at 420 nm. The total nitrogen (TN) concentration was

measured by the absorbance at 420 nm after treatment using a TN reagent set. Anions (Cl^-, ClO_3^-, NO_2^-, NO_3^-, HCO_2^-, $C_2O_4^{2-}$, $C_2H_3O_2^-$) and cations (NH_4^+, Na^+, Ca^{2+}, Mg^{2+}) were simultaneously determined by ion chromatography (DX-500, Dionex, USA) using an anion-exchange column Ionpac AS 19 and a cation-exchange column Ionpac CS 16. The protein and carbohydrate concentrations were measured using the Lowry method[31] and the phenol/sulfuric acid method.[32] The total chlorine (Cl_{DPD}) was measured using the DPD (N,N-diethyl-p-phenylenediamine) method at a wavelength of 530 nm. The concentration of urea was quantified based on the product ammonium concentration after hydrolysis with jack-bean urease. Absorbance measurements were made using an Agilent 8453 UV-VIS spectrophotometer.

4.3. RESULTS AND DISCUSSION

4.3.1. Voltammetric Characteristics of the WEC. The space-time extent of pollutant oxidation is generally expected to increase with the applied potential (or current) when the effects of the current density (J) on a desired current efficiency are not substantial.[28,33] However, concomitant augmentation of the solution resistance (iR) would be significant[34] in the WEC since the σ of electrolyte is much lower than in an industrial electrolyzer or chlor-alkali cell. Therefore, dealing with the WEC for energy conversion purposes, it is essential to investigate the variation of iR-compensated anodic potential ($E_a - iR$), J, and cell voltage ($E_a - E_c$) as a function of the E_a. As shown in Figure 4.1a, the iR sharply increases as the E_a increases due to the exponential dependence of i on the $E_a - iR$. The increase of $E_a - iR$ was marginal at an E_a above 3 V where additional power consumption should not contribute to the rate of electron transfer. Therefore, subsequent WEC

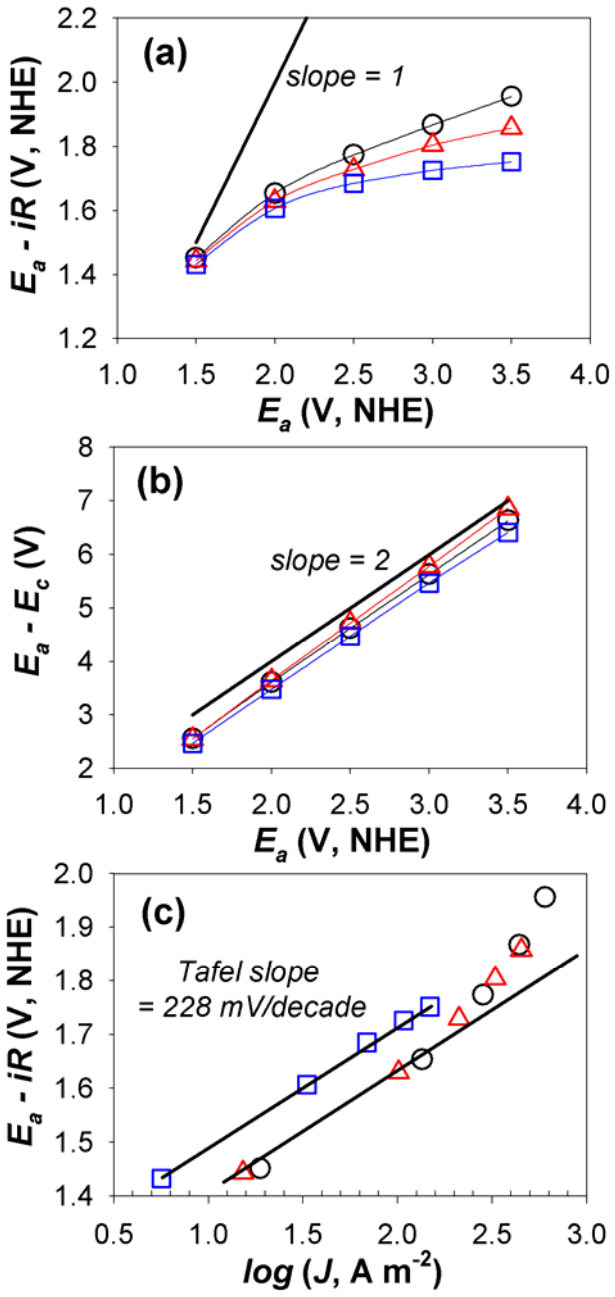

Figure 4.1. Dependence of (a) *iR* compensated anodic potential (E_a – iR) on applied anodic potential (E_a), (b) cell potential (E_a – E_c) on E_a, and (c) logarithmic current density (J) on the E_a – iR during chronoamperometric experiment in a single compartment electrolysis cell with 10 mM (square, R: 21.9 Ω), 30 mM (triangle, R: 6.8 Ω), and 50 mM (circle, R: 4.8 Ω) NaCl solution (275 mL).

experiments were carried out under potentiostatic conditions with the E_a of 3 V. The energy loss at high applied potentials should be emphasized considering that the $E_a - E_c$ is the actual determinant of the energy consumption; in this study, an equivalent magnitude of E_c was required to manipulate the E_a (Figure 4.1b).[33] This observation points out a potential problem, especially in dilute solution, with inferring that various reactive oxidants are present based on the cell voltage. For example, in 10 mM NaCl solution, the value of $E_a - iR$ at an $E_a - E_c$ of 6.41 V was only 1.75 V (27%), smaller than the thermodynamic potential required to form H_2O_2, O_3, as well as ·OH, Cl·, and Cl_2^{-}·. The reactive intermediates such as hydroxyl and chlorine radicals should be surface-bound to play a role without an $E_a - iR$ exceeding their redox potentials (E).

4.3.2. Electrochemistry of the BiO_x/TiO_2 Anode in Dilute Chloride Solutions. The BiO_x/TiO_2 has been used as a visible-light photocatalyst due to the characteristics of Bi_2O_3, including high refractive index and photoconductivity coupled with a relatively small band gap (~ 2.8 eV).[35] We also show that the BiO_x/TiO_2 anode is an excellent electrochemical catalyst for generation of oxygen and RCS. In Figure 4.2, we illustrate the cyclic voltammetry of the BiO_x/TiO_2 in 50 mM NaCl and 50 mM $NaClO_4$ solutions. The onset potential of the anodic wave was observed near 1.16 V (NHE) in both electrolytes; this corresponds to an OER η of 0.32 V. The OER η value of the BiO_x/TiO_2 is low compared with those of IrO_2 and RuO_2 based electrodes.[8,11,36] Since the OER η value is closely related to the enthalpy of oxide transition,[20] the facile OER activity of the BiO_x/TiO_2 anode can be attributed to the oxide ion conducting BiO_x rather than the electrochemically resistant TiO_2. According to Comninellis[23], the OER on metal oxides electrodes functions according to the following set of reactions:

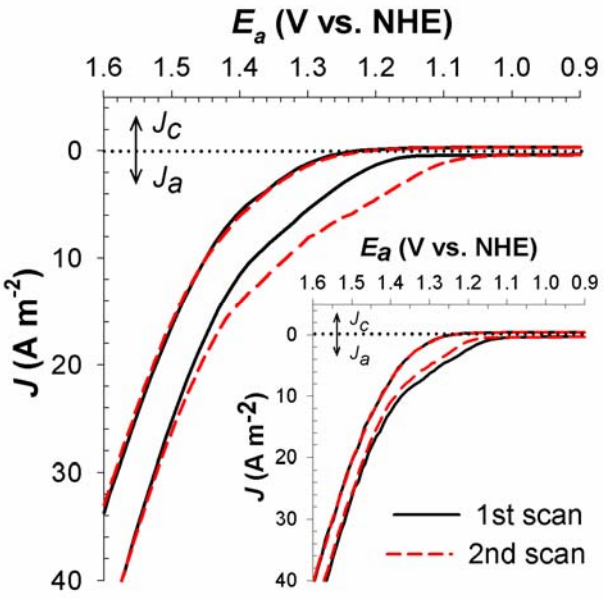

Figure 4.2. Cyclic voltammetry (CV) of a single compartment electrolysis cell with 50 mM NaCl (σ: 5.5 mS cm^{-1}, R: 4.5 Ω, pH: 6.6) or 50 mM $NaClO_4$ (inset, σ: 5.1 mS cm^{-1}, R: 4.6 Ω, pH: 6.6) solution (275 mL).

$$MO_x + H_2O \xrightarrow{k_1} MO_x(\cdot OH) + H^+ + e^- \quad (4.1)$$

$$MO_x(\cdot OH) \xrightarrow{k_2} MO_{x+1} + H^+ + e^- \quad (4.2)$$

$$MO_x(\cdot OH) \xrightarrow{k_{3a}} MO_x + 1/2\ O_2 + H^+ + e^- \quad (4.3a)$$

$$MO_{x+1} \xrightarrow{k_{3b}} MO_x + 1/2\ O_2 \quad (4.3b)$$

The physi-sorbed ($MO_x(\cdot OH)$) and chemi-sorbed (MO_{x+1}) active oxygen would in turn react with Cl^- to form the RCS, resulting in an indirect oxidation of environmental pollutants, while reactions of the $MO_x(\cdot OH)$ or surface-trapped holes with electron donors is often classified as direct oxidation.[4,6] The contribution of the surface bound hydroxyl radicals can be estimated by monitoring the current variation at a fixed E_a under

a sequential addition of an organic electron donor (*e.g.*, formate).[37] As shown in Figure 4.3, the measured formate concentration did not deviate from the stepwise increasing time profile (without degradation), while the current variation was marginal as well. Therefore, the $MO_x(\cdot OH)$ or the valence-band hole do not appear to be major contributors in oxidation pathways on the BiO_x/TiO_2 anode. The negligible heterogeneous surface degradation of formate might be partially attributed to a mass transport limitation to the anode surface. However, we propose that an internal oxidation of Bi(III) to the higher Bi(V) valence state would rapidly quench the $MO_x(\cdot OH)$. Figure 4.1c illustrates the chrono-amperometric current response in 10, 30, and 50 mM NaCl solutions. In a lower anodic potential region, the relationship between the log J and $E_a - iR$ was governed by a linear Tafel equation, with a slope of 228 mV decade^{-1} independent of the [Cl^-]. The magnitude of the Tafel slope, which has been used to elucidate the rate determining step (RDS) in a multi-step reaction sequence,[24,25,38] suggests that the formation of $MO_x(\cdot OH)$ (eq 4.1) would be the RDS with a charge transfer coefficient around 0.25. The α-phase Bi_2O_3 is known to have one quarter of an oxide vacancy per unit cell.[27] In addition, partial substitutions of Ti^{4+} with the effective ionic radius (r_{ion}) of 61 pm by Bi^{3+} with r_{ion} of 103 pm provide for additional oxide vacancies that are favorable to the III/V valence state transition.[35] The minor direct oxidation efficacy, which is related with oxygen deficiencies,[5] has been previously demonstrated for RuO_x/TiO_2 electrodes.[8,12,21,39]

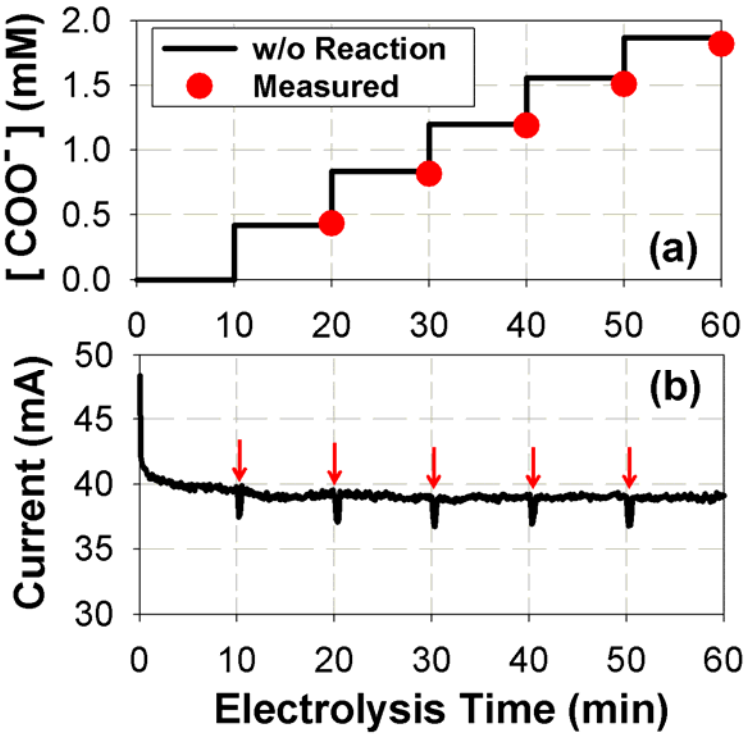

Figure 4.3. (a) Evolution of the formate concentration and (b) current variation under sequential substitution (2 mL, arrows) with 10 mM NaCOOH (σ: 0.92 mS/cm) in a potentiostatic (E_a: 3 V), single compartment electrolysis cell; initial electrolyte: 5.3 mM KH_2PO_4 47.5 mL (pH: 7.2, σ: 0.92 mS/cm).

Several possible reaction mechanisms for the chlorine evolution reaction (CER) on the RuO_2 or RuO_2/TiO_2 are consistent with the MO_{x+1} surface species as the dominant reactive site for chloride oxidation.[24,25,38] In a typical sequence, Cl^- is initially oxidized to a surface bound ClO^- (eq 4.4a), which in turn reacts with another chloride in bulk aqueous solution or on the electrode surface to produce Cl_2 (eq 4.4b). In addition, an $E_a - iR$ exceeding the E of $Cl_2^-\cdot/Cl^-$ couple (2.0 V) should allow for the generation of chlorine radicals (eqs 4.4c and 4.5c), whose decay rate constants to Cl_2 are in the order of 10^9 M^{-1} s^{-1} .[7] Regardless of the terminal step in the mechanism, the RCS generation is

characterized as first order in [Cl^-] with a pseudo-steady-state approximation on $MO_x(ClO^-)$.[25] At circum-neutral pH, the Cl_2 reacts with water to form hypochlorous acid, hypochlorite, H^+, and Cl^- (eqs 4.5a and 4.5b).

$$MO_{x+1} + Cl^- \xrightarrow{k_{4a}} MO_x(ClO^-) \quad (4.4a)$$

$$MO_x(ClO^-) + Cl^- + 2H^+ \xrightarrow{k_{4b}} MO_x + Cl_2 + H_2O \quad (4.4b)$$

$$MO_x(ClO^-) + Cl^- + H^+ \longrightarrow MO_x(\cdot OH) + Cl_2^{-}\cdot \quad (4.4c)$$

$$Cl_2 + H_2O \xleftrightarrow[k_{-5a}]{k_{5a}} HOCl + Cl^- + H^+ \quad (4.5a)$$

$$HOCl \xleftrightarrow[k_{-5b}]{k_{5b}} ClO^- + H^+ \quad (4.5b)$$

$$Cl_2^{-}\cdot \longleftrightarrow Cl\cdot + Cl^- \quad (4.5c)$$

In the subsequent scan in NaCl solution (dashed line in Figure 4.2), there was a significant decrease in the current onset potential to 1.06 V. The earlier onset of the anodic current observed in the chloride solution could be ascribed to the formation of chlorate, which is a major by-product detected in the wastewater electrolysis (*vide infra*), along with the build-up of the RCS during the initial scan. The second onset potential did not explicitly coincide with the *E* values of ClO_3^-/Cl_2 (1.47 V at pH 0, 0.97 V at pH 7), ClO_3^-/HOCl (1.44 V at pH 0, 0.92 V at pH 7), and ClO_3^-/ClO^- (1.36 V at pH 0, 0.94 V at pH 7) couple. However, given the bulk solution near neutral pH, it is conceivable to assume that HOCl or ClO^- should be the primary reductants leading to chlorate production (eq 4.6).[40,41] The reaction scheme described herein neglects perchlorate

formation and direct oxidation of chloride to chlorate,[42] which are reported to occur in a very high anodic bias (in the order of 10^3 A m^{-2} in terms of J).[40,43]

$$2MO_{x+1} + ClO^- \xrightarrow{k_{6a}} 2MO_x + ClO_3^- \quad (4.6a)$$

$$2MO_{x+1} + HOCl \xrightarrow{k_{6b}} 2MO_x + ClO_3^- + H^+ \quad (4.6b)$$

4.3.3. Electrochemical Kinetics in Dilute Chloride Solutions. The polarization curve of Figure 4.1c shows an inflection in the current response with an augmentation of J in 30 and 50 mM NaCl solutions. An incremental transition of the Tafel slope is generally interpreted as an artifact of a mass transport limitation or a shift in the RDS[24]. If we consider that the RDS at a low E_a is due to the electron transfer reaction of eq 4.1, then the reactions involving the MO_{x+1} (eqs 4.3b, 4.4a, and 4.6) become important as the E_a increases. In the chemical reaction limited regime, heterogeneous reactions including OER, CER, and chlorate evolution reactions should not significantly depend on the $E_a - iR$.[23] At a relatively large value of η, the active sites would be virtually saturated with the higher oxide valence states; *i.e.*, quasi constant $[MO_{x+1}]$ in the Nernstian equilibrium between MO_x and MO_{x+1}. If we define free chlorine (FC) as the sum of Cl_2, HOCl, and ClO^-,[14,28,40] then the electrochemical conversion of the chloride can be treated as a simple first-order reaction in series, where the overall kinetics is governed by eqs 4.7 – 4.9 (the complete derivation given in Supporting Information). Even in the presence of chlorine radicals, their short lifetimes should allow the [RCS] to be comparable with [FC], which was quantified as Cl_{DPD} in this study. The utilization of the FC as a single component can be rationalized by an existence of the most abundant reaction intermediate, whose

speciation would be dependent on the wastewater composition and the operating condition.

$$\frac{d[Cl^-]}{dt} = -k_{4a}[MO_{x+1}][Cl^-] = -k_4^{eff}[Cl^-] \quad (4.7)$$

$$\frac{d[FC]}{dt} = k_{4a}[MO_{x+1}][Cl^-] - k_{6a}[MO_{x+1}]^2[FC] = k_4^{eff}[Cl^-] - k_6^{eff}[FC] \quad (4.8)$$

$$\frac{d[ClO_3^-]}{dt} = k_{6a}[MO_{x+1}]^2[FC] = k_6^{eff}[FC] \quad (4.9)$$

Figure 4.4 shows the evolution of the Cl^-, FC, and ClO_3^- concentrations during a potentiostatic electrolysis in chloride solutions with initial chloride concentrations ($[Cl^-]_0$) of 30 and 50 mM. Anionic chlorine species with other oxidation states (ClO_2^-, ClO_4^-) were not detected. Despite the different current response (J = 232 ± 20 A m^{-2} in $[Cl^-]_0$ of 30 mM, 364 ± 23 A m^{-2} in 50 mM), the concentration of each chlorine species when normalized by $[Cl^-]_0$ is governed by identical kinetic parameters. This observation demonstrates that the CER and chlorate evolution reactions are in chemical reaction limited regime. The chlorate evolution rate was found to increase with time; this provides further corroboration that the oxidation of FC is responsible for the chlorate formation.[40,41] The apparent first-order behavior for the reactions taking place on the BiO_x/TiO_2 anode suggests that a plug-flow or sequential-batch reactor would be preferred to a continuous stirred-tank reactor in terms of the yield and selectivity for the FC. The least-squares estimates for the rate coefficients are 0.17 hr^{-1} for k_4^{eff} and 0.37 hr^{-1} for k_6^{eff} using all data sets. However, there are some deviations from the regression lines that are most likely due to potential interference of cathodic reactions, which reduce the RCS to

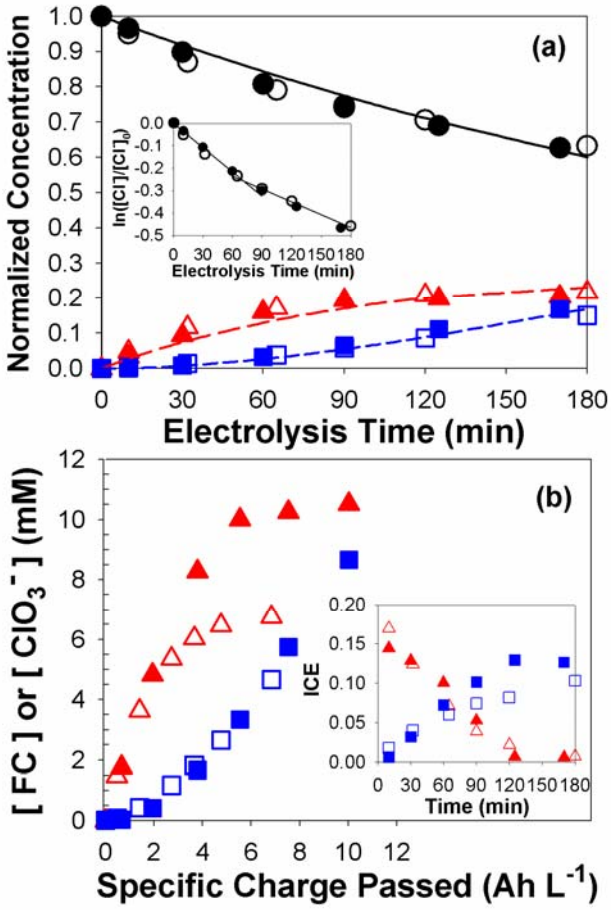

Figure 4.4. The variation of chloride (circle), free chlorine (triangle), and chlorate (square) concentration as a function of (a) electrolysis time and (b) specific charge passed during potentiostatic (E_a: 3 V) electrolysis in 30 mM (filled, R: 7.0 Ω) and 50 mM (empty, R: 5.0 Ω) NaCl solution (55 mL). The inset figures in (a) and (b) show the logarithmic normalized chloride concentration and the instantaneous current efficiency versus the electrolysis time.

chloride.[7,15] As shown in Figure 4.4a (inset), the k_4^{eff} slightly decreased with the augmentation of the FC concentration. The cathodic FC reduction constitutes a null electrochemical cycle with the Cl species as an electron relay,[7] reducing the apparent rate and current efficiency of the desired reactions (pollutants removal and hydrogen generation). With another least-squares estimation using the initial data points, we

obtained 0.24 hr^{-1} for k_4^{eff} and 0.36 hr^{-1} for k_6^{eff}, which can be used to estimate the rate constants for the homogeneous reactions between the RCS and electron donors (*vide infra*).

The instantaneous current efficiency (ICE) and general current efficiency (GCE) are figures of merit, which have been frequently used to evaluate the selectivity of the passed charge towards the chemical contaminants oxidation or RCS generation.[4,6] For an electrolysis cell with chloride and water as electron donors, the ICE for FC and chlorate can be expressed as follows (from eqs 4.3b, 4.8, and 4.9):

$$ICE_{FC} = \frac{i_{FC}}{i_{O_2} + i_{FC} + i_{ClO_3^-}} = \frac{2(k_4^{eff}[Cl^-] - k_6^{eff}[FC])}{2k_3^{eff} + 2k_4^{eff}[Cl^-] + 4k_6^{eff}[FC]} = \frac{2VFd[FC]}{i\,dt} \quad (4.10)$$

$$ICE_{ClO_3^-} = \frac{i_{ClO_3^-}}{i_{O_2} + i_{FC} + i_{ClO_3^-}} = \frac{4k_6^{eff}[FC]}{2k_3^{eff} + 2k_4^{eff}[Cl^-] + 4k_6^{eff}[FC]} = \frac{4VFd[ClO_3^-]}{i\,dt} \quad (4.11)$$

where, i_{O2}, i_{FC}, and i_{ClO3}- refer to the current used for generation of oxygen, FC, and chlorate, k_3^{eff} represents $k_{3b}[MO_{x+1}]$, while V is electrolyte volume and F is Faraday's constant. Figure 4.4b depicts [FC] and $[ClO_3^-]$ as a function of the specific charge passed for which the tangential slope is proportional to the ICE. The GCE at a specific time, defined as the charge required for an observed product divided by the total passed charge, is visualized by the slope of a secant line toward the initial point. As readily expected from eqs 4.10 and 4.11 and the analytical solutions of eqs 4.7 – 4.9 (eqs 4.34 and 4.36), the ICE_{FC} monotonically decreases along with the electrolysis time or passed charge, while the GCE_{FC} is always higher than the ICE_{FC} (*vice versa* for the chlorate). The initial ICE_{FC} should be a strong function of $[Cl^-]_0$ (eq 4.35), consistent with the literature on

chlorine evolution with metal oxide electrodes.[9,44] However, the initial ICE_{FC} was near 0.15 irrespective of the difference in $[Cl^-]_0$, while the effects of $[Cl^-]_0$ were more discernible for the initial ICE for chlorate formation. This observation indicates that the OER is not completely determined by the MO_{x+1} dismutation (eq 4.3b), but is also influenced by the electron transfer reactions (eqs 4.1 and 4.2), where k_3^{eff} could increase in part with the σ or $[Cl^-]_0$.

The observed first-order decrease of $[Cl^-]$ can also be a consequence of a mass transport limitation, whose impact can be roughly assessed by the limiting current density (J_L) as shown in eq 4.12:[34,45]

$$J_L = n\,F\,k_m^{\,Cl}\,[Cl^-], \tag{4.12}$$

where, n is the number of electrons for Cl^- oxidation (2) and k_m^{Cl} is the mass transfer coefficient for Cl^-. If k_m^{Cl} is assumed to be on the order of 10^{-5} m s^{-1},[46,47] then the J_L can be estimated to be 96 A m^{-2} for 50 mM NaCl solutions and 58 A m^{-2} for 30 mM solutions. These values are approximately 70% higher than the current density used for the FC formation (J multiplied by ICE_{FC}). This implies that chloride oxidation would not be in the transport-controlled regime. Even if a mass transport limitation is operative, the forms of kinetic equations are essentially the same.

4.3.4. Electrochemical Treatment of Fresh Urine. Preliminary experiments were performed to assess the performance of the WEC when fresh human urine is oxidized under potentiostatic condition (E_a: 3 V). During the electrochemical oxidation, intense foaming was observed, most likely due to an interaction of the electrolytically produced

bubbles (*i.e.*, O_2 and H_2) with proteins. In addition, precipitation of $CaCO_3$ and $Mg(OH)_2$ occurred on the cathode. The scale deposition is facilitated by high pH in the vicinity of the cathodes, presumably due to the consumption of protons during hydrogen production. In this situation, subsequent electrolyses were carried using fresh urine that was diluted with Milli-Q water by a volume ratio of 1:3. The cathodic deposit in calcareous form was corroborated by monotonic decreases of [Ca^{2+}] and [Mg^{2+}], as shown in Figure 4.5b (inset).

In spite of the $[Cl^-]_0$ in diluted urine of 45 mM, the observed rate of Cl^- decay as well as the production rates of FC and ClO_3^- (as shown in Figure 4.5a) were much smaller than those measured in NaCl solution. In this experiment, the Cl_{DPD} can be composed of either FC or combined chlorine, although each contribution cannot be estimated precisely by the chlorine mass balance analysis (see analytical details in the Supporting Information) due to the bulk pH (6.6) smaller than the pKa of HOCl (7.5). The slower kinetics that were observed during the chlorine redox cycle can be attributed to facile homogeneous reactions of FC, with the various electron donors present in urine being reduced back to chloride rather than further oxidized to chlorate. However, there was little net elimination of COD after 6 h (Figure 4.5b), which is most likely due to the presence of macro-molecular organic compounds. The proteins concentration in the diluted urine was 8 times higher than in the DWW (Table 4.1). The decomposition of high-molecular-weight organic compounds, which may be refractory to dichromate digestion in COD analysis, may have caused partial increase of the detectable COD. Since E of $Cr_2O_7^{2-}/Cr^{3+}$ (1.36 V at pH 0) exceeds the corresponding potentials of ClO^-/Cl^- or $HOCl/Cl^-$ at circum-neutral pH, the FC would transform the recalcitrant organics

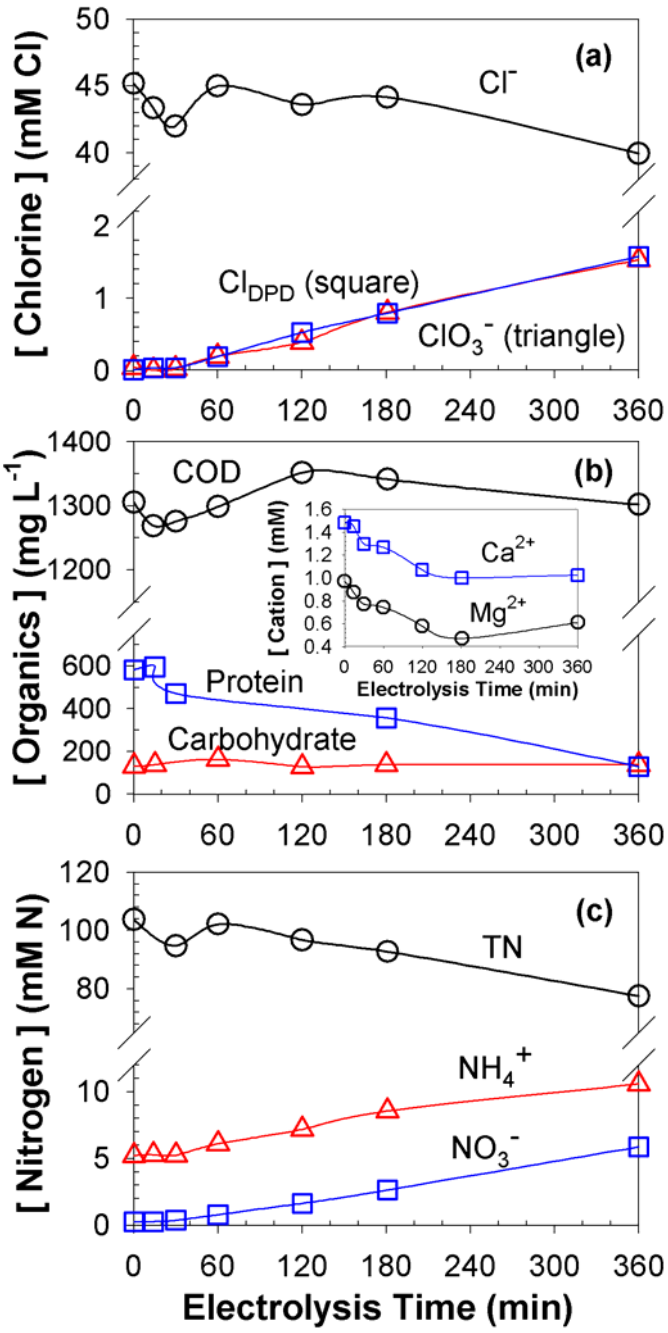

Figure 4.5. Evolution of (a) chlorine species, (b) organic species, (c) nitrogen species, and (b inlet) cations (Ca^{2+}, Mg^{2+}) concentration in a potentiostatic (E_a: 3 V) WEC experiment (J: 247 ± 6 A m^{-2}, $E_a - iR$: 2.15 ± 0.02 V, $E_a - E_c$: 5.41 ± 0.04 V) with diluted human urine (pH: 6.6, σ: 6.05 mS/cm, 55 mL).

to be kinetically amenable to the dichromate. The concentration profile of protein (Figure 4.5b), in terms of the abundance of peptide bonds determined via the Lowry method,[31] gave a pseudo first-order rate coefficient of 0.23 hr^{-1}; this indicates that the organic transformation by the FC involves cleavages of the peptide bonds.

About 80% of the initial TN in diluted urine was contributed by urea (Table 4.1) with additional contributions from creatinine, uric acid, amino acids, and protein. Figure 4.5c shows that the degradation of the nitrogen containing organics resulted in the production of ammonium ion, nitrate, and gaseous nitrogen expressed by the decrease in the TN concentration. The urea degradation by the FC is known to initiate by sequential chlorination of the urea to tetrachlorourea which is further oxidized to the chloramine species.[48] The inorganic combined chlorine eventually yields ammonium ion, nitrogen gas (by dismutation of chloramines in so-called breakpoint chlorination mechanism), and nitrate via further oxidation by FC.[9,49,50] The high concentration of refractory organics in the fresh urine required an extended electrolysis time for apparent COD conversion. In light of this observation, a combination with biological pre-treatment including anaerobic digestion is used to enhance pollutants conversion and to increase the energy efficiency of the electrochemical treatment,[34,36,47] as demonstrated in this study (*vide infra*).

4.3.5. Chlorine Transformation in the WEC with Model Septic Tank Effluents. During the potentiostatic (E_a: 3 V) WEC experiments with STEs, J was observed to be comparable to those in sodium chloride solution (Figure 4.6a). Therefore, we assume that the redox kinetics for the various chlorine species are in a chemical reaction limited regime. The main oxidizable components in the STEs were ammonium ion and organic

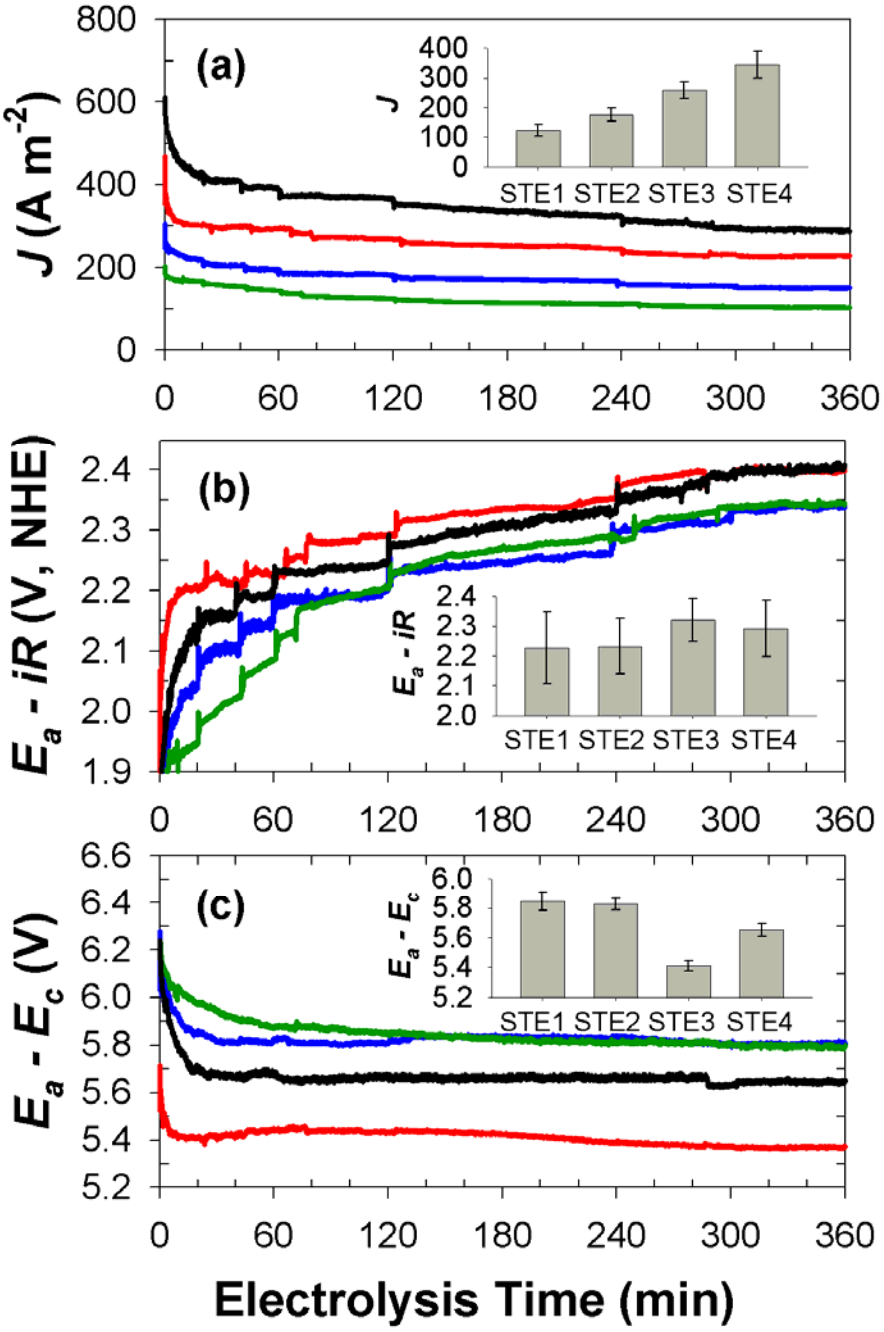

Figure 4.6. Evolution of (a) current density (J), (b) iR-compensated anodic potential ($E_a - iR$), and (c) cell voltage ($E_a - E_c$) in potentiostatic (E_a: 3 V) WEC experiment with model septic tank effluents; STE1 (green), STE2 (blue), STE3 (red), STE4 (black). Each inset figure shows the mean value with standard deviation in the error bars.

compounds in terms of COD (Table 4.1). Their homogeneous reactions with the FC can be expressed by the following non-stoichiometric reactions:

$$COD + FC \xrightarrow{k_{13}} Product + Cl^- \quad (4.13)$$

$$2NH_4^+ + 3FC \xrightarrow{k_{14}} N_2 + 3Cl^- \quad (4.14)$$

$$NH_4^+ + 4FC \xrightarrow{k_{15}} NO_3^- + 4Cl^- \quad (4.15)$$

Assuming that bimolecular reactions occur between the ammonium ion and FC with overall second order kinetics would be ideal, since reactions 14 and 15 are most likely to proceed via sequential chlorination, producing chloramines as reaction intermediates.[9] In this context, the governing equations for FC in the presence of oxidizable chemical species can be modified as:

$$\frac{d[FC]}{dt} = k_4^{eff}[Cl^-] - k_6^{eff}[FC] - k_{13}[FC][COD] - (3k_{14}+4k_{15})[FC]\left[NH_4^+\right] \quad (4.16)$$

Figure 4.7 illustrates the evolution of Cl_{DPD}, following a typical break-point chlorination curve,[49] whose concentration was much smaller than $[Cl^-]_0$. In addition, the sum of apparent $[Cl^-]$, including $[ClO^-]$, $[ClO_3^-]$ and $[Cl_{DPD}]$, was always conserved with standard deviations less than 0.1 mM. The initial pH of the STEs was near 9 (Table 4.1) due to urea hydrolysis during anaerobic pre-treatment. The bulk pH did not change significantly during electrolysis because of the inherent buffering capacity of STEs and bicarbonate generation from COD oxidation. Therefore, Cl_{DPD} should be dominated by the sum of the combined chlorines, which followed a typical time profile for intermediates of reactions in series. The insignificant concentrations of FC again imply

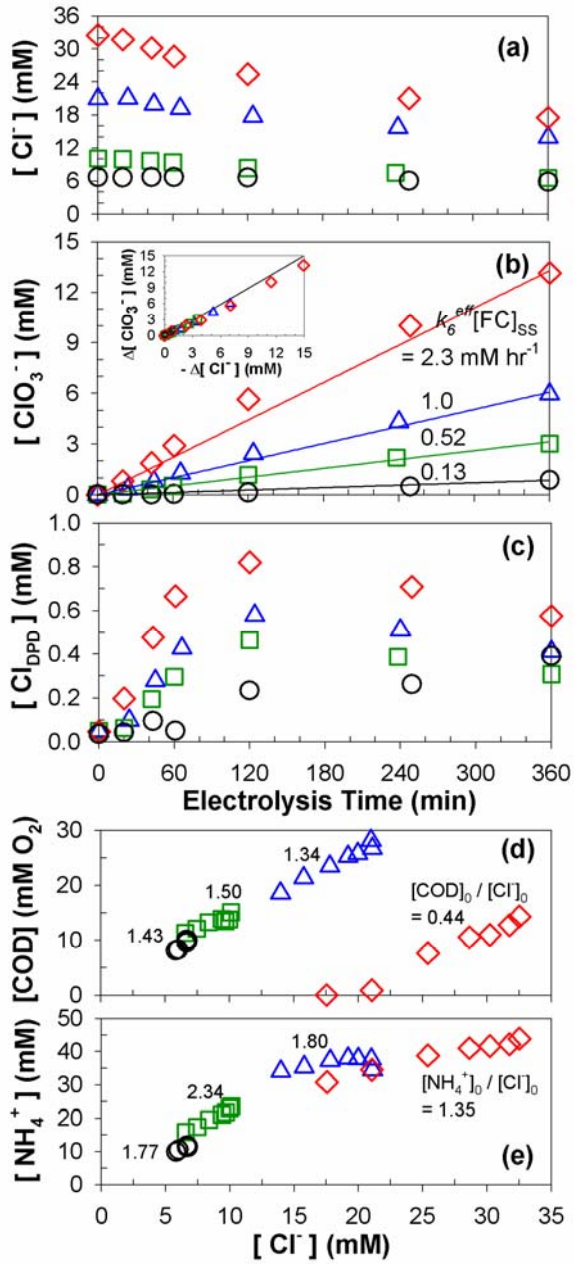

Figure 4.7. Time profiles of (a) chloride, (b) chlorate, and (c) Cl_{DPD} concentration together with (b, inset) scatter plots of increase of chlorate versus decrease of chloride concentration, (d) COD versus chloride concentration, and (e) ammonium ion versus chloride concentration in potentiostatic (E_a: 3 V) WEC experiments with model septic tank effluents; STE1 (circle), STE2 (square), STE3 (triangle), STE4 (diamond).

facile homogeneous reactions between FC and the constituent pollutants, which allows for a pseudo-steady-state approximation for the FC concentration ($[FC]_{SS}$). With a quasi-constant FC concentration, eq 4.16 indicates a linear correlation of $[Cl^-]$ with [COD] and $[NH_4^+]$ for each experimental condition, as demonstrated in Figure 4.7d and 4.7e. At given values of k_4^{eff} and k_6^{eff} under quasi-saturated active sites, the $[FC]_{SS}$ will be a function of the initial chloride concentration ($[Cl^-]_0$), the initial ratio of pollutants to chloride concentration ($[COD]_0/[Cl^-]_0$, $[NH_4^+]_0/[Cl^-]_0$), and the rate coefficients for specific pollutant degradation (k_{13}, k_{14}, k_{15}).

In the STEs electrolysis, a major by-product was again found to be chlorate ion, whose production rate appeared to be nearly unchanged with time (zero-order kinetics), as shown in Figure 4.7b and expressed by eq 4.9 at a constant $[FC]_{SS}$. Using the value of k_6^{eff}, the $[FC]_{SS}$ recorded in the slopes of the chlorate concentration profiles were estimated to be 0.34, 1.4, 2.8 and 6.3 mM (higher than the bulk $[Cl_{DPD}]$). As noted in the literature,[34] there should be concentration gradients for the heterogeneous reactants and products in electrode vicinity, often referred to boundary layer or reaction cage. Owing to higher reactivity and molecular weight, the FC gradient would be more pronounced than the chloride gradient so that the $[FC]_{SS}$ in the boundary layer can exceed the bulk $[FC]_{SS}$. Given our previous arguments, the characteristic mass balance equations can be written for the near-surface of the anode and bulk solution separately as:

$$\frac{d[FC]^A_{SS}}{dt} = k_4^{eff}[Cl^-] - k_6^{eff}[FC]^A_{SS} - \frac{k_m^{FC}}{\delta}\left([FC]^A_{SS} - [FC]^B_{SS}\right) = 0 \quad (4.17)$$

$$\frac{d[FC]^B_{SS}}{dt} = \frac{k_m^{FC}}{\delta}\left([FC]^A_{SS} - [FC]^B_{SS}\right) - [FC]^B_{SS}\left\{k_{13}[COD] + (3k_{14} + 4k_{15})\left[NH_4^+\right]\right\} = 0 \quad (4.18)$$

In this case, $[FC]^{A}_{SS}$ and $[FC]^{B}_{SS}$ are the quasi-steady-state FC concentrations in the boundary layer and in bulk, k_m^{FC} is the mass transfer coefficient for the FC, and δ is the depth of boundary layer. When $[FC]^{B}_{SS}$ is much lower than $[FC]^{A}_{SS}$ and the k_m^{FC}/δ is constant, eqs 4.17 and 4.43 indicate that $[FC]^{A}_{SS}$ and the corresponding chlorate production rate are strongly dependent on the initial chloride concentration,[40] as shown in Figure 4.7b. On the other hand, as can be inferred from eq 4.18, $[FC]^{B}_{SS}$ should be affected by the initial concentration of pollutants ($[COD]_0$, $[NH_4^+]_0$) as well.

4.3.6. COD Removal Characteristics in WEC with Model Septic Tank Effluents. Figure 4.8 illustrates the evolution of the COD concentration during the WEC experiments using STEs. The COD conversion after 6 h electrolysis was 15%, 25%, and 34% for STE1–3, whereas almost complete mineralization (*i.e.*, conversion to CO_2) of COD was observed for STE4. The pseudo-steady-state assumption for FC allows us to characterize the COD degradation kinetics by a pseudo-first-order rate constant, k_{COD}^{eff}.

$$\frac{d[\mathrm{COD}]}{dt} = -k_{13}[FC]^{B}_{SS}[\mathrm{COD}] = -k_{COD}^{eff}[\mathrm{COD}] \quad (4.19)$$

From a series of nonlinear regressions of eq 4.19 we can estimate k_{COD}^{eff}, which is an order of magnitude higher for STE4 (0.43 hr^{-1}) than for the others (0.041 – 0.066 hr^{-1}). The rate constants depend on $[COD]_0/[Cl^-]_0$ rather than $[Cl^-]_0$, in agreement with previous reports[14,33,51] in which the observed rate constants increased with the relative COD concentration but were not altered by influent dilution. The initial ratio of pollutants-to-chloride concentration would be an important determinant of $[FC]^{B}_{SS}$, as inferred from eq 4.18 with $[FC]^{A}_{SS}$ as a strong function of $[Cl^-]_0$. Therefore, an extended

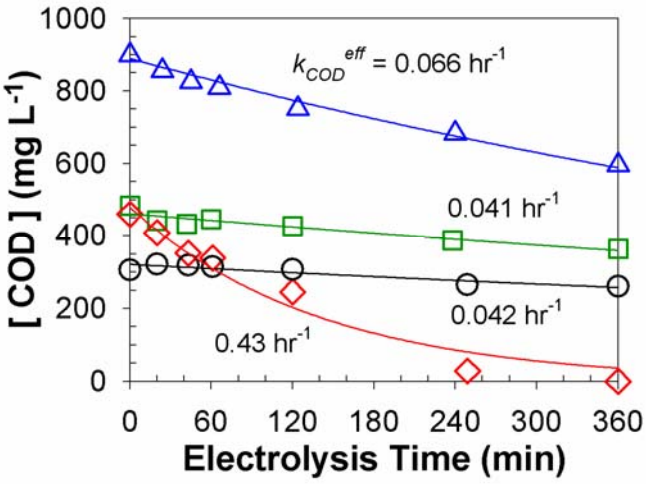

Figure 4.8. Time profiles of COD concentration in potentiostatic (E_a: 3 V) WEC experiments with model septic tank effluents; STE1 (circle), STE2 (square), STE3 (triangle), STE4 (diamond).

anaerobic treatment resulted in STE4 having a lower pollutants-to-chloride ratio than the other STEs (Figure 4.7d and 4.7e) and superior COD conversion. In addition, a lower fraction of recalcitrant organics in STE4 (Table 4.1) also contributed to the higher k_{COD}^{eff} by an augmented k_{13}. Assuming the DWW is analogous to the flushing water for excreta, the recipe of STE4 is rationalized by a low usage of flushing water, which is threefold volume of urine, as would be the scenario in communities with water shortages. The HRT required for STE with a higher flushing would be comparable since the dilution does not affect the ratio of pollutants to chloride concentration, or even smaller when sticking to an effluent water quality criteria.

Consequently, the results for STE4 strongly demonstrate that our WEC is suitable for efficient toilet wastewater treatment system in a relatively short HRT without external chemical dosages, if combined with proper anaerobic pre-treatment unit. It should be

noted that the pre-treatment would require much shorter times than 7 days, since the biological concentration in septic tanks would be much greater than in DWW.

Figure 4.9 details the transformation characteristics for the organic compounds in terms of scatter plots for protein, carbohydrates, and carboxylic acids versus the COD concentration. As in the case of COD, the pseudo first-order rate constant for protein degradation ($k_{protein}^{eff}$) was also much higher for STE4 (2.5 hr^{-1}) than for STE1–3 (1.2 – 1.5 hr^{-1}). In addition, the observed $k_{protein}^{eff}$ exceeds k_{COD}^{eff} by more than an order of magnitude for STE1–3, which suggests that the FC would preferentially attack the nucleophilic sites of organic macromolecules by electrophilic substitution reactions.[7,52] The reactions between FC and the peptides, which have second-order rate constants on the order of $10^6 – 10^7$ $M^{-1}s^{-1}$, are known to initiate by chloramination of terminal amine group.[52] The cleavage of peptides bonds should produce measurable COD (carbonyl compounds and amines with shorter chain lengths), because initial protein degradation was not accompanied by a noticeable decrease of COD (Figure 4.9a). On the contrary, the COD degradation caused increases in carbohydrate and carboxylate concentration (Figure 4.9b and 4.9c), as is reported in a previous work using municipal wastewater.[19] While carboxylate ions (*e.g.*, formate, oxalate, and acetate) are often the observed products of organic compound oxidation,[39,53] the increase in apparent carbohydrate may be due to the release of mono- or oligo-saccharide from decompositions of glycoproteins. The reaction of FC with electron-rich glycosidic bonds in poly-saccharides should also yield simple sugars, which can form hydroxymethylfurfural in the phenol/sulphuric acid analytical method.[32] The reactivity of the FC with oxygenated moieties (alcohol and carboxyl functional groups) in carbohydrates and carboxylic acids are known to be

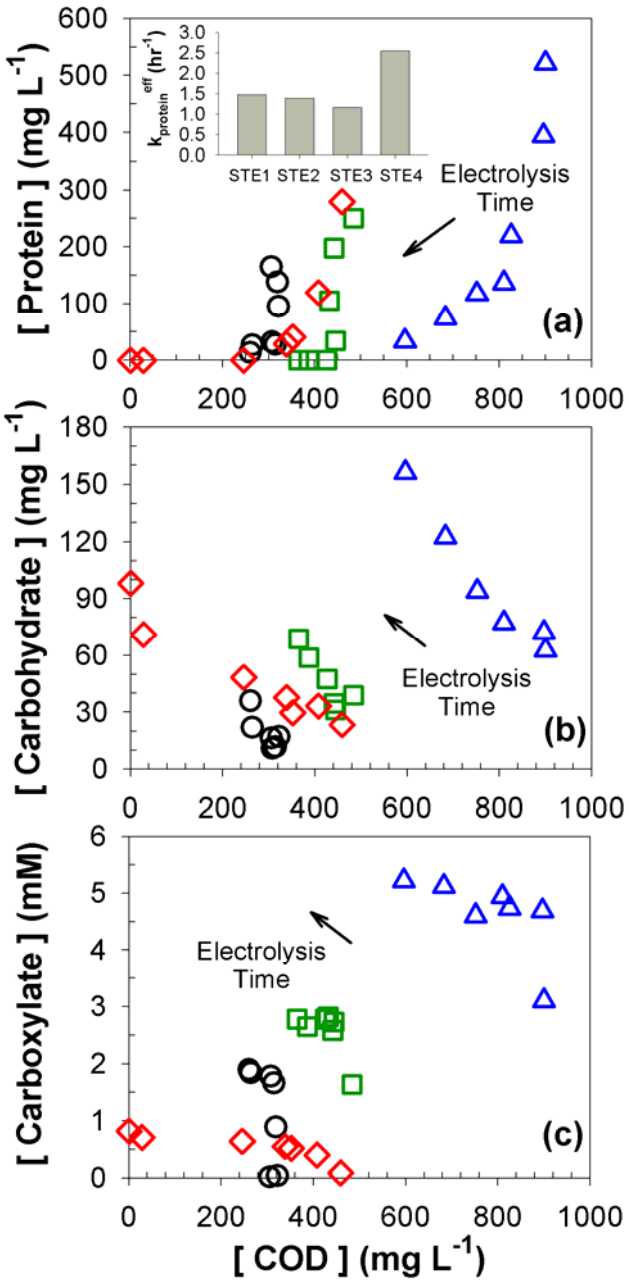

Figure 4.9. Scatter plot for (a) protein, (b) carbohydrate, and (c) carboxylates concentration versus COD concentration together with (a, inlet) pseudo-first-order rate constants for protein degradation in potentiostatic (E_a: 3 V) WEC experiments with model septic tank effluents; STE1 (circle), STE2 (square), STE3 (triangle), STE4 (diamond). Arrows indicate an arbitrary varying direction along with time.

relatively slow.[52,54] Nevertheless, the accumulation of these organic compounds did not significantly contribute to the residual COD of STE4.

4.3.7. Nitrogen Removal Characteristics in the WEC with Model Septic Tank Effluents. The evolution of nitrogen containing compounds, another major constituent of STEs, is illustrated in Figure 4.10. The conversions of TN and NH_4^+ after the 6 h of electrolysis were observed to be less than that of COD, and the TN conversion had a relative order of STE4 (39%) > STE2 (25%) > STE3 (18%) > STE1 (13%). The kinetics of the ammonium ion oxidation can be described in terms of the pseudo-first-order rate constants, k_{am}^{eff}, as follows:

$$\frac{d[NH_4^+]}{dt} = -(3k_{14}+4k_{15})[FC]^B_{SS}[NH_4^+] = -k_{am}^{eff}[NH_4^+] \quad (4.20)$$

As shown in Figure 4.10b, the magnitude of k_{am}^{eff} was not simply correlated with $[FC]^B_{SS}$ as in the case of COD, and the highest rate constant was observed for STE2. Table 4.1 and Figure 4.10a (inset) show that ammonium ion constituted 60 – 70% of TN in STE3–4 and even larger fractions for STE1–2 (higher dilution with DWW). The initial organic nitrogen, in terms of $[TN]_0 - [NH_4^+]_0 - [NO_3^-]_0$, was attributed to urea by more than 50%. As discussed above, the degradation of urea and other nitrogen containing moieties (amines, amides, amino acids, and peptides) will produce ammonium ion via organic chloramine formation and consecutive oxidation.[48,52] As a result, apparent k_{am}^{eff} values were lower for STE3–4 despite the higher levels of $[FC]^B_{SS}$. Figure 4.10a (inset) further visualizes that the ostensible decay rates of TN exceeds those of ammonium for STE3–4. This observation together with low values of $[Cl_{DPD}]$ (Figure 4.7c) suggests that

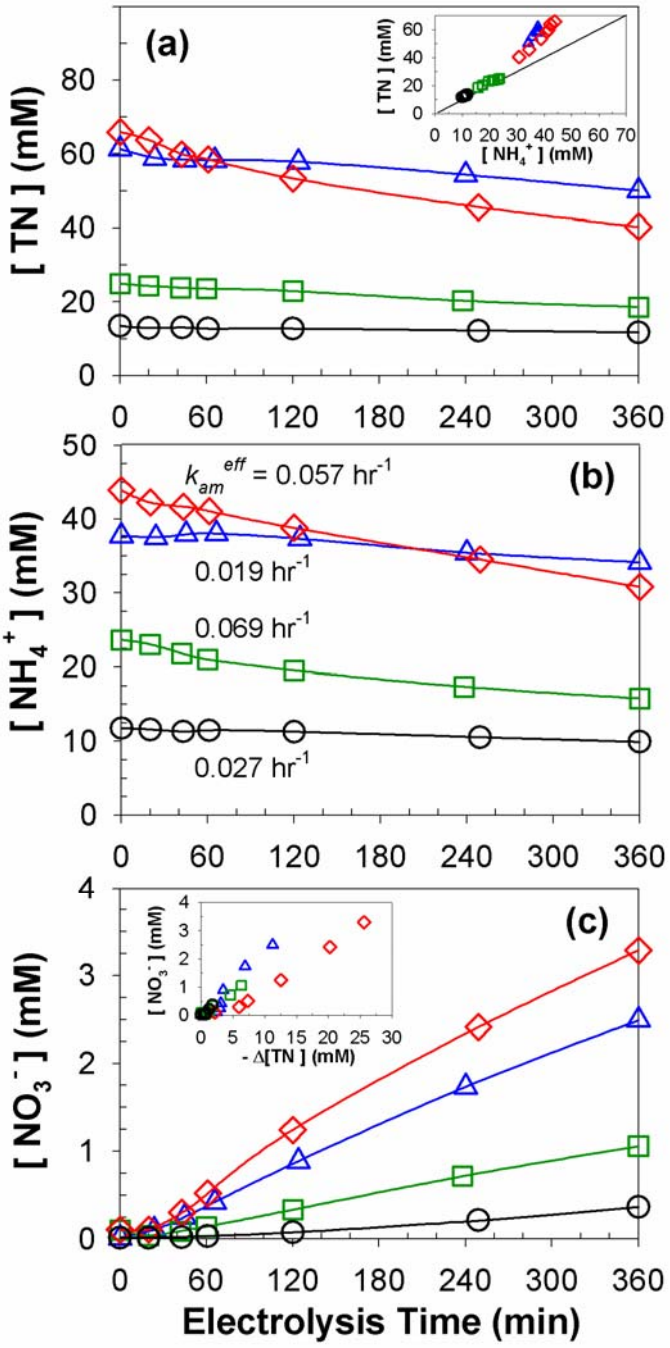

Figure 4.10. Time profiles of (a) TN, (b) NH_4^+, and (c) NO_3^- concentration together with scatter plots for (a, inlet) TN versus NH_4^+ concentration and (c, inlet) NO_3^- versus removed NH_4^+ concentration in potentiostatic (E_a: 3 V) WEC experiments with model septic tank effluents; STE1 (circle), STE2 (square), STE3 (triangle), STE4 (diamond).

gaseous nitrogen generation may not be limited by the dismutation reactions of the chloramine species. The relative reactivity of FC towards amides (including urea) is not as high as the second-order rate constants of FC with ammonium ion, primary/secondary amines, amino acids, and peptides.[52] On the other hand, the observed rates of the TN decay were also greater than nitrate generation rate, as shown in Figure 4.10c (inset), which is more obvious for STE4. Although the mechanism and kinetics for the breakpoint chlorination are not fully known, the dominance of combined chlorine in the Cl_{DPD} allows us to conclude that the disproportionation of chloramines is favored relative to their further oxidation to nitrate, as the chloramine concentration increases. Previous studies on ammonium ion removal from landfill leachates[50] and anaerobic digestion effluents[55] reported similar results in that N_2 formation is favored over nitrate formation as J or $[Cl^-]_0$ increase.

In the case of the STE4 effluent, which had the highest TN conversion, the WEC effluents still had significant nitrogen concentrations (~ 40 mM TN), which were primarily in the form of ammonium ion (76%) and nitrate (8.2%). If we imagine the bioavailability of residual nitrogen, the treated water can then be regarded as a liquid fertilizer if used for irrigation water.

4.3.8. Current Efficiency and Energy Consumption of the WEC with Model Septic Tank Effluents. Based on the kinetic model in this study, the instantaneous current efficiencies for COD degradation and for production of N_2, NO_3^-, and ClO_3^- can be expressed as follows:

$$ICE_{COD} = \frac{4k_{14}[FC]^{B}_{SS}[COD]}{2k_3^{eff} + 2k_4^{eff}[Cl^-] + 4k_6^{eff}[FC]^{A}_{SS}} = -\frac{4VFd[COD]}{i\,dt} \quad (4.21)$$

$$ICE_{N_2} = \frac{3k_{14}[FC]^{B}_{SS}[NH_4^+]}{2k_3^{eff} + 2k_4^{eff}[Cl^-] + 4k_6^{eff}[FC]^{A}_{SS}} = -\frac{3VFd[TN]}{i\,dt} \quad (4.22)$$

$$ICE_{NO_3^-} = \frac{8k_{15}[FC]^{B}_{SS}[NH_4^+]}{2k_3^{eff} + 2k_4^{eff}[Cl^-] + 4k_6^{eff}[FC]^{A}_{SS}} = \frac{8VFd[NO_3^-]}{i\,dt} \quad (4.23)$$

$$ICE_{ClO_3^-} = \frac{6k_6^{eff}[FC]^{A}_{SS}}{2k_3^{eff} + 2k_4^{eff}[Cl^-] + 4k_6^{eff}[FC]^{A}_{SS}} = \frac{6VFd[ClO_3^-]}{i\,dt} \quad (4.24)$$

In these equations, the [COD] should be expressed in molar concentration units (mM O_2), while N_2 is assumed to totally account for the gaseous nitrogen production. The ICE for chlorate production is expressed based on 6-electron transferred from chloride. Compared to the ICE for chloride oxidation in the absence of pollutants (eqs. 4.10 – 4.11, Figure 4.4b) with significant time variations, the differential concentrations of COD, TN, nitrate, and chlorate appeared to be almost linearly correlated with the specific charge passed (Figure 4.11). Accordingly, the ICE did not deviate much from the GCE. These findings can be explained in terms of the pseudo first-order rate constants for pollutant degradation (k_{COD}^{eff}, kam^{eff}) that are much lower than k_4^{eff} and k_6^{eff}. The ICE for organic compound degradation on non-active electrodes such as BDD has sometimes been reported to approach unity initially but decrease with time, as limited by the mass transport of substrate to the anode surface.[54]

A series of linear regressions of the differential concentrations on the specific charge passed can be used to estimate the mean current efficiencies, as illustrated by Figure 4.12a. The results as well as eqs 4.44 – 4.47 indicate that the current efficiencies of the

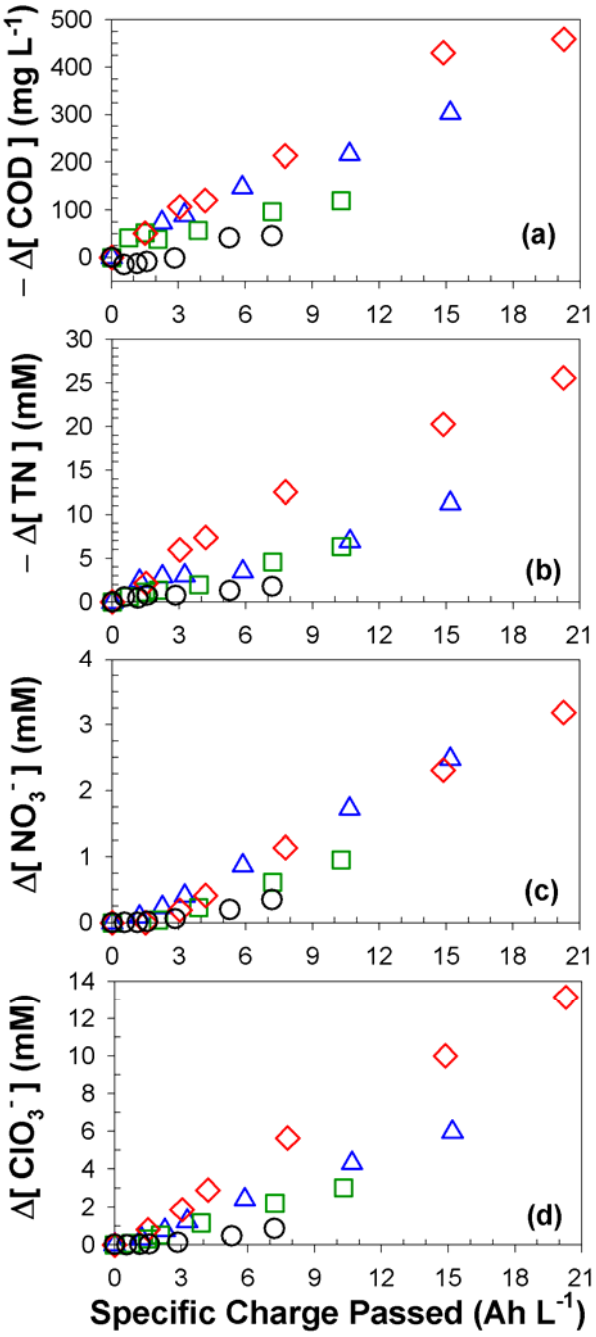

Figure 4.11. Variations in (a) COD concentration, (b) TN concentration, (c) nitrate concentration, and (d) chlorate concentration as a function of specific passed charge in potentiostatic (E_a: 3 V) WEC experiments with model septic tank effluents; STE1 (circle), STE2 (square), STE3 (triangle), STE4 (diamond).

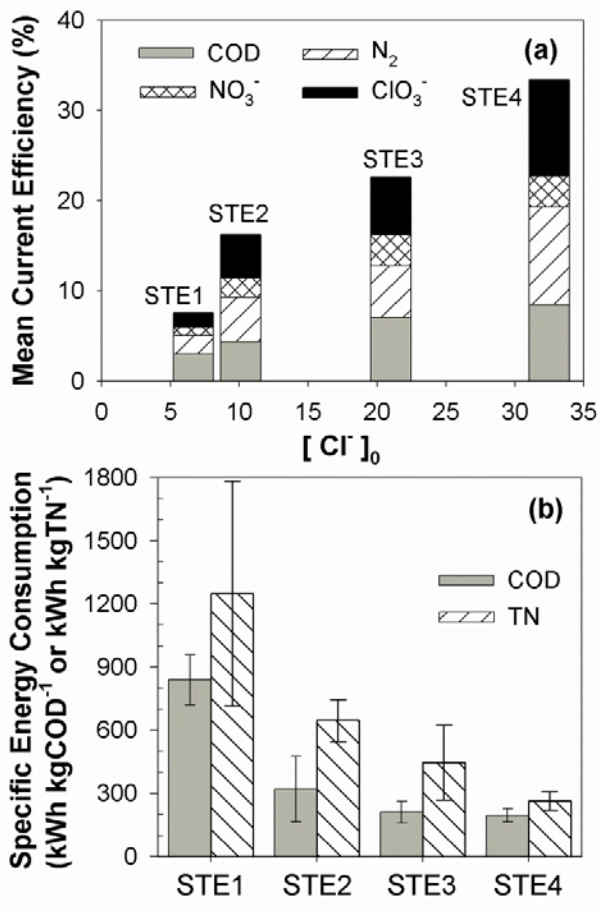

Figure 4.12. (a) Average current efficiency for COD, nitrogen, and chlorine conversion, and (b) specific energy consumption for COD and total nitrogen on average in potentiostatic (E_a: 3 V) WEC experiments with model septic tank effluents. Error bars represent the standard deviation.

FC mediated oxidation are influenced substantially by $[Cl^-]_0$ itself,[10,13,28,56] rather than by the pollutants-to-chloride ratio. The rate of pollutant removal should be a function of $[Cl^-]_0$ only, since it is proportional to the $[FC]^B_{SS}$ multiplied by the pollutant concentrations. At a given $[Cl^-]_0$, eqs. 4.44 – 4.47 further indicate that the relative concentration and reactivity towards the FC govern the charge consumption for each substrate. For example, in STE4, k_{COD}^{eff} exceeds k_{am}^{eff} by a greater extent than in the other STEs, which was

balanced by the lowest value of the [COD]/[NH_4^+] ratio. Independent of the specific STE composition, the charge required for COD reduction was comparable with that for N_2 production, about half of which was consumed for nitrate production. Even though the 'regression toward the mean' analysis would underestimate the individual ICE, the sum of eqs 4.21 to 4.24 as the total current used other than OER was less than 50%. In a previous direct measurement of oxygen evolution from an electrolysis of a chloride solution, we estimated the current efficiency of the OER to be less than 25%.[15]

As can be seen in Figure 4.12b, the energy consumption for unit removal of pollutants also monotonically decreased with the increase in $[Cl^-]_0$. However, the influence of $[Cl^-]_0$ on the SEC is not as significant as on the ICE due to the large increment of J with $[Cl^-]_0$ (Figure 4.6a). These observations suggest that an influent dilution (increase in flushing volume) might reduce the HRT to achieve an effluent quality criteria (*vide supra*), but an increase of energy consumption is inevitable.[14,51] The kinetic model presented herein predicts minor effects of J on the observed rate constants in the chemical reaction limited regime. This model is in general agreement with previous reports on RuO_2 which experimentally showed a saturation dependence of the observed rate constants on J.[12,33,34,57] It is clear that current density plays a crucial role in the direct oxidation rate but not in the indirect oxidation rate.[33,57] Under these conditions, further increases in J should favor OER rather than CER, which in turn decreases the current efficiency of pollutant oxidation but significantly increases the solution resistance, energy loss and SEC.[14] Therefore, a reduction in SEC is expected with an effort to adjust the E_a to maximize the desired current efficiency.

4.3.9. Hydrogen Production in WEC with Model Septic Tank Effluents. Figure 4.13 depicts the quantitative estimates for hydrogen generation as a function of the average *J* value. The rate of total gas production (*Q*) almost linearly increased with the average *J*. The volumetric fraction of hydrogen (X_{H2}) was about 40% under current densities less than 150 A m^{-2} (STE1), while increased to near 60% at higher current densities. However, the dependency of X_{H2} on *J* was not obvious when taking into account the measurement error (coefficient of variation: 11% in maximum) in the GC/TCD analysis. The adverse contribution of gases initially present in the connection tube may explain the lower X_{H2} for STE1. The remaining fractions of the gaseous products would include oxygen, water vapor, nitrogen, carbon dioxide, chlorine, ammonia, and hydrogen sulphide (with minor contribution). The molar flow rate of hydrogen (F_{H2}) is used to estimate the current efficiency for hydrogen generation (CE_{H2}) to be 50% for STE1, increasing to 90% for STE2–4. The hydrogen evolution reaction (HER) has a well-known reaction sequence[20] that proceeds by combination of eq 4.25 with either eq 4.26 or 4.27:

$$HA + C + e^- \rightarrow C(H\cdot) + A^- \quad (4.25)$$

$$C(H\cdot) + HA + e^- \rightarrow H_2 + C + A^- \quad (4.26)$$

$$2\,C(H\cdot) \rightarrow H_2 + 2C \quad (4.27)$$

where C stands for a cathodically active site for the HER and A is the conjugate base of the proton (OH^- or null term in circum-neutral pH). The main constituent acting as the active sites is presumed to be Ni, in the case of Hastelloy C-22 that was used in this study. Ni belongs to a near-summit group of the volcano plots under basic conditions.[20]

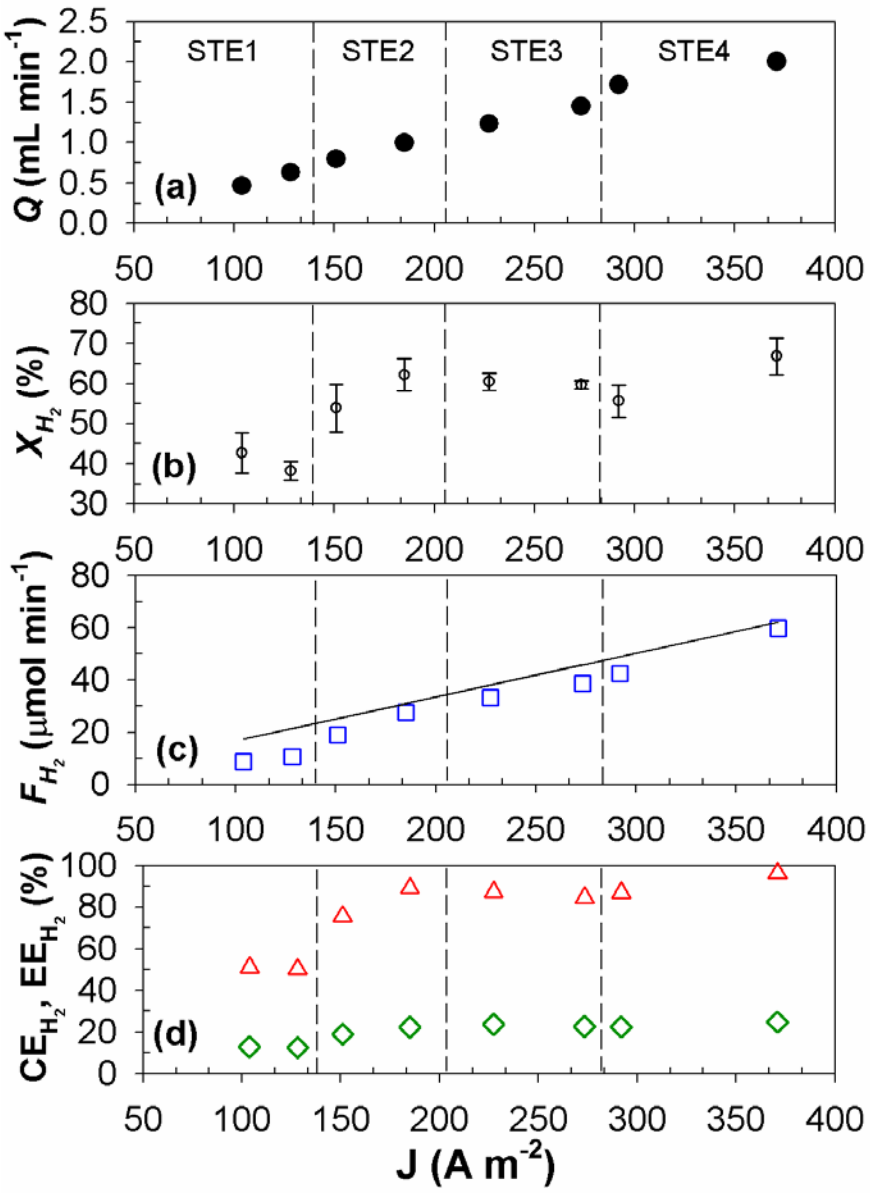

Figure 4.13. Dependency of (a) generation rate of total gaseous products (Q, solid circle), (b) volumetric fraction of hydrogen (X_{H2}, void circle), (c) molar generation rate of hydrogen (F_{H2}, square), (d) current and energy efficiency (CE in triangle and EE in diamond) for hydrogen generation on average current density (J) during gas collection (80 – 110 min and 300 – 330 min) in potentiostatic (E_a: 3 V) WEC experiments with model septic tank effluents. Error bars in (b) represent the standard deviations of repetitive GC/TCD measurement, and the reference line in (c) shows theoretical F_{H2} with CE of 100%.

Ni-based binary or ternary metal composites (with Mo, Co, Cd, and Fe) have been thoroughly investigated for their catalytic HER activity that is dependent on the bond strength between the metal surface and adsorbed hydrogen.

Competitive electron acceptors including oxygen, nitrate, chlorate, and FC can interfere with the HER. The cathodic potential (E_c), which ranged from –2.4 to –2.8 V, is sufficiently below the E of $O_2/HO_2\cdot$ (–0.54 V at pH 7) as well as positive E (spontaneous reduction) of NO_3^-/NO_2^- (0.42 V at pH 7), ClO_3^-/ ClO^-, and ClO^-/Cl^-. The RCS species are clearly the major scavengers of HER and their effects on the CE_{H2} have been documented in our previous reports. For example, Park *et al.*[7] reported that an injection of organic electron donors during electrolysis in NaCl solution results in a sharp increase of CE_{H2} by quenching the RCS. In the present report, anodically generated FC species should engage in facile reactions with pollutants in the bulk phase before being transported to the cathode surface,[34] as demonstrated by the quasi-steady-state FC with a very small bulk-phase concentration ($[FC]^B_{SS}$). The reduction of oxygen to superoxide radical and resulting reactive oxygen species (ROS) were thought to influence the oxidation of pollutants. However, the roles of ROS appear to be marginal in this study because the conversion of COD was insignificant when the chloride concentration was low (STE1).

In spite of the relatively high current efficiency, the energy efficiency for hydrogen generation (EE_{H2}) was observed near 25% for STE2–4, which is much lower than an idealized electrolysis unit. The EE_{H2} has been reported to increase with lowering cell voltage[19] and in synergy with photocatalytic hydrogen evolution on the BiO_x/TiO_2

electrode under direct solar radiation.[18] The energy losses due to the intrinsic overpotential, the ohmic drop, along with the various side reactions in the complex electrolyte system within the WEC may be compensated by a net saving of energy for water treatment and the added costs of electrolyte addition. The US DOE[58] estimated that the wastewater collection and treatment consumes about 60% of the energy requirements for water supply. The impurities in the gaseous product narrow the usage of the hydrogen to an internal combustion (IC) engine without an added purification procedure. Based on the energy efficiency of the current hydrogen IC engines of 35%, a 10% reduction of the SEC is expected with using the hydrogen as a secondary energy source for the WEC.

4.4. OUTLOOK FOR THE FUTURE

Conventional water reuse criteria for non-restricted urban reuse applications are generally based on a BOD of 30 mg L^{-1}.[3] The electrochemically treated water for the STE4 showed negligible COD, suggesting that the treated water is suitable for reuse as toilet flushing water and for irrigation. The relatively facile removal of protein further implies an efficient disinfection of coliforms through complete breakage of bacterial cells and inactivation owing to the reduced carbon source. Since color is also an important consideration for reuse of treated wastewater, we note that the yellowish color was nearly eliminated during WEC treatment as shown in Figure 4.14. However, chlorate production poses a potential health risk, since several drinking water guidelines recommend chlorate concentrations lower than 10 μM.[40] The high level of chlorate most likely will not be a significant problem when using the treated water only for toilet flushing. The chlorate

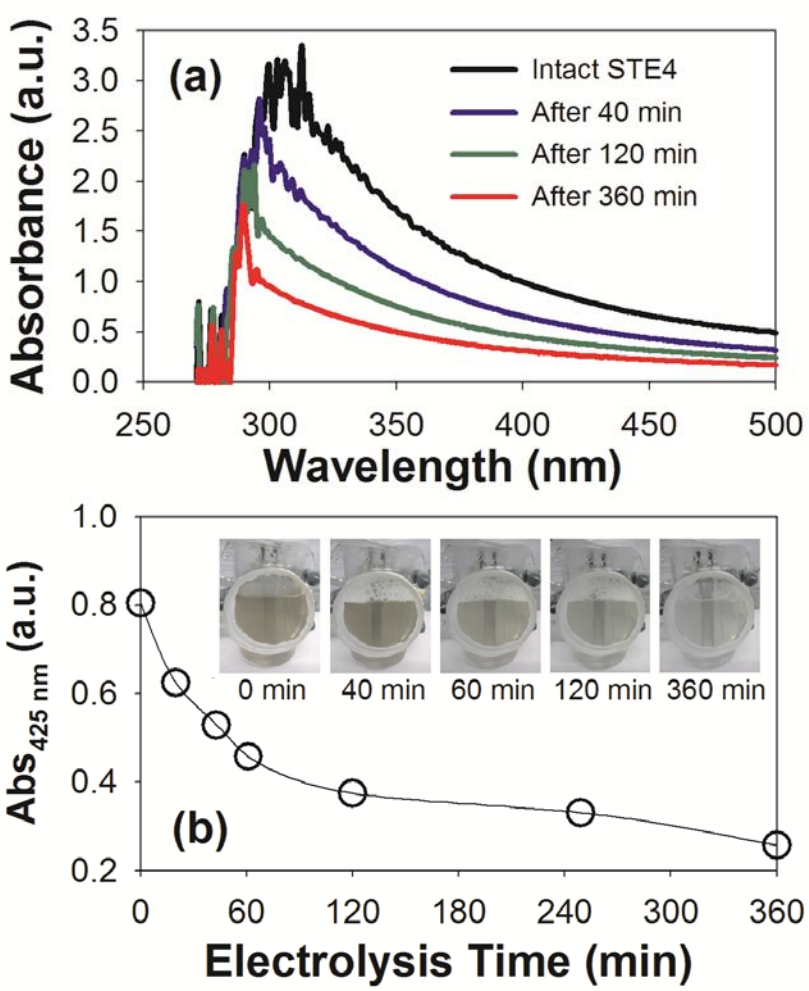

Figure 4.14. (a) Variation in absorbance spectra (270 – 500 nm) along with the electrolysis time and (b) absorbance at 425 nm as a function of electrolysis time in potentiostatic (E_a: 3 V) WEC experiments with STE4. Inset figure in (b) visualizes the color variation.

formation can be reduced with an increase in hydraulic mixing in the WEC resulting in an increase of k_m^{FC}, as inferred from eqs 4.40 and 4.43. A proper selection of cathode materials, known to have a high activity for nitrate reduction (such as bimetallic Cu/Zn[59]), can be another potential solution to facilitate chlorate reduction to chloride under actual operating conditions. These enhancements would be beneficial with respect to increasing

the efficiency of pollutant oxidation even though chlorate reduction could compete with the HER. Calcareous deposits on the cathode surface could result in significant mass transport limitation for hydrogen evolution. Current switching (*i.e.*, polarity) has been shown to remove calcareous deposits, although this would require anti-corrosion cathode material.

The WEC with or without a PV power source has the potential to meet the growing demand for on-site wastewater treatment coupled with water reuse and, in select cases, for alternative fuel production from water-splitting. A scaled-up WEC or PWEC should be easy to transport to various environments, including urbanized areas, peri-urban environments, and remote locations in the developing world that lack viable sanitation facilities to treat domestic black water. These systems may also be used for treatment of industrial wastewaters, landfill leachates, anaerobic sludge digester effluents, and reverse osmosis concentrates.

4.5. SUPPORTING INFORMATION

4.5.1. Materials. NaCl and concentrated sulfuric acid were used as received from Macron Chemicals. Crystalline phenol (99.6%) and $Na_2C_2O_4$ were purchased from J.T. Baker. Total Protein Reagent, Folin-Ciocalteu's phenol reagent, protein standard (bovin serum albumin), $TiOSO_4$, H_2IrCl_6, $[O_2CCH_2C(OH)(CO_2)CH_2CO_2]Bi$, Bi_2O_3, $SnCl_4$, and $TaCl_5$ were received from Sigma Aldrich. Chemical oxygen demand (COD) digestion solution, COD standard solution (potassium acid phthalate), total nitrogen (TN) reagent set, DPD total chlorine reagent powder, and chlorine standard solution were received from Hach. Jack Bean Urease was provided by the Worthington Biochemical Corporation. All other

chemicals were supplied by Mallinckrodt. Ti metal sheet (Ti-Gr.2 sheet, 0.50 mm thick) was purchased from ThyssenKrupp Materials. All electrolyte and standard solutions were prepared in MilliQ water (18.2 MO cm) from a Millipore Milli-Q gradient water purification system.

4.5.2. BiO_x/TiO_2 Electrode Preparation. A Ti metal sheet (0.5 mm thick) was sand-blasted with SiC paper (120 – 240 grits) and degreased with acetone. The precursor solution for the anti-passivation layer was prepared as 73 mM H_2IrCl_6 with 27 mM $TaCl_5$ in 4 M HCl solution. Both sides of pretreated Ti support were brushed by the precursor and annealed at 525 °C for an hour. This procedure was repeated 5 times with the same annealing temperature for a 10 min duration. A sealing coat was deposited twice by painting 225 mM $SnCl_4$ and 12.5 mM Bi_2O_3 in 0.5 M HCl solution and baking at 425 °C for 10 min. Precipitates from dissolving 10 mmol Bi_2O_3 and 0.48 mol $TiOSO_4$ in 1.2 M Na_2CO_3 (1 L) were calcined at 830 °C for 45 min to produce bismuth oxide doped titanium dioxide (BiO_x/TiO_2) nanoparticles. The precursor for the BiO_x/TiO_2 thin film (overcoat solution) was 160 mM $Ti(OCH_2CH_2O)_2$ (*i.e.*, the preparation details are described elsewhere) with 80 mM $[O_2CCH_2C(OH)(CO_2)CH_2CO_2]Bi$ in a 0.24 M NH_4OH solution. To prepare the slurry deposition layer, BiO_x/TiO_2 particles dispersed in MilliQ water (3 M metal concentration) were brushed on air dried; after this step a 25-fold diluted overcoat solution was sequentially pasted on to the surface. The slurry deposit was baked on at 250 for 5 min; this procedure was repeated 7 times. In the final sequence, a thin film of BiO_x/TiO_2 deposit was made by repetitive sealing with overcoat solution annealed at 250 °C (4 times) and then at 450 °C (2 times).

4.5.3. Electrochemical Methods. Before all electrochemical experiments, the electrodes were rinsed with acetone and a large amount of MilliQ water. The electrode module was allowed to equilibrate with the electrolyte solution in an open circuit for 1 h while monitoring the open circuit potential of anode and cathode. As a routine procedure, the pH, conductivity, and the ohmic resistance between anode and reference electrode (R) were measured before and after the electrochemical experiments. The R was measured by current interruption method with current bias of 100 mA. For the chrono-voltammetric data collection, the current intensity (J) was averaged from 400 to 500 seconds. The variation of current density after 500 seconds was not significant, since the p-values of the paired t-test between the averaged current from 400 to 500 seconds and from 500 to 1800 seconds were always larger than 0.05.

4.5.4. Model Septic Tank Effluent Preparation. The COD degradation during the anaerobic incubation followed an exponential decay trend, where initial decomposition of macro-molecules was followed by mineralization of organics with exponential growth of microorganisms, initially presented in domestic wastewater (DWW). Urea was hydrolyzed to give ammonium ion enzymatically using urease; this resulted in an increase of the pH of the model septic tank effluents (STEs) up to 9. The increase in pH resulted in a considerable amount of precipitation of minerals, including magnesium ammonium phosphate (struvite). The supernatant of the collected DWW and prepared STEs was used in the experiments to minimize the effects of particulate matters.

4.5.5. Analyses. COD was measured with standard digestion kits with a low detection range (3 – 150 mg L^{-1}); the kits were prepared in order to eliminate the interference of the ammonium ion in the COD analysis[60] by controlling the kinetics for ammonium and COD

oxidation steps separately. Samples were diluted to adjust the chloride concentration far below the interference range (2,000 mg L^{-1}) as suggested by the digestion kit supplier (Hach, USA). For the Dionex DX-500 Ion Chromatography (IC) system, hypochlorite appeared to have a peak at a retention time identical to the chloride ion with superimposable calibration curves. Since the hypochlorite would be detected both in the IC analysis and total chlorine (Cl_{DPD}) analysis, the sum of [Cl^-], [Cl_{DPD}], and [ClO_3^-] exceeded the initial chloride concentration, particularly for the electrolysis in pure NaCl solution. In this case, [Cl^-] was calibrated by subtracting the difference, which corresponds to [ClO^-]. For urea measurement, 5 mL of diluted samples in 15 mL conical tubes were added by 2 mL of urease solution (63.1 mg L^{-1}) and incubated in water bath (50 °C) for 20 min. Treated samples were cooled down at room temperature (RT) for IC analysis. Urea measurements were performed only for the intact electrolyte before the electrolysis due to the interference of free chlorine. In the phenol-sulfuric acid method,[32] 0.4 mL samples in glass tubes were mixed with 0.4 mL phenol solution (5 W/V%) and 2 mL sulfuric acids (95%) to measure the absorbance at 470 nm after reaction for 30 min at RT. For protein measurement,[31] 0.5 mL samples were introduced to 2.5 mL total protein reagent in 15 mL conical tubes with gentle inversion several times. After reaction for 10 min at RT, twofold diluted Folin-Ciocalteu's phenol reagent of 0.2 mL was added with vigorous mixing. With further holding at RT for 30 min, the absorbance of the supernatant was measured at 600 nm. NH_4Cl, NaOCl, $NaClO_3$, $NaNO_2$, $NaNO_3$, HCOONa, $Na_2C_2O_4$, CH_3COONa, $MgSO_4$, and $CaCl_2$ were used as standards with proper concentration range for the IC analysis. Potassium acid phthalate, NH_4Cl, chlorine, bovine serum albumin, and glucose solution

were used as a standard for COD, TN, Cl_{DPD}, protein, and carbohydrate analysis, respectively.

4.5.6. Kinetic Equations in the Absence of Oxidizable Pollutants. eq 4.28 implies a pseudo-steady-state assumption for the surface bound ClO^-, while eq 4.30 is based on the negligible amount of Cl_2 at circum-neutral pH.

$$\frac{d[MO_x(ClO^-)]}{dt} = k_{4a}[MO_{x+1}][Cl^-] - k_{4b}[MO_x(ClO^-)][Cl^-][H^+]^2 = 0 \quad (4.28)$$

$$\frac{d[Cl^-]}{dt} = -k_{4a}[MO_{x+1}][Cl^-] - k_{4b}[MO_x(ClO^-)][Cl^-][H^+]^2 + k_{5a}[Cl_2] - k_{-5a}[HOCl][Cl^-][H^+] \quad (4.29)$$

$$\frac{d[Cl_2]}{dt} = k_{4a}[MO_{x+1}][Cl^-] - k_{5a}[Cl_2] + k_{-5a}[HOCl][Cl^-][H^+] = 0 \quad (4.30)$$

$$\frac{d[HOCl]}{dt} = k_{5a}[Cl_2] + k_{-5a}[HOCl][Cl^-][H^+] - k_{5b}[HOCl] + k_{-5b}[ClO^-][H^+] - k_{6b}[MO_{x+1}]^2[HOCl] \quad (4.31)$$

$$\frac{d[ClO^-]}{dt} = k_{5b}[HOCl] - k_{-5b}[ClO^-][H^+] - k_{6a}[MO_{x+1}]^2[ClO^-] \quad (4.32)$$

$$\frac{d[ClO_3^-]}{dt} = k_{6a}[MO_{x+1}]^2[ClO^-] + k_{6b}[MO_{x+1}]^2[HOCl] \quad (4.33)$$

Assuming that active sites are saturated at high current densities (quasi-constant $[MO_{x+1}]$), we use eq 4.28 and eq 4.30 in eq 4.29 to obtain

$$\frac{d[Cl^-]}{dt} = -k_{4a}[MO_{x+1}][Cl^-] = -k_4^{eff}[Cl^-] \quad (4.7)$$

By denoting $[FC] = [Cl_2] + [HOCl] + [ClO^-]$, eq 4.30 to 4.32 gives

$$\frac{d[FC]}{dt} = k_{4a}[MO_{x+1}][Cl^-] - k_{6a}[MO_{x+1}]^2[FC] = k_4^{eff}[Cl^-] - k_6^{eff}[FC] \quad (4.8)$$

Assuming that k_{6a} is comparable to k_{6b} and [FC] ~ [HOCl] + [ClO^-] at circum-neutral pH,

$$\frac{d[ClO_3^-]}{dt} = k_{6a}[MO_{x+1}]^2[FC] = k_6^{eff}[FC] \tag{4.9}$$

4.5.7. Instantaneous Current Efficiency (ICE) for Free Chlorine (FC) and Chlorate without the Presence of Pollutants. Substituting the analytical solutions of eq 4.7 to 4.9 to eq 4.10 yields,

$$ICE_{FC} = \frac{2[k_4^{eff}\exp\left(-k_4^{eff}t\right) - \frac{k_4^{eff}k_6^{eff}}{k_6^{eff} - k_4^{eff}}\left\{\exp\left(-k_4^{eff}t\right) - \exp\left(-k_6^{eff}t\right)\right\}]}{\frac{2k_3^{eff}}{[Cl^-]_0} + 2k_4^{eff}\exp(-k_4^{eff}t) + \frac{4k_4^{eff}k_6^{eff}}{k_6^{eff} - k_4^{eff}}\{\exp\left(-k_4^{eff}t\right) - \exp\left(-k_6^{eff}t\right)\}} \tag{4.34}$$

where, $[Cl^-]_0$ denotes the initial chloride concentration.

$$\text{When } t \to 0,\ ICE_{FC} = \frac{k_4^{eff}}{\frac{k_3^{eff}}{[Cl^-]_0} + k_4^{eff}} \tag{4.35}$$

Similarly, the instantaneous current efficiency for chlorate formation is expressed as

$$ICE_{ClO_3^-} = \frac{\frac{6k_4^{eff}k_6^{eff}}{k_6^{eff} - k_4^{eff}}\{\exp\left(-k_4^{eff}t\right) - \exp\left(-k_6^{eff}t\right)\}}{\frac{2k_3^{eff}}{[Cl^-]_0} + 2k_4^{eff}\exp(-k_4^{eff}t) + \frac{4k_4^{eff}k_6^{eff}}{k_6^{eff} - k_4^{eff}}\{\exp\left(-k_4^{eff}t\right) - \exp\left(-k_6^{eff}t\right)\}} \tag{4.36}$$

4.5.8. Kinetic Equations in the Presence of Pollutants. The governing equations for chloride and FC with the presence of pollutants are derived by modifying eq 4.7 and 4.8 as:

$$\frac{d[Cl^-]}{dt} = -k_4^{eff}[Cl^-] + k_{13}[FC][COD] + (3k_{14} + 4k_{15})[FC][NH_4^+] \tag{4.37}$$

$$\frac{d[FC]}{dt} = k_4^{eff}[Cl^-] - k_6^{eff}[FC] - k_{13}[FC][COD] - (3k_{14} + 4k_{15})[FC][NH_4^+] \tag{4.16}$$

By treating the FC mass balance analyses for the bulk-phase and the electrode boundary layer separately, we employ pseudo-steady-state approximations for the FC to give

$$\frac{d[\mathrm{FC}]^{\mathrm{A}}{}_{\mathrm{SS}}}{dt} = k_4^{\,eff}\left[\mathrm{Cl}^-\right] - k_6^{\,eff}[\mathrm{FC}]^{\mathrm{A}}{}_{\mathrm{SS}} - \frac{k_m^{\,FC}}{\delta}\left([\mathrm{FC}]^{\mathrm{A}}{}_{\mathrm{SS}} - [\mathrm{FC}]^{\mathrm{B}}{}_{\mathrm{SS}}\right) = 0 \tag{4.38}$$

$$\frac{d[\mathrm{FC}]^{\mathrm{B}}{}_{\mathrm{SS}}}{dt} = \frac{k_m^{\,FC}}{\delta}\left([\mathrm{FC}]^{\mathrm{A}}{}_{\mathrm{SS}} - [\mathrm{FC}]^{\mathrm{B}}{}_{\mathrm{SS}}\right) - [\mathrm{FC}]^{\mathrm{B}}{}_{\mathrm{SS}}\left\{k_{13}[\mathrm{COD}] + (3k_{14} + 4k_{15})[\mathrm{NH_4^+}]\right\} = 0 \tag{4.39}$$

where, $[\mathrm{FC}]^{\mathrm{A}}{}_{\mathrm{SS}}$ and $[\mathrm{FC}]^{\mathrm{B}}{}_{\mathrm{SS}}$ are quasi-steady-state FC concentration in the anode vicinity and in bulk, $k_m^{\,FC}$ is the mass transfer coefficient for the FC, and δ is the depth of boundary layer. Since $[\mathrm{FC}]^{\mathrm{A}}{}_{\mathrm{SS}} >> [\mathrm{FC}]^{\mathrm{B}}{}_{\mathrm{SS}}$, the solutions of eq 4.38 and 4.39 are reduced to

$$[\mathrm{FC}]^{\mathrm{A}}{}_{\mathrm{SS}} = \frac{k_4^{\,eff}[\mathrm{Cl}^-]}{k_6^{\,eff} + k_m^{\,FC}/\delta} \equiv C_{[FC]^A{}_{SS}}[\mathrm{Cl}^-] \tag{4.40}$$

$$[\mathrm{FC}]^{\mathrm{B}}{}_{\mathrm{SS}} = \frac{\left(k_m^{\,FC}/\delta\right)k_4^{\,eff}[\mathrm{Cl}^-]}{\left(k_6^{\,eff} + k_m^{\,FC}/\delta\right)\left(k_{13}[\mathrm{COD}] + (3k_{14} + 4k_{15})[\mathrm{NH_4^+}]\right)} \equiv \frac{C_{[FC]^B{}_{SS}}[\mathrm{Cl}^-]}{\left(k_{13}[\mathrm{COD}] + (3k_{14} + 4k_{15})[\mathrm{NH_4^+}]\right)} \tag{4.41}$$

Also, the mass balance equation for chloride (eq 4.37) and chlorate (eq 4.9) are modified as

$$\frac{d[\mathrm{Cl}^-]}{dt} = -k_4^{\,eff}[\mathrm{Cl}^-] + k_{13}[\mathrm{FC}]^{\mathrm{B}}{}_{\mathrm{SS}}[\mathrm{COD}] + (3k_{14} + 4k_{15})[\mathrm{FC}]^{\mathrm{B}}{}_{\mathrm{SS}}\left[\mathrm{NH_4^+}\right] \tag{4.42}$$

$$\frac{d[\mathrm{ClO_3^-}]}{dt} = k_6^{\,eff}[\mathrm{FC}]^{\mathrm{A}}{}_{\mathrm{SS}} \tag{4.43}$$

4.5.9. Instantaneous Current Efficiency (ICE) for COD degradation. Substituting eq 4.40 and 4.41 into eqs 4.21 to 4.24 gives

$$\mathrm{ICE_{COD}} = \frac{4C_{[FC]^B{}_{SS}}}{\left(\frac{2k_3^{\,eff}}{[\mathrm{Cl}^-]} + 2k_4^{\,eff} + 4C_{[FC]^A{}_{SS}}k_6^{\,eff}\right)\left(1 + \frac{(3k_{14} + 4k_{15})[\mathrm{NH_4^+}]}{k_{13}[\mathrm{COD}]}\right)} \tag{4.44}$$

$$\mathrm{ICE_{N_2}} = \frac{4C_{[FC]^B{}_{SS}}}{\left(\frac{2k_3^{\,eff}}{[\mathrm{Cl}^-]} + 2k_4^{\,eff} + 4C_{[FC]^A{}_{SS}}k_6^{\,eff}\right)\left(1 + \frac{4k_{15}}{3k_{14}} + \frac{k_{13}[\mathrm{COD}]}{3k_{14}[\mathrm{NH_4^+}]}\right)} \tag{4.45}$$

$$ICE_{NO_3^-} = \frac{4C_{[FC]^B{}_{SS}}}{\left(\frac{2k_3^{eff}}{[Cl^-]} + 2k_4^{eff} + 4C_{[FC]^A{}_{SS}} k_6^{eff}\right)\left(1 + \frac{3k_{14}}{4k_{15}} + \frac{k_{13}[COD]}{4k_{15}[NH_4^+]}\right)} \quad (4.46)$$

$$ICE_{ClO_3^-} = \frac{6C_{[FC]^A{}_{SS}} k_6^{eff}}{\frac{2k_3^{eff}}{[Cl^-]} + 2k_4^{eff} + 4C_{[FC]^A{}_{SS}} k_6^{eff}} \quad (4.47)$$

4.6. REFERENCES

(1) Vorosmarty, C. J.; McIntyre, P. B.; Gessner, M. O.; Dudgeon, D.; Prusevich, A.; Green, P.; Glidden, S.; Bunn, S. E.; Sullivan, C. A.; Liermann, C. R.; Davies, P. M. Global threats to human water security and river biodiversity. *Nature* **2010,** *467* (7315), 555-561.

(2) Grant, S. B.; Saphores, J. D.; Feldman, D. L.; Hamilton, A. J.; Fletcher, T. D.; Cook, P. L. M.; Stewardson, M.; Sanders, B. F.; Levin, L. A.; Ambrose, R. F.; Deletic, A.; Brown, R.; Jiang, S. C.; Rosso, D.; Cooper, W. J.; Marusic, I. Taking the "Waste" out of "Wastewater" for human water security and ecosystem sustainability. *Science* **2012,** *337* (6095), 681-686.

(3) *Guidelines for water reuse*; EPA/600/R-12/618; United States Environmental Protection Agency: Washington, D.C., 2012.; nepis.epa.gov/Adobe/PDF/P100FS7K.pdf.

(4) Martinez-Huitle, C. A.; Ferro, S. Electrochemical oxidation of organic pollutants for the wastewater treatment: direct and indirect processes. *Chemical Society Reviews* **2006,** *35* (12), 1324-1340.

(5) Trasatti, S. Electrocatalysis in the anodic evolution of oxygen and chlorine. *Electrochimica Acta* **1984,** *29* (11), 1503-1512.

(6) Panizza, M.; Cerisola, G. Direct and mediated anodic oxidation of organic pollutants. *Chemical Reviews* **2009,** *109* (12), 6541-6569.

(7) Park, H.; Vecitis, C. D.; Hoffmann, M. R. Electrochemical water splitting coupled with organic compound oxidation: The role of active chlorine species. *Journal of Physical Chemistry C* **2009,** *113* (18), 7935-7945.

(8) Malpass, G. R. P.; Miwa, D. W.; Mortari, D. A.; Machado, S. A. S.; Motheo, A. J. Decolorisation of real textile waste using electrochemical techniques: Effect of the chloride concentration. *Water Research* **2007,** *41* (13), 2969-2977.

(9) Chiang, L. C.; Chang, J. E.; Wen, T. C. Indirect oxidation effect in electrochemical oxidation treatment of landfill leachate. *Water Research* **1995,** *29* (2), 671-678.

(10) Costa, C. R.; Olivi, P. Effect of chloride concentration on the electrochemical treatment of a synthetic tannery wastewater. *Electrochimica Acta* **2009,** *54* (7), 2046-2052.

(11) Malpass, G. R. P.; Miwa, D. W.; Machado, S. A. S.; Olivi, P.; Motheo, A. J. Oxidation of the pesticide atrazine at $DSA^{(R)}$ electrodes. *Journal of Hazardous Materials* **2006,** *137* (1), 565-572.

(12) Miwa, D. W.; Malpass, G. R. P.; Machado, S. A. S.; Motheo, A. J. Electrochemical degradation of carbaryl on oxide electrodes. *Water Research* **2006,** *40* (17), 3281-3289.

(13) Rajkumar, D.; Palanivelu, K. Electrochemical degradation of cresols for wastewater treatment. *Industrial & Engineering Chemistry Research* **2003,** *42* (9), 1833-1839.

(14) Rajkumar, D.; Kim, J. G. Oxidation of various reactive dyes with in situ electro-generated active chlorine for textile dyeing industry wastewater treatment. *Journal of Hazardous Materials* **2006,** *136* (2), 203-212.

(15) Park, H.; Vecitis, C. D.; Hoffmann, M. R. Solar-powered electrochemical oxidation of organic compounds coupled with the cathodic production of molecular hydrogen. *Journal of Physical Chemistry A* **2008,** *112* (33), 7616-7626.

(16) Choi, J.; Qu, Y.; Hoffmann, M. R. SnO_2, IrO_2, Ta_2O_5, Bi_2O_3, and TiO_2 nanoparticle anodes: electrochemical oxidation coupled with the cathodic reduction of water to yield molecular H_2. *Journal of Nanoparticle Research* **2012,** *14* (8).

(17) Valero, D.; Ortiz, J. M.; Exposito, E.; Montiel, V.; Aldaz, A. Electrochemical wastewater treatment directly powered by photovoltaic panels: Electrooxidation of a dye-containing wastewater. *Environmental Science & Technology* **2010,** *44* (13), 5182-5187.

(18) Park, H.; Bak, A.; Ahn, Y. Y.; Choi, J.; Hoffmannn, M. R. Photoelectrochemical performance of multi-layered BiO_x-TiO_2/Ti electrodes for degradation of phenol and production of molecular hydrogen in water. *Journal of Hazardous Materials* **2012,** *211*, 47-54.

(19) Park, H.; Choo, K.; Park, H.; Choi, J.; Hoffmann, M. R. Electrochemical oxidation and microfiltration of municipal wastewater with simultaneous hydrogen production: Influence of organic and particulate matter. *Chemical Engineering Journal* **2013,** *215-216* (15), 802-810.

(20) Walter, M. G.; Warren, E. L.; McKone, J. R.; Boettcher, S. W.; Mi, Q. X.; Santori, E. A.; Lewis, N. S. Solar water splitting cells. *Chemical Reviews* **2010,** *110* (11), 6446-6473.

(21) Panizza, M.; Cerisola, G. Electrochemical oxidation as a final treatment of synthetic tannery wastewater. *Environmental Science & Technology* **2004,** *38* (20), 5470-5475.

(22) Panizza, M.; Delucchi, M.; Cerisola, G. Electrochemical degradation of anionic surfactants. *Journal of Applied Electrochemistry* **2005,** *35* (4), 357-361.

(23) Comninellis, C. Electrocatalysis in the electrochemical conversion/combustion of organic pollutants for waste-water treatment. *Electrochimica Acta* **1994,** *39* (11-12), 1857-1862.

(24) Trasatti, S. Progress in the understanding of the mechanism of chlorine evolution at oxide electrodes. *Electrochimica Acta* **1987,** *32* (3), 369-382.

(25) Krishtalik, L. I. Kinetics and mechanism of anodic chlorine and oxygen rvolution reactions on yransition-metal oxide electrodes. *Electrochim Acta* **1981**, *26* (3), 329-337.

(26) Gujar, T. P.; Shinde, V. R.; Lokhande, C. D.; Han, S. H. Electrosynthesis of Bi_2O_3 thin films and their use in electrochemical supercapacitors. *Journal of Power Sources* **2006,** *161* (2), 1479-1485.

(27) Shuk, P.; Wiemhofer, H. D.; Guth, U.; Gopel, W.; Greenblatt, M. Oxide ion conducting solid electrolytes based on Bi_2O_3. *Solid State Ionics* **1996,** *89* (3-4), 179-196.

(28) Scialdone, O.; Randazzo, S.; Galia, A.; Silvestri, G. Electrochemical oxidation of organics in water: Role of operative parameters in the absence and in the presence of NaCl. *Water Research* **2009,** *43* (8), 2260-2272.

(29) Weres, O. Electrode with surface comprising oxides of titanium and bismuth and water purification process using this electrode. U.S. Patent 7,494,583 B2, Feb. 24, 2009.

(30) *Onsite wastewater treatment systems manual*; EPA/625/R-00/008; United States Environmental Protection Agency: Washington, D.C., 2002.; nepis.epa.gov/Adobe/ PDF/P100FS7K.pdf .

(31) Lowry, O. H.; Rosebrough, N. J.; Farr, A. L.; Randall, R. J. Protein measurement with the Folin phenol reagent. *Journal of Biological Chemistry* **1951,** *193* (1), 265-275.

(32) Dubois, M.; Gilles, K. A.; Hamilton, J. K.; Rebers, P. A.; Smith, F. Colorimetric method for determination of sugars and related substances. *Analytical Chemistry* **1956,** *28* (3), 350-356.

(33) Mohan, N.; Balasubramanian, N. In situ electrocatalytic oxidation of acid violet 12 dye effluent. *Journal of Hazardous Materials* **2006,** *136* (2), 239-243.

(34) Szpyrkowicz, L.; Kelsall, G. H.; Kaul, S. N.; De Favei, M. Performance of electrochemical reactor for treatment of tannery wastewaters. *Chemical Engineering Science* **2001,** *56* (4), 1579-1586.

(35) Wang, Y.; Wang, Y.; Meng, Y. L.; Ding, H. M.; Shan, Y. K.; Zhao, X.; Tang, X. Z. A highly efficient visible-light-activated photocatalyst based on bismuth- and sulfur-codoped TiO_2. *Journal of Physical Chemistry C* **2008,** *112* (17), 6620-6626.

(36) Goncalves, M. R.; Marques, I. P.; Correia, J. P. Electrochemical mineralization of anaerobically digested olive mill wastewater. *Water Research* **2012,** *46* (13), 4217-4225.

(37) Kesselman, J. M.; Weres, O.; Lewis, N. S.; Hoffmann, M. R. Electrochemical production of hydroxyl radical at polycrystalline Nb-doped TiO_2 electrodes and estimation of the partitioning between hydroxyl radical and direct Hole oxidation pathways. *Journal of Physical Chemistry B* **1997,** *101* (14), 2637-2643.

(38) Santana, M. H. P.; De Faria, L. A. Oxygen and chlorine evolution on RuO_2+TiO_2+CeO_2+Nb_2O_5 mixed oxide electrodes. *Electrochimica Acta* **2006,** *51* (17), 3578-3585.

(39) Panizza, M.; Cerisola, G. Olive mill wastewater treatment by anodic oxidation with parallel plate electrodes. *Water Research* **2006,** *40* (6), 1179-1184.

(40) Jung, Y. J.; Baek, K. W.; Oh, B. S.; Kang, J. W. An investigation of the formation of chlorate and perchlorate during electrolysis using Pt/Ti electrodes: The effects of pH and reactive oxygen species and the results of kinetic studies. *Water Research* **2010,** *44* (18), 5345-5355.

(41) Polcaro, A. M.; Vacca, A.; Mascia, M.; Palmas, S.; Ruiz, J. R. Electrochemical treatment of waters with BDD anodes: kinetics of the reactions involving chlorides. *Journal of Applied Electrochemistry* **2009,** *39* (11), 2083-2092.

(42) Czarnetzki, L. R.; Janssen, L. J. J. Formation of hypochlorite, chlorate and oxygen during NaCl electrolysis from alkaline-solutions at an RuO_2/TiO_2 Anode. *Journal of Applied Electrochemistry* **1992,** *22* (4), 315-324.

(43) Bergmann, M. E. H.; Rollin, J.; Iourtchouk, T. The occurrence of perchlorate during drinking water electrolysis using BDD anodes. *Electrochimica Acta* **2009,** *54* (7), 2102-2107.

(44) Kraft, A.; Stadelmann, M.; Blaschke, M.; Kreysig, D.; Sandt, B.; Schroder, F.; Rennau, J. Electrochemical water disinfection - Part I: Hypochlorite production from very dilute chloride solutions. *Journal of Applied Electrochemistry* **1999,** *29* (7), 861-868.

(45) Szpyrkowicz, L.; Radaelli, M.; Daniele, S. Electrocatalysis of chlorine evolution on different materials and its influence on the performance of an electrochemical reactor for indirect oxidation of pollutants. *Catalysis Today* **2005,** *100* (3-4), 425-429.

(46) Szpyrkowicz, L.; Kaul, S. N.; Neti, R. N.; Satyanarayan, S. Influence of anode material on electrochemical oxidation for the treatment of tannery wastewater. *Water Research* **2005,** *39* (8), 1601-1613.

(47) Szpyrkowicz, L.; Kaul, S. N.; Neti, R. N. Tannery wastewater treatment by electro-oxidation coupled with a biological process. *Journal of Applied Electrochemistry* **2005,** *35* (4), 381-390.

(48) Blatchley, E. R.; Cheng, M. M. Reaction mechanism for vhlorination of urea. *Environmental Science & Technology* **2010,** *44* (22), 8529-8534.

(49) Kapalka, A.; Katsaounis, A.; Michels, N. L.; Leonidova, A.; Souentie, S.; Comninellis, C.; Udert, K. M. Ammonia oxidation to nitrogen mediated by electrogenerated active chlorine on Ti/PtO_x-IrO_2. *Electrochemistry Communications* **2010,** *12* (9), 1203-1205.

(50) Peez, G.; Saiz, J.; Ibanez, R.; Urtiaga, A. M.; Ortiz, I. Assessment of the formation of inorganic oxidation by-products during the electrocatalytic treatment of ammonium from landfill leachates. *Water Research* **2012,** *46* (8), 2579-2590.

(51) Fernandes, A.; Pacheco, M. J.; Ciriaco, L.; Lopes, A. Anodic oxidation of a biologically treated leachate on a boron-doped diamond anode. *Journal of Hazardous Materials* **2012,** *199*, 82-87.

(52) Deborde, M.; von Gunten, U. Reactions of chlorine with inorganic and organic compounds during water treatment - Kinetics and mechanisms: A critical review. *Water Research* **2008,** *42* (1-2), 13-51.

(53) Vlyssides, A.; Barampouti, E. M.; Mai, S.; Arapoglou, D.; Kotronarou, A. Degradation of methylparathion in aqueous solution by electrochemical oxidation. *Environmental Science & Technology* **2004,** *38* (22), 6125-6131.

(54) Canizares, P.; Paz, R.; Lobato, J.; Saez, C.; Rodrigo, M. A. Electrochemical treatment of the effluent of a fine chemical manufacturing plant. *Journal of Hazardous Materials* **2006,** *138* (1), 173-181.

(55) Lei, X. H.; Maekawa, T. Electrochemical treatment of anaerobic digestion effluent using a Ti/Pt-IrO_2 electrode. *Bioresource Technology* **2007,** *98* (18), 3521-3525.

(56) Bonfatti, F.; Ferro, S.; Lavezzo, F.; Malacarne, M.; Lodi, G.; De Battisti, A. Electrochemical incineration of glucose as a model organic substrate - II. Role of active chlorine mediation. *Journal of the Electrochemical Society* **2000,** *147* (2), 592-596.

(57) Mohan, N.; Balasubramanian, N.; Basha, C. A. Electrochemical oxidation of textile wastewater and its reuse. *Journal of Hazardous Materials* **2007,** *147* (1-2), 644-651.

(58) *Energy demands on water resources: Report to congress on the interdependency of energy and water*; United States Department of Energy: Washington D.C., 2006.;

http://www.sandia.gov/energy-water/docs/121-RptToCongress-EWwEIAcomments-FINAL.pdf.

(59) Li, M.; Feng, C. P.; Zhang, Z. Y.; Shen, Z. L.; Sugiura, N. Electrochemical reduction of nitrate using various anodes and a Cu/Zn cathode. *Electrochemistry Communications* **2009,** *11* (10), 1853-1856.

(60) Kim, B. R. Effect of ammonia on COD analysis. *Journal Water Pollution Control Federation* **1989,** *61* (5), 614-617.

Chapter 5

$BI_XTI_{1-X}O_Z$ FUNCTIONALIZED HETERO-JUNCTION ANODE WITH AN ENHANCED REACTIVE CHLORINE GENERATION EFFICIENCY IN DILUTE AQUEOUS SOLUTIONS

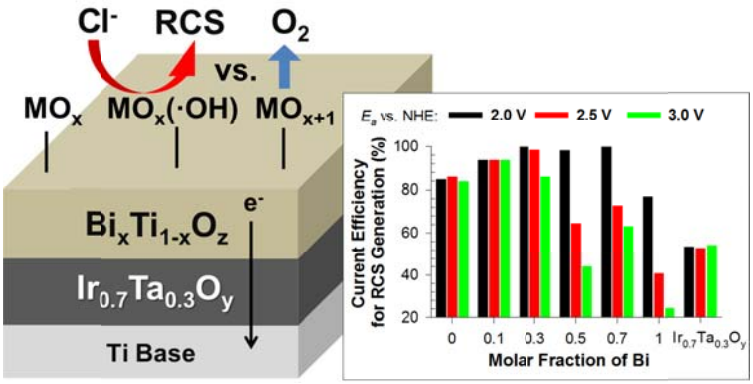

ABSTRACT

New $Ir_{0.7}Ta_{0.3}O_y/Bi_xTi_{1-x}O_z$ hetero-junction anodes have been developed and characterized for reactive chlorine species (RCS) generation in dilute aqueous solution (50 mM NaCl). The primary objective was to control the electro-stationary speciation of hydrous metal oxides between hydroxyl radical ($>MO_x(\cdot OH)$) and higher valence-state oxides ($>MO_{x+1}$). An underlying layer of the mixed-metal oxide, $Ir_{0.7}Ti_{0.3}O_y$, was synthesized to serve as a primary ohmic contact and electron shuttle. Binary thin films of $Bi_xTi_{1-x}O_z$ were prepared from the thermal decomposition of an aqueous solution mixture of Ti/Bi complexes. With these core components, the measured current efficiency for RCS generation (η_{RCS}) was enhanced where the values observed for x = 0.1 or 0.3 were virtually twice of the η_{RCS} of the $Ir_{0.7}Ti_{0.3}O_y$ anode. At the same time, the rates of RCS generation were enhanced by a factor of 20 – 30%. Partial substitution of Ti with Bi results in a positive shift in surface charge allowing for stronger interaction with anions as confirmed by FTIR-ATR analysis. A kinetic model to describe the formate ion degradation showed that an increasing fraction of Bi in the composite promotes a redox transition of $>MO_x(\cdot OH)$ to $>MO_{x+1}$. In accelerated life tests under conditions corresponding to a service life of 2 years under an operational current density of 300 A m^{-2}, dissociation of Ti component from $Ir_{0.7}Ta_{0.3}O_y/TiO_2$ was found to be minimal, while BiO_x in the surface layers undergoes oxidation and a subsequent dissolution.

5.1. INTRODUCTION

We developed new hetero-junction mixed-metal oxides anodes, which allow for enhanced reactive chlorine generation in dilute aqueous solution in terms of current (energy) efficiency. The outer surface of the hetero-junction anodes is functionalized with $Bi_xTi_{1-x}O_z$ layers which provide elevated electro-stationary concentration of adsorbed hydroxyl radical, while the underlying $Ir_{0.7}Ta_{0.3}O_y$ layer serves both as ohmic contact and electron shuttle. This study demonstrates that the surficial binary metal oxides layers, prepared through traditional thermal decomposition of aqueous Ti and Bi complex solutions, not only shift the heterogeneous kinetics and selectivity but also reduce a loss of the precious element (*e.g.*, Iridium) under long-term operation.

Dimensionally stable anodes (DSAs) consisting of mixed-metal oxides containing either IrO_2 or RuO_2 as core components have been widely deployed for industrial chlorine production (chloro-alkali processes),[1] energy storage into molecular H_2 (polymer exchange membrane electrolysis),[2,3] and high-salinity wastewater treatment processes,[4,5] among many other uses. Drawbacks to long-term application include the high materials cost of Ir and Ru as well as their instability relative to conversion to IrO_4^{2-} and RuO_4 under operational anodic potential bias.[6] In recent years, strategies to promote the mass normalized activities of IrO_2 or RuO_2 have relied on increasing electro-active surface area via either quantum sizing the crystalline structure[3,7] or elevation in thin film porosity[1,2] by modern material preparation techniques. The use of mixed-metal oxides anodes has been extended to composites containing Ta_2O_5,[6] TiO_2,[6,8-10] SnO_2,[11,12] ZrO_2,[6] CeO_2,[8,9] and Sb_2O_5[11,12] as a secondary or tertiary component, most often focusing on enhancement in

stability or conductivity. Nevertheless, for a couple of decades, IrO_2-Ta_2O_5 (Ir:Ta = 7:3) and RuO_2-TiO_2 (Ru:Ti = 3:7) combinations remain the best composition accepted for an industrial application with respect to oxygen evolution reaction (OER) and chlorine evolution reaction (ClER), respectively.[1,2,6]

Another challenge to point out in this regard is that the Pt-group metal oxides with the lowest over-potential for OER also exhibit outstanding electro-catalytic activities for chlorine generation. The competition between OER and ClER is due to their competition for active surface sites (*e.g.*, surface coordinated reactive oxygen species).[13] Upon an electrical potential gradient across the anode/electrolyte interface, hydrous metal oxides have been known to produce physi-sorbed hydroxyl radicals ($>MO_x(\cdot OH)$) and, by further oxidative transition, higher oxides ($>MO_{x+1}$).[4,5,14] As a rule of thumb, the surface-bound $>MO_x(\cdot OH)$ is believed to prefer reactions with electron-donating substances adsorbed on the surface, whereas liberation of active oxygen chemi-sorbed to a higher-oxidation-state central metal into molecular O_2 would be favored for $>MO_{x+1}$.[14] The quasi-stationary distribution between $>MO_x(\cdot OH)$ and $>MO_{x+1}$ is primarily determined by the enthalpy change in lower ($>MO_x$) to higher ($>MO_{x+1}$) oxides transition or the binding energy of active oxygen.[13,15,16] In this context, volcano plots have been used to interpret the electrochemical activities of variable types of metal oxide.[15] Recent density functional theory calculations suggested that the volcano type relations for OER and ClER overlap while the highest activity is seen with RuO_2 followed by IrO_2.[13,16]

The additives are often used to control the electrolyte composition (*i.e.*, the activities of chloride ion, water, and proton) and to minimize various scavenging reactions.[17] The

selectivity toward a desired product is also contingent upon the speciation of surficial reactive oxygen species which, in turn, is mostly determined by the specific composition of the anode.[4,5] Relatively low metal-oxygen bond strengths for PbO_2, SnO_2, and TiO_2 are known to facilitate reactions between $>MO_x(\cdot OH)$ and electron donating substrates (*e.g.*, organics and chloride ion). As a result, metal oxides located at the left-hand side of a typical volcano plot show considerably high current efficiencies (selectivities of electron transfer), in spite of a large kinetic barrier (and energy consumption) for initial activation of $>MO_x$. On the contrary, $>MO_x(\cdot OH)$ sites are readily quenched by redox transition of metal ions in case of IrO_2- or RuO_2-based mixed metal oxides with relatively low OER over-potentials. Therefore, the degradation of organic waste products on metal oxides near the apex of the volcano plot is primarily due to homogeneous reactions with reactive chlorine species (RCS) that are generated from $>MO_{x+1}$. In this case, the current generation from OER is often comparable or dominating that from ClER in dilute aqueous solutions.

Among several beneficial aspects of hetero-junction fabrication of catalytic thin film, a shift in heterogeneous kinetics can be anticipated by surface modification[18] to enhance the selectivity towards the reaction of interest. TiO_2 in water lead to the formation of surface-bound hydroxyl radical, $>Ti(\cdot OH)$, by trapping photo-chemically generated electrons and holes under illumination or with an applied potential bias equal to or greater than the bandgap energy.[19] TiO_2 provides active sites for hydroxyl radical formation with limited transition to $>MO_{x+1}$.[20] On the other hand, Bi_2O_3 is known to have excellent pseudo-capacitance capability in the water splitting potential region and dielectric permittivity for use in Faradaic supercapacitors.[21,22] Extraordinary oxide ion conductivity

attributed to intrinsic disordered oxygen vacancies and high polarizability by the presence of a $6s^2$ lone pair in Bi(III) allows Bi_2O_3 to be used as a solid oxide fuel cell electrolyte.[23] The electrochemical nature of Bi_2O_3 appears to be suitable for $>MO_x$ formation and OER.[24]

In this paper, we report on the electrochemical activity and stability of $Ir_{0.7}Ti_{0.3}O_y/Bi_xTi_{1-x}O_z$ hetero-junction anodes and their potential applications for electrochemical water and wastewater treatment. A systematic parametric study was undertaken in order to determine the effects of nominal molar fraction of Bi in $Bi_xTi_{1-x}O_z$ functionalities on RCS generation efficacies during the course of potentiostatic electrolysis of dilute aqueous solutions with circum-neutral pH.

5.2. EXPERIMENTAL SECTION

5.2.1. $Ir_{0.7}Ti_{0.3}O_y/Bi_xTi_{1-x}O_z$ Hetero-junction Anode Preparation. The hetero-junction semiconductor anodes were prepared by sequential thermal decomposition methods. Ti metal sheets (3 × 2 cm^2, 0.5 mm thickness) were pretreated by sand-blast, 50 V/V% acetone degreasing, and etching in boiling 10 M/V% oxalic acid right before fabrication. $Ir_{0.7}Ta_{0.3}O_y$ layers were prepared by brushing precursor (70 mM H_2IrCl_6 + 30 mM $TaCl_5$ in 1:1 ethanol and isopropanol) on both sides of Ti base, drying at 80 ºC (10 min) and annealing at 525 ºC (10 min). The electrodes underwent five more repetitive sequences and further heat treatment at 525 ºC for 1 h as a final annealing, ending up with catalysts loading of 0.64 mg cm^{-2} on average. Aqueous titanium-glycolate complex was prepared from hydroxo-peroxo method,[25-27] with proper modifications. In a typical recipe, titanium butoxide (250 mM of final concentration) and glycolic acid (375 mM) were added into a

relevant amount of water. The resulting precipitates were re-dissolved with 30 W/W% H_2O_2 (*ca.* 40% of final precursor volume). Exothermic reactions with a presence of dark red color appeared with vigorous generations of CO_2 and O_2 bubbles. In order to adjust the pH to be circum-neutral, a small aliquot of concentrated NH_4OH (*ca.* 3.5% of final precursor volume) was added. The color quickly changed into yellow with the pH adjustment while mild bubble generations (including N_2) continued with a decay of residual H_2O_2. Aqueous Bi solutions were prepared by dissolving 250 mM bismuth citrate in 750 mM NH_4OH solutions. The resulting precursors of Ti and Bi were mixed together for preparation of $Bi_xTi_{1-x}O_z$ layers with variable nominal molar fraction of Bi (x = 0, 0.1, 0.3, 0.5, 0.7, 1). Analogous thermal decomposition procedures were carried out on top of the $Ir_{0.7}Ta_{0.3}O_y$ anode with annealing temperature at 425 ºC. The mass loading of outer $Bi_xTi_{1-x}O_z$ layer ranged from 0.51 to 1.4 mg cm^{-2}, depending on the precursor composition (x). The prepared electrodes were cleaned with dilute acetone and a large amount of deionized water before electro-analytical and physic-chemical characterization.

5.2.2. Electroanalysis. The electrochemical reactor employed throughout this study consisted of an anode under investigation, a stainless steel cathode in parallel (3 × 2 cm^2, 5 mm distance), and a Ag/AgCl/Sat. KCl reference electrode (Basi Inc.) in a one compartment cell (working volume of 60 mL). The Vycor® glass tip of the reference electrode was located 3 mm apart from the center of the anode. Applied anodic potential (E_a) from a potentiostat (SP-50, BioLogic) was converted to the normal hydrogen electrode (NHE) scale by E_a (NHE) = E_a (Ag/AgCl) + 0.197 V. Cyclic voltammetry (CV) data in stirred 50 mM NaCl solutions (three consecutive cycles without open-circuit resting) were recorded in the range of E_a from 0.2 to 1.0 V at the scan rate of 20 mV sec^{-1}.

The quasi-stationary polarization data from 0.8 to 2.5 V were also collected with the scan rate of 5 mV sec^{-1}. Before each electrochemical experiment, open circuit potentials of anode and cathode were monitored for 30 min. The ohmic resistances were measured before and after each experiment by a current interruption method with current bias of 200 mA.

5.2.3. Potentiostatic RCS Generation and Formate Ion Degradation. The generation rate and current efficiency of RCS generation were estimated during potentiostatic electrolysis in 50 mM NaCl solutions under several different E_a (2.0, 2.5, and 3.0 V). The RCS concentration was measured by DPD (N,N-diethyl-p-phenylenediamine) reagent at a fixed time interval (2 min) three times with proper dilutions. The relatively low reaction time was intended to minimize an occurrence of chlorine species with higher oxidation states (ClO_3^-, ClO_4^-).[28] The current efficiency for the RCS generation was estimated by the following equation:

$$\eta_{\mathrm{RCS}} = \frac{2\,VF\,d[Cl_{DPD}]}{I\,dt} \tag{5.1}$$

where, V is electrolyte volume (0.06 L), F is Faraday constant (96485.3 C mol^{-1}), $[Cl_{DPD}]$ is the concentration of RCS (M), I is current (A), and t is electrolysis time (sec). In order to assess the contribution of $>MO_x(\cdot OH)$ on the RCS generation, formate ion was chosen as a probe compound for the surficial hydroxyl radical. Potentiostatic electrolysis experiments were performed in 50 mM NaCOOH solutions for 1 h. The $[HCOO^-]$ was measured for periodically collected samples using ion chromatography (Dionex, USA) with anion-exchange column (Ionpac AS 19).

5.2.4. Surface Characterization. After finishing the electrochemical experiments, anodes were cut into half pieces, each of which was subject to the physicochemical surface analysis and accelerated life test, respectively. The horizontal or cross-sectional morphology were observed by ZEISS 1550VP field emission scanning electron microscopy (SEM), while elemental compositions were analyzed by Oxford X-Max SDD X-ray energy dispersive spectrometer (EDS) system either in point-and-identification or mapping mode. X-ray diffraction (XRD) profiles were collected using an X'pert MD (Panalytical) diffractometer with Cu-K radiation. Thermo-Scientific Nicolet™ iS™50 Fourier transform infrared spectroscopy (FTIR) was used to characterize surface functionalities. Hetero-junction anodes were held on attenuated total reflectance (ATR) unit in contact either with deionized water or 1 M $NaClO_4$ solutions.

5.2.5. Accelerated Life Test. The stabilities of the $Ir_{0.7}Ta_{0.3}O_y/Bi_xTi_{1-x}O_z$ hetero-junction anodes with variable molar fraction of Bi (x) were compared using accelerated life tests. Each hetero-junction anode sandwiched with a stainless steel cathode (0.5 × 2 cm^2, 3 mm distance) was immersed in 1 M $NaClO_4$ solution in a conical tube. Neware Battery Testing System powered the galvanostatic (current density= 1 A cm^{-2}) electrolysis in each test cell. The electrolyte was replaced periodically (3 to 5 h interval), and dissociated amounts of Ti, Bi and Ir in the electrolyte were quantified by Agilent inductivity coupled plasma-mass spectrometry (ICP-MS).

5.3. RESULTS

5.3.1. Physico-chemical Properties. Figure 5.1 shows SEM images of the $Ir_{0.7}Ta_{0.3}O_y/Bi_xTi_{1-x}O_z$ hetero-junction anodes with variable molar fraction of Bi (x) after

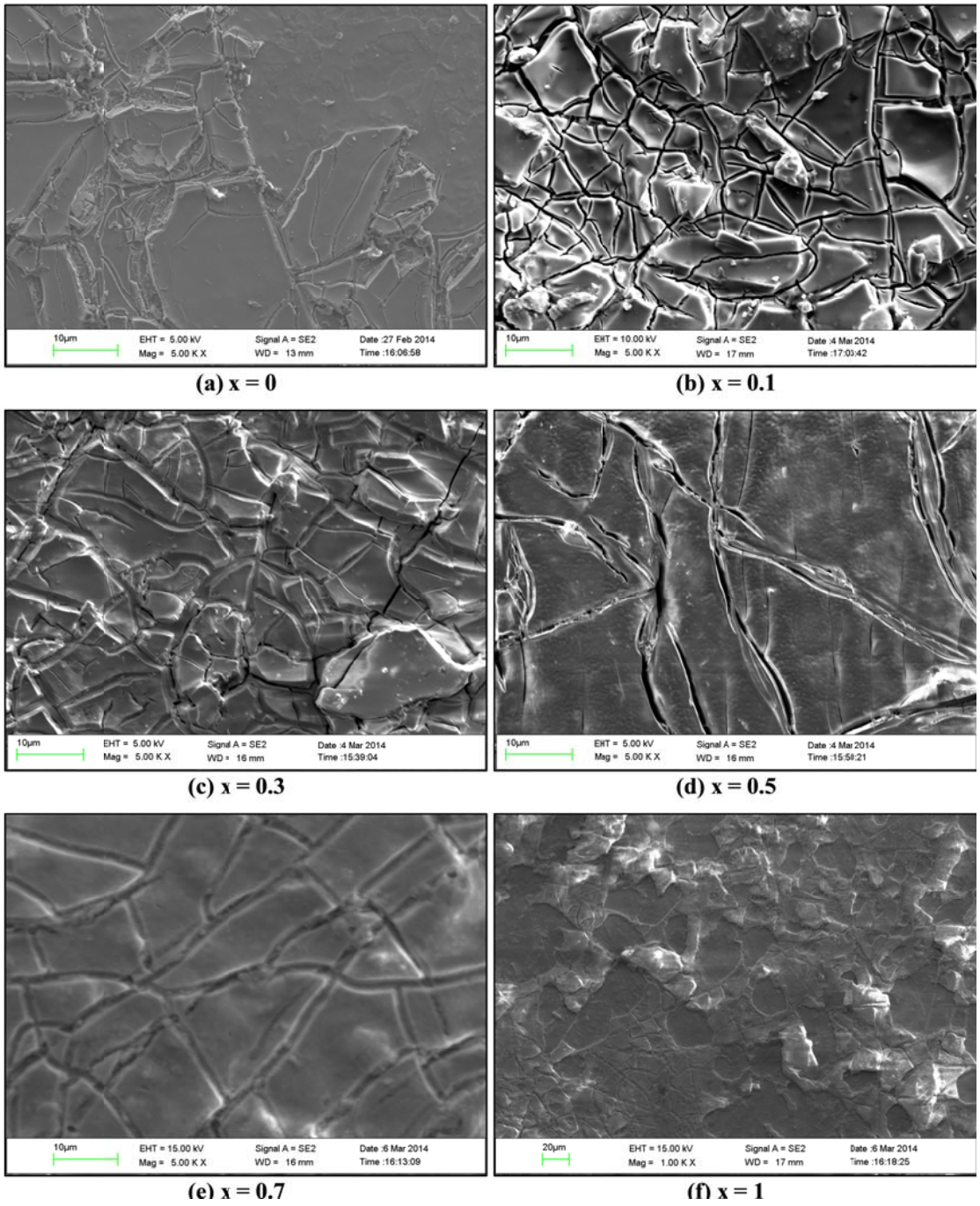

Figure 5.1. Scanning Electron Microscopy (SEM) images of horizontal view for $Ir_{0.7}Ta_{0.3}O_y/Bi_xTi_{1-x}O_z$ hetero-junction anode with variable molar fraction of Bi with magnification of ×5000 (a – e) or ×1000 (f).

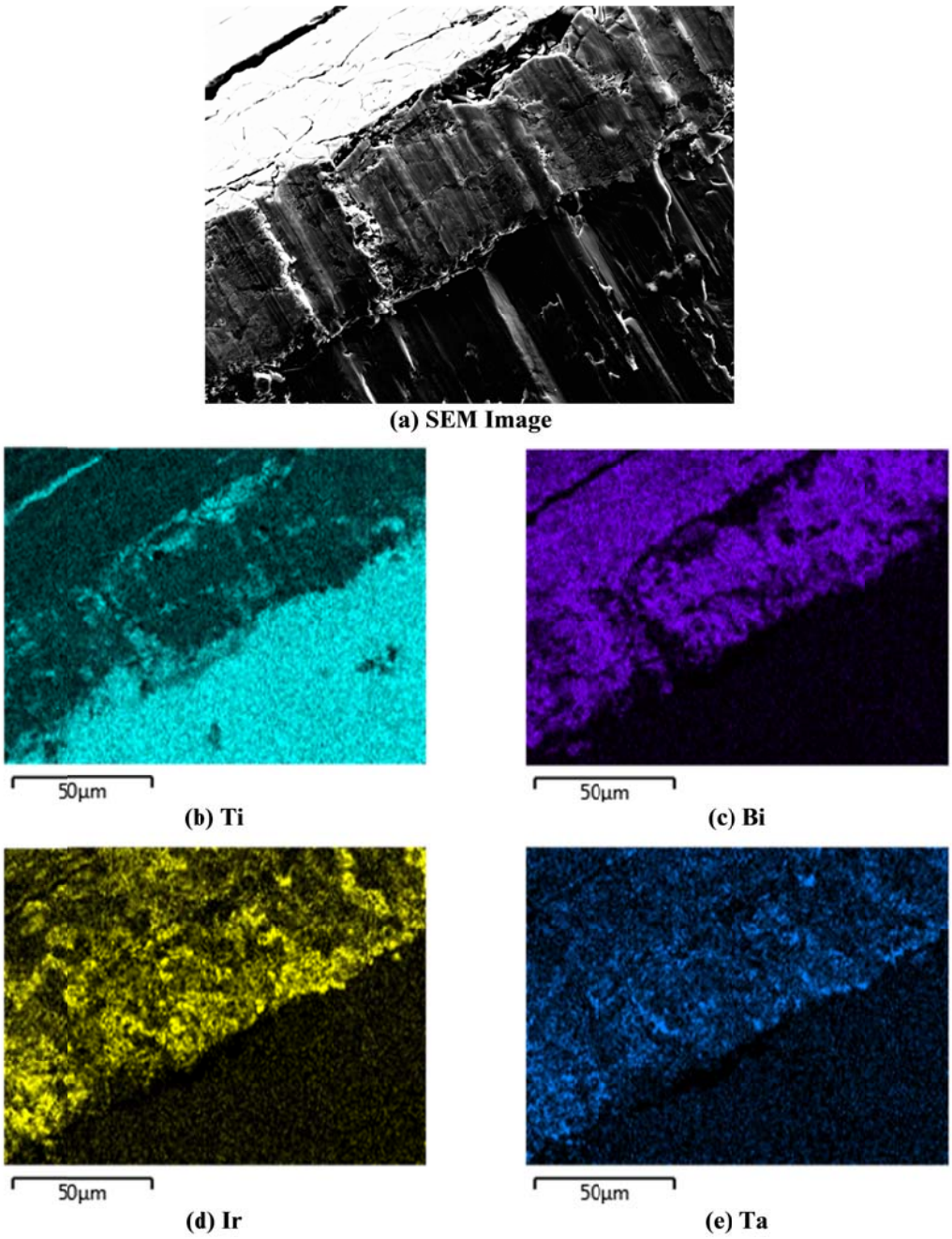

Figure 5.2. Scanning Electron Microscopy (SEM) image (a) of cross-section view for $Ir_{0.7}Ta_{0.3}O_y$ /$Bi_{0.3}Ti_{0.7}O_z$ hetero-junction anode with Energy Dispersive Spectroscopy (EDS) mapping of Ti (b), Bi (c), Ir (d), and Ta (e).

undergoing the electrochemical experiments. The horizontal morphology of the outer surface appeared to have a cracked and fragmented shapes, where the size of discrete islands appeared to be the lowest for x = 0.1. Observations of vertical cross-section estimated the total depth of mixed metal oxides deposit on Ti support to be approximately 70 μm, while suggested that the depth of cracks is much less than the total film thickness. The surficial cracks were more distinct for the binary compositions (x = 0.1 ~ 0.7), which presumably ascribed to the differences in thermal expansion coefficients of titanium and bismuth oxides.[10] The interface between the underlying $Ir_{0.7}Ta_{0.3}O_y$ and $Bi_xTi_{1-x}O_z$ was not distinct perhaps due to inter-diffusions of ions. An EDS mapping image on a cross-section view of $Ir_{0.7}Ta_{0.3}O_y/Bi_{0.3}Ti_{0.7}O_z$ anode (Figure 5.2) indicated, in fact, that thermal inter-diffusion of the metal ions had taken place across the hetero-junction during annealing, on the basis of vertical gradients of Ir and Ta signals.

According to the XRD profiles (Figure 5.3), the hetero-junction anode without Bi doping (x = 0) was characterized by a mixture of anatase and rutile phase TiO_2. In the presence of Bi with fractions higher than 10%, the peak from the anatase TiO_2 ($2\theta = 25$ º) disappeared. The anatase TiO_2 structure has been known to be transformed into a thermodynamically more stable rutile structure by thermal stresses with temperatures higher than 600 ºC.[29] However, evidence has been presented that an existence of impurities in the TiO_2 lattice structure can significantly reduce the transition temperature;[1] the annealing temperature in this study was 425 ºC, which is in the lower range reported by Hanaor and Sorrell[29]. In addition, Tomita *et al*.[25] reported the crystalline structure of TiO_2 prepared from the aqueous titanium-glycolate complexes can

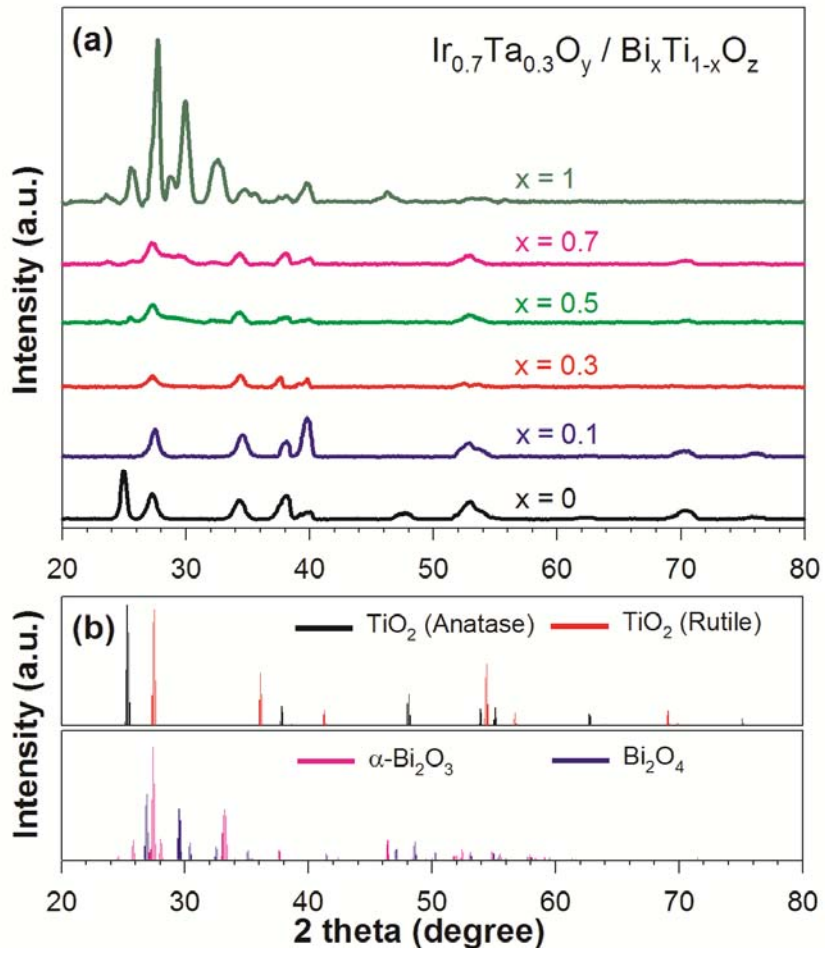

Figure 5.3. X-ray diffraction patterns of hetero-junction anodes $Ir_{0.7}Ta_{0.3}O_y$ / $Bi_xTi_{1-x}O_z$ with variable molar fraction (x) of Bi (a) referenced with a library for metal oxides of interests (b).

be influenced by the pH of precursor solution. With the current formulation for preparation of the anodes, the process of mixing with the Bi precursor (bismuth citrate dissolved in ammonia) should elevate the mixture precursor pH. In the absence of Ti ($Ir_{0.7}Ta_{0.3}O_y/BiO_z$), the surficial XRD patterns indicate α-phase Bi_2O_3 and Bi_2O_4, suggesting that the effective oxidation state of Bi is a mixture of +3 and +5. In this regard, it is well known that monoclinic α-Bi_2O_3 is converted to cubic δ-Bi_2O_3 at temperatures

higher than 730 ºC. After cooling the product, metastable β- and γ-phase Bi_2O_3 are found.[23] A visual observation, that the light yellow color of the initial composite as deposited changed into white after the electrochemical experiments, implied that the partial oxidation of Bi (III) to Bi (V) was likely to occur via an anodic potential bias rather than via thermal annealing. For the hetero-junction anodes with Bi fraction from 0.3 to 0.7, the diffraction intensities appeared to be much lower than the other compositional formulations using the same XRD instrument. The relative differences in the effective ionic radii of Bi (103 pm) and Ti (60.5 pm) may result in distortions in the lattice microstructure, which is often observed in binary metal oxide thin film.[30]

The infrared absorption bands of the hetero-junction anodes in contact with deionized water (Figure 5.4a) were mostly characterized by broad bands at 3000 – 3600 cm^{-1}, relatively sharp peaks centered at 1640 cm^{-1}, and prominent bands starting at around 900 cm^{-1}. Peaks at 1640 cm^{-1} are usually assigned to bending (deformation) vibrations of free or physi-sorbed water, while the absorption bands ranged from 3000 to 3600 cm^{-1} are ascribed to stretching vibrations of surface titanol group (>Ti-OH) or hydrogen bonded H_2O. Absorption regions at wavenumbers lower than 900 cm^{-1} occur owing to fundamental vibrations of oxides lattice, particularly from M-O stretching and M-O-M bridging modes (where M is Ti or Bi). The minor peaks at around 2400 cm^{-1} are attributed to adsorption of carbonaceous species from air. Regarding the Bi-enriched hetero-junction anodes (x = 0.7 and 1), peaks centered near 1400 cm^{-1} appeared due to hydrated bismuth oxide moieties or surface hydroxyl functionalities (*i.e.*, >Bi-OH) via hydrolysis as in the common case of metal oxides exposed to water (*e.g.*, TiO_2, Fe_2O_3, SiO_2, WO_3, etc.). The absorption peaks near 3300 cm^{-1} broadened as the fraction of Bi

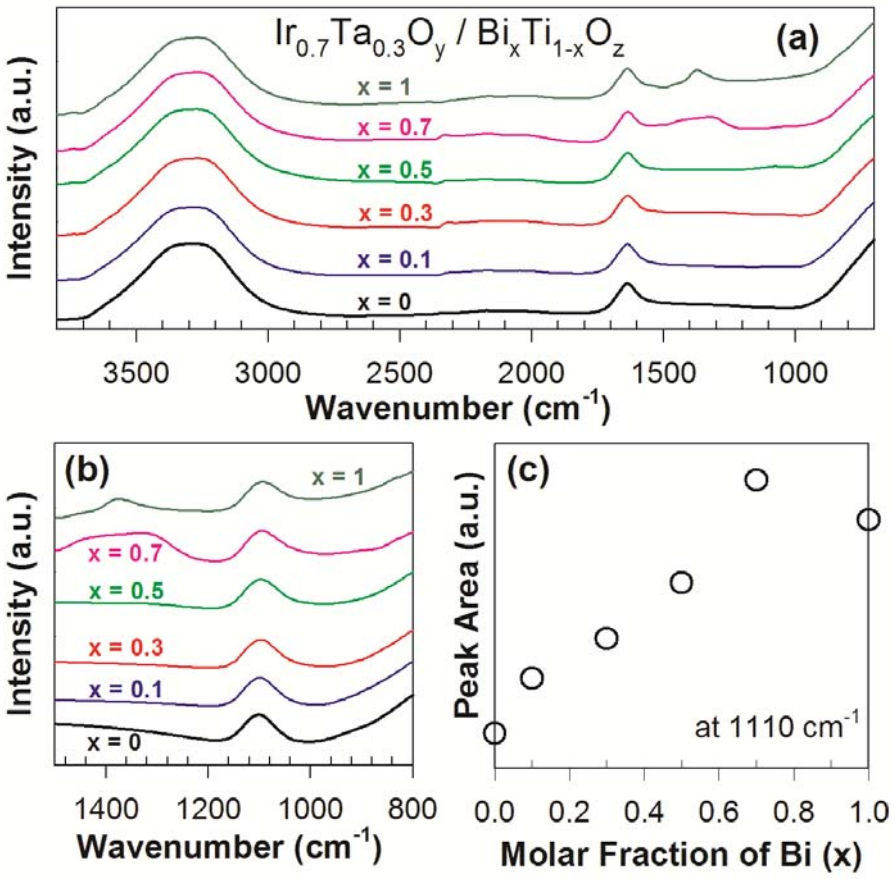

Figure 5.4. Fourier transform infrared spectroscopy with attenuated total reflectance (FTIR-ATR) analysis of $Ir_{0.73}Ta_{0.27}O_y/Bi_xTi_{1-x}O_z$ hetero-junction anodes with variable molar fraction (x); (a) in contact with deionized water, (b) in contact with 1 M $NaClO_4$ solutions, (c) integrated intensities of peaks at 1110 cm^{-1} in contact with 1 M $NaClO_4$ solutions. Each adsorption spectra was collected with respect to the background signal of the contacting liquid.

increased. In contrast, the intensity of the peak at 1640 cm^{-1} did not change along with the molar fraction of Bi, presumably due to the interference of interstitial water molecule layers between solid samples and internal reflectance element. Evidence has been presented that the absorption bands in this range (1640 cm^{-1}) originate primarily from coordinated H_2O rather than from surficial hydroxyl group.[31]

According to traditional models describing the surface charge of metal oxides based on their amphoteric nature, the IR absorption from M-OH bonds is expected to decay with the deprotonation of OH functionalities. Therefore, increased isoelectric point of metal oxides at a given solution composition (bulk pH) would allow for losses in absorption by M-OH. In an attempt to assess the role of Bi on the surface charge more clearly, IR spectra were collected in 1 M $NaClO_4$ background solutions with circum-neutral pH. Aside from the absorption profiles described above, characteristic peaks of adsorbed ClO_4^- appeared at 1110 cm^{-1} (Figure 5.4b). The integrated intensities of the characteristic peaks monotonically increased along with the molar fraction of Bi (Figure 5.4c). This observation clearly demonstrates that an increase in the surficial Bi fraction is accompanied by an increase in positive surface charges.

5.3.2. Voltammetric Characteristics. Water oxidation on metal oxide anodes is initiated by the one electron oxidation of surface hydroxyl groups to form bound hydroxyl radical ($>MO_x(\cdot OH)$) and, sequentially, these intermediate states can be further oxidized to higher oxides ($>MO_x$).[4,5,14] Eqs 5.2-5.5 describe the overall reaction sequence of the OER,[17,32,33] where the rate constant for each reaction step is governed by the bond strength between the corresponding metal ion and active oxygen.[15,16]

$$>MO_x + H_2O \rightarrow >MO_x(\cdot OH) + H^+ + e^- \ (k_1) \quad (5.2)$$

$$>MO_x(\cdot OH) \rightarrow >MO_x + 1/2\ O_2 + H^+ + e^- \ (k_2) \quad (5.3)$$

$$>MO_x(\cdot OH) \rightarrow >MO_{x+1} + H^+ + e^- \ (k_3) \quad (5.4)$$

$$>MO_{x+1} \rightarrow >MO_x + 1/2\ O_2 \ (k_4) \quad (5.5)$$

Figure 5.5a illustrates the electrochemical activities of the $Ir_{0.7}Ta_{0.3}O_y/Bi_xTi_{1-x}O_z$ hetero-junction anodes in 50 mM NaCl solutions with circum-neutral pH in terms of current density (J) during anodic polarization. The anodic wave followed a quasi-linear relation with the applied potential; *i.e.*, an exponential dependence given by the Butler-Volmer formulation was relaxed due to an increase in ohmic resistance. The onset potential for the anodic current, which is defined as the iR-corrected anodic potential ($E_a - iR$) at the J of 1 A m^{-2},[34] was observed at near 1.2 V on average without a significant variation with composition (coefficient of variation: 5 %). The corresponding over-potential of OER was 0.4 V, which is comparable to previously reported values for anodes based on IrO_2.[7,33] The Tafel slopes, from the linear regions of log J versus $E_a - iR$ relationships, appeared to be near 120 mV $decade^{-1}$ in the range of $E_a - iR$ lower than 1.55 V. These values were not dependent on the surface composition as well (coefficient of variation: 7%). Under a larger anodic bias, there were substantial increases in the Tafel slopes most likely due to mass transport limitations. The observed Tafel slopes can be interpreted in terms of the initial formation of hydroxyl radical (eq 5.2) as the rate-determining step.[15,17,32]

In the absence of the $Ir_{0.7}Ta_{0.3}O_y$ layer, the current generation was always negligible, as shown in Figure 5.5a ($Bi_{0.3}Ti_{0.7}O_z$ as an example). Even with the presumed redox transitions of surficial Bi, the $Ir_{0.7}Ta_{0.3}O_y$ layer was essential as an ohmic contact to overcome the Schottky barrier to electron transfer (metal oxides toward base metals). The magnitudes of J on the hetero-junction anodes were lower than on the $Ir_{0.7}Ta_{0.3}O_y$ anode, owing to the electrical resistance across the hetero-junction. In addition, the intensity of

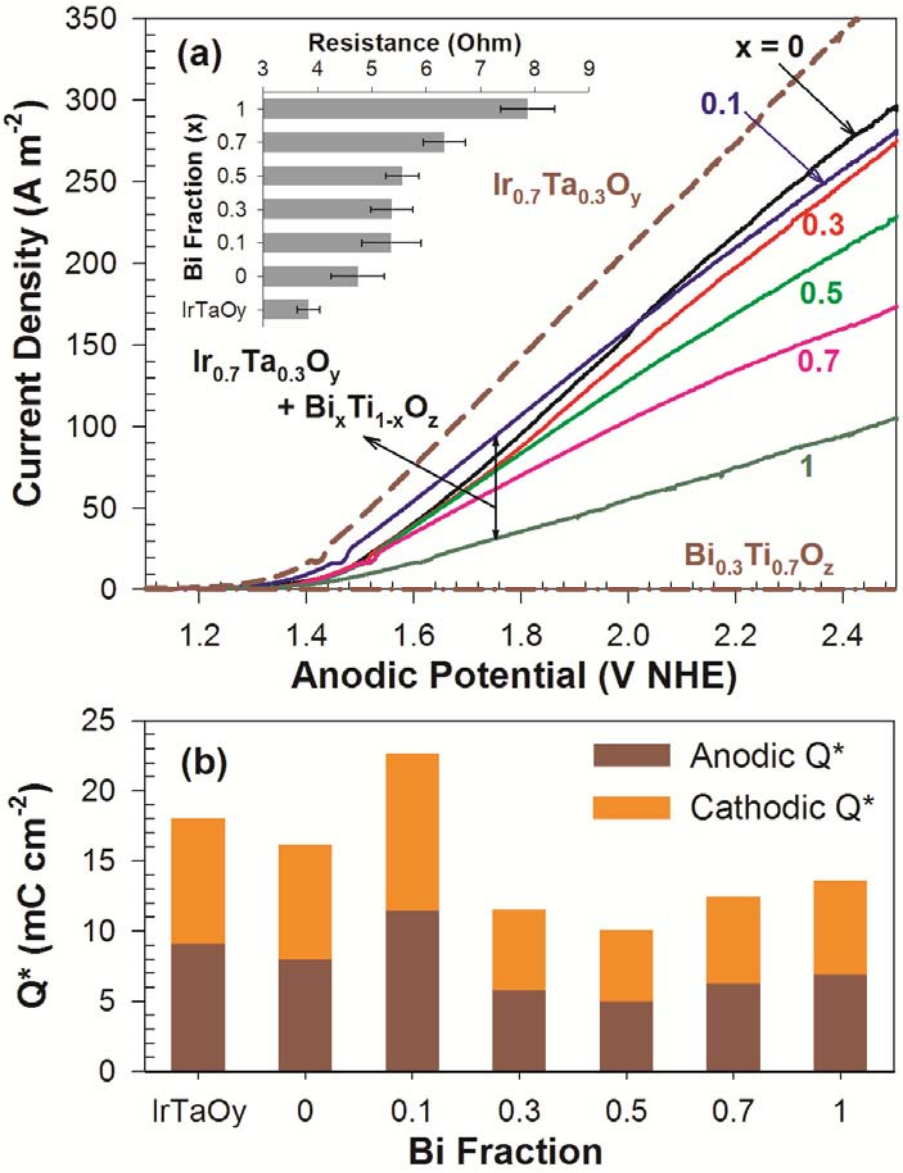

Figure 5.5. (a) Current generation during linear sweep voltammetry (scan rate: 5 mV sec^{-1}) together with (a, inset) ohmic resistance measured by current interruption and (b) integrated charge (Q*) during cyclic voltammetry (scan range: 0.2 ~ 1.0 V NHE, scan rate: 20 mV sec^{-1}) with $Ir_{0.73}Ta_{0.27}O_y/Bi_xTi_{1-x}O_z$ hetero-junction anodes with variable molar fraction (x); electrolyte: 50 mM NaCl (pH ~ 7), cathode: stainless steel, geometric surface area: 3×2 cm^2. Data for $Ir_{0.7}Ta_{0.3}O_y$ or $Bi_{0.3}Ti_{0.7}O_z$ anode are shown as references.

the anodic wave decreased as the molar fraction of Bi increased. In light of nearly consistent onset potentials and Tafel slopes, the effects of Bi content on current generation can be explained in terms of the ohmic resistance measured by a current interruption technique (inset of Figure 5.5a). The ohmic resistance consists of electrolyte resistance to ion migration, polarization resistance coupled with resistance across the catalytic film.[35] Their combined effects can be depicted as resistors in series for a simplified equivalent (*e.g.*, Randles circuit).[10,32,36-38] Because double layer capacitances usually overwhelm the physical capacitances of metal oxides films by several orders of magnitude,[37] the polarization resistance would not significantly contribute to the ohmic resistances in measurements by the current interruption method.[35] Therefore, the adverse effects of the Bi content on current response are ascribed to an increasing electrical resistance within the anode. This observation is therefore analogous to p-n junction under reverse bias, since the Bi_2O_3 has often been regarded as a p-type semiconductor.[39]

On the other hand, integrated charge (Q*) in a cyclic voltammogram within the potential region between the hydrogen evolution reaction and OER has been widely used as a parameter for electrochemically active surface area.[8,10,36] Figure 5.6 shows the CV profiles in 50 mM NaCl solutions under E_a between 0.2 and 1.0 V. The integrated charges in anodic current (anodic Q*) was superimposable to those in cathodic current (cathodic Q*), as depicted in Figure 5.5b. The reversible redox reactions (described either by eq 5.2 or eq 5.4) at the active sites should account for the symmetric voltammograms.[8] The ratio of Ti to Bi contents was not well correlated with the magnitude of Q*, which was observed to be the highest for the Bi fraction of 0.1. In addition, there was little

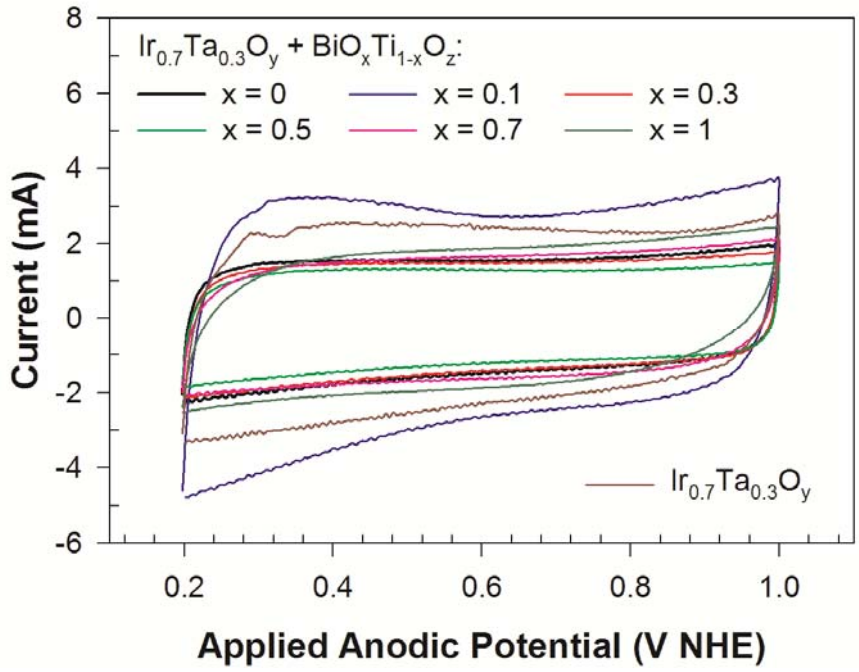

Figure 5.6. Cyclic voltammogram of $Ir_{0.7}Ta_{0.3}O_y/Bi_xTi_{1-x}O_z$ hetero-junction anode with variable molar fraction of Bi (x) referenced with $Ir_{0.7}Ta_{0.3}O_y$ anode; counter electrode: stainless steel, geometric surface area: 3×2 cm^2, electrolyte: 50 mM NaCl, scan range: 0.2 – 1.0 V NHE, scan rate: 20 mV sec^{-1}.

relationship between the current density and Q*, which suggests that the current generation is primarily governed by ohmic resistance rather than by the surface area.

5.3.3. Reactive Chlorine Species Generation. Figure 5.7 shows reactive chlorine generation on $Ir_{0.7}Ta_{0.3}O_y/Bi_xTi_{1-x}O_z$ hetero-junction anodes in 50 mM NaCl solutions. The E_a was adjusted from 2.0 to 3.0 V, which corresponded to the cell voltage from 4 to 6 V versus the counter electrode. The current generation during the course of potentiostatic electrolysis (Figure 5.7a) was in general agreement with the polarization curve in Figure 5.5a. In comparison with the $Ir_{0.7}Ta_{0.3}O_y$ anode, the quasi-steady-state values of J were reduced for the hetero-junction anodes by 20 to 60% as the molar

fraction of Bi increased, primarily due to augmented *iR* (*vide supra*). Nevertheless, the $Bi_xTi_{1-x}O_z$ hetero-junction layer was found to substantially increase the current efficiency of RCS generation as calculated using eq 5.1 (Figure 5.7c). The η_{RCS} was estimated to average 53% for $Ir_{0.7}Ta_{0.3}O_y$ anode, in agreement with previous reports under comparable condition.[28] This value increased to 85% via the layering of an protective overcoat of TiO_2 (x = 0). Even higher magnitudes of η_{RCS} were observed for the hetero-junction anodes with Bi contents of 10 or 30%. Consequently, the rates of RCS generation (Figure 5.7b) were enhanced by a factor of 20 to 30%. The improvements in η_{RCS} should be underscored because the energy efficiency, in terms of the specific RCS generation rate normalized by power input, is directly proportional to the η_{RCS} (and cell voltage).

The electrochemical oxidation of chloride ion on metal oxides anodes occurs due to reactions with either hydroxyl radical or active oxygen adsorbed on the surface, as described by the following equations:[5,13,40]

$$>MO_x(\cdot OH) + Cl^- \rightarrow >MO_x + 1/2Cl_2 + OH^- \ (k_5 = 4.3 \times 10^9\ M^{-1}\ s^{-1}) \qquad (5.6)$$

$$>MO_{x+1} + Cl^- \rightarrow >MO_x + ClO^- \ (k_6) \qquad (5.7)$$

Outer-sphere electron transfer from chloride ion (eq 5.6) is most likely much faster than by direct transfer of active surficial oxygen (eq 5.7). In this regard, the η_{RCS} is likely to be determined primarily by speciation between $>MO_x(\cdot OH)$ and $>MO_{x+1}$. The relative concentration of surface reactive oxygen will depend on the rate of eq 5.4, whose electro-stationary distribution can be described in terms of a 'Nernstian' equilibrium. The

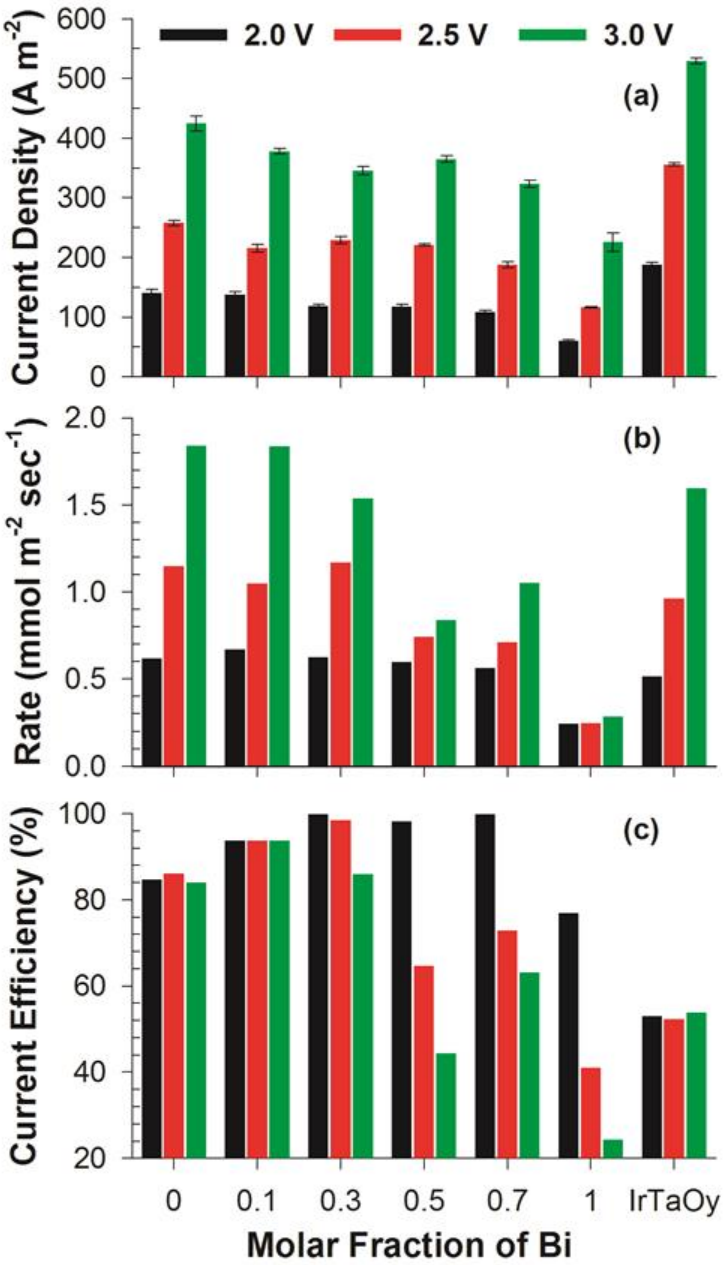

Figure 5.7. (a) Mean current density together with (b) specific rate and (c) current efficiency of reactive chlorine species generation during the course of potentiostatic electrolysis with $Ir_{0.7}Ta_{0.3}O_y/Bi_xTi_{1-x}O_z$ hetero-junction anodes with variable molar fraction (x); electrolyte: 50 mM NaCl (pH ~ 7), cathode: stainless steel, geometric surface area: 3×2 cm^2, applied anodic potential: 2.0, 2.5, 3.0 V NHE. Data for $Ir_{0.7}Ta_{0.3}O_y$ anode are shown as references.

increase in η_{RCS} on $Bi_xTi_{1-x}O_z$ hetero-junction system can be explained as the lower to higher oxide transition via electron transfer is more thermodynamically favorable (*i.e.*, lower enthalpy change) to IrO_2 rather than to TiO_2.

When Bi is the majority surface constituent (x = 0.5 to 1), the η_{RCS} decreased with increasing anodic potential. The decrease of η_{RCS} could be possibly explained in association with bulk pH. Electrolysis in dilute NaCl solutions results in an increase of pH from non-stoichiometric water splitting.[41] The increase of solution pH that is proportional to the conversion of chloride ion to RCS favors the OER since higher pH reduces the redox potential of water oxidation. In some cases, however, the Bi may accelerate the higher oxide formation[24] with a net result of increasing rate with increasing anodic potential.

5.3.4. Formate Ion Degradation. Formate ion was used in this study as a prove for surface-bound hydroxyl radical.[20] Many investigators employ reactive dye compounds such as methylene blue and RNO (p-nitrosodimethylaniline) for quantitative ·OH estimation with relatively simple instrumentation.[14,42] However, the low aqueous solubility of these dye compounds limits the operational concentration (< 1 mM). Furthermore, degradation of a dye compound via a direct electron transfer or active oxygen transfer from higher oxides has been reported for IrO_2-based anodes.[42] The reaction between formate ion and ·OH produces the carbon dioxide radical anions (eq 5.8 and 5.9) and the homogeneous bimolecular rate constants for this sequence are well known.[43] We assume that oxygen atom transfer from $>MO_{x+1}$ to formate is very slow in

comparison. For example, the O-atom transfer between ozone and formate ion was reported to be in the range of 10^2 M^{-1} s^{-1}.[43]

$$>MO_x(\cdot OH) + HCOO^- \rightarrow >MO_x + COO^{-}\cdot + H_2O \ (k_7 = 3.2 \times 10^9\ M^{-1}\ s^{-1}) \quad (5.8)$$

$$>MO_x(\cdot OH) + COO^{-}\cdot \rightarrow >MO_x + CO_2 + OH^- \quad (5.9)$$

$$[>MO_x(\cdot OH)]_{SS} = \frac{k^{obs}{}_{formate}\ (s^{-1})}{3.2 \times 10^9\ M^{-1}s^{-1}} \quad (5.10)$$

The formate ion degradation in 50 mM NaCOOH solutions (Figure 5.8) followed pseudo-first-order reaction profile that in turn allows for a steady-state kinetic analysis. The quasi-steady-state concentration of hydroxyl radical on each anode surface ($[>MO_x(\cdot OH)]_{SS}$) was estimated according to the observed pseudo-first-order rate constant of formate decay ($k^{obs}{}_{formate}$), using eq 5.10, given the homogeneous bimolecular rate constant. The estimated concentration of $>MO_x(\cdot OH)$ (Figure 5.9) was orders of magnitude lower than the typical site density of >Ti-OH moieties on TiO_2 particles (1×10^{-8} mol cm^{-2}), but in comparable order with estimations for thin film TiO_2 electrodes.[41]

The rates of formate degradation rate under variable surface composition (Figure 5.9) were largely in parallel with those of RCS generation; both the $k^{obs}{}_{formate}$ and $[>MO_x(\cdot OH)]_{SS}$ showed peaks at x of 0.1 or 0.3 and monotonically decreased with further increases of the Bi content. This observation could also result from a combinational consequences of ohmic resistance (*vide supra*) and branching ratio of $>MO_x(\cdot OH)$ to $>MO_{x+1}$. However, in comparison with the hetero-junction anodes giving the highest rate

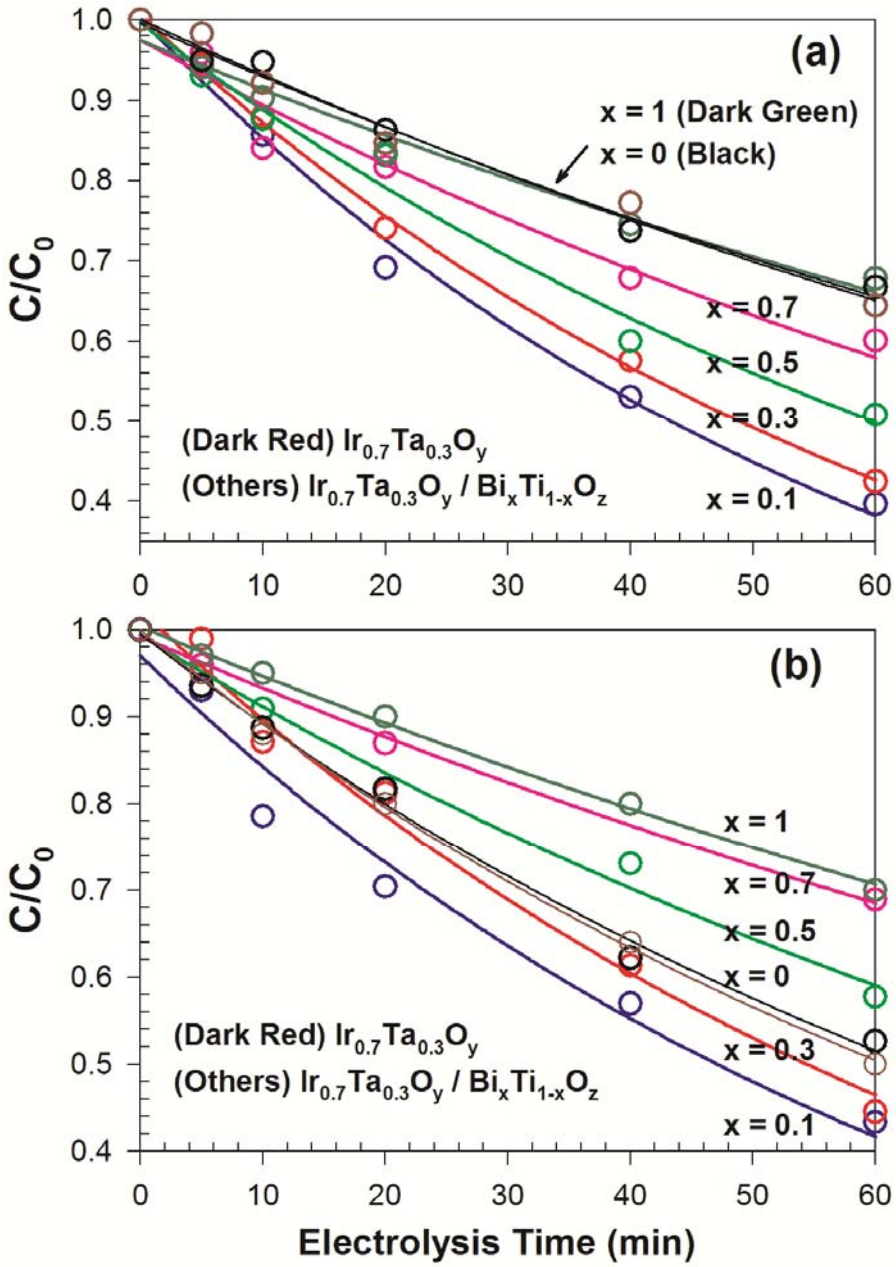

Figure 5.8. Time profiles of formate ion oxidation during the course of potentiostatic electrolysis with $Ir_{0.7}Ta_{0.3}O_y/Bi_xTi_{1-x}O_z$ hetero-junction anodes with variable molar fraction (x); electrolyte: 50 mM NaCOOH, cathode: stainless steel, geometric surface area: 3×2 cm^2, applied anodic potential: (a) 2.5 and (b) 3.0 V NHE. Data for $Ir_{0.7}Ta_{0.3}O_y$ anode are shown as references.

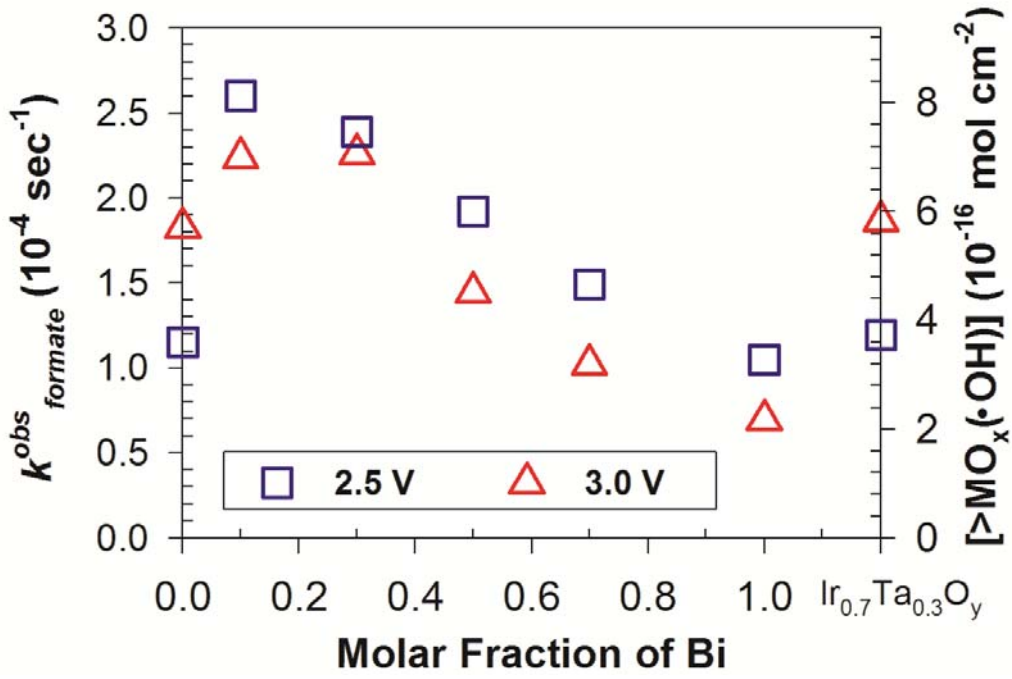

Figure 5.9. Observed pseudo-first-order rate constant of formate ion oxidation with corresponding surface hydroxyl radical concentration during the course of potentiostatic electrolysis with $Ir_{0.7}Ta_{0.3}O_y/Bi_xTi_{1-x}O_z$ hetero-junction anodes with variable molar fraction (x); electrolyte: 50 mM NaCOOH, cathode: stainless steel, geometric surface area: 3×2 cm^2, applied anodic potential: 2.5 or 3.0 V NHE. Data for $Ir_{0.7}Ta_{0.3}O_y$ anode are shown as references.

constants (x = 0.1 or 0.3), the anodes without Bi ($Ir_{0.7}Ta_{0.3}O_y$ with or without TiO_2 hetero-junction) resulted in slower reactions with $HCOO^-$ (particularly at the E_a of 2.5 V). Recalling that the anodes without Bi showed comparable RCS generation rates with the hetero-junction anodes with x of 0.1 or 0.3, contributions of lattice oxygen atoms to RCS generation appear to be more significant for anodes without Bi. On the other hand, when Bi fraction exceeds 0.1, the $[>MO_x(\cdot OH)]_{SS}$ at the E_a of 3.0 V was found to be even lower than those at 2.5 V.

5.3.5. Stability. The accelerated life tests are the most widely used protocols to estimate the service life of anodes for OER or ClER. In these methods, the goal is usually to monitor the cell voltage under a harsh galvanostatic environment (J up to 1 A cm^{-2}) such that the dissolution or detachment of electro-active catalysts occurs more rapidly. An accelerated life, as determined by the point when an abrupt jump of cell voltage occurs along with complete deactivation, can be converted into an estimated service life under practical operating conditions according to empirical proportionalities to $J^{1/m}$ (m range from 1.4 to 2.0).[11] However, in the case of the hetero-junction anodes, removal of the outer $Bi_xTi_{1-x}O_z$ layer would not deteriorate the voltammetric response from the $Ir_{0.7}Ta_{0.3}O_y$ layer. In this regard, the definition of accelerated life was modified to an endpoint in which the free metal concentration in the background electrolyte would signify complete failure of $Bi_xTi_{1-x}O_z$ layer. Passivation of the base metal by insulating TiO_2[11] was assumed to be insignificant when compared to dissolution or detachment of the catalytic films.

Figure 5.10 shows the variations of cell voltage and cumulative metal concentrations in the electrolyte (1 M $NaClO_4$ solutions) during the course of galvanostatic electrolysis. The electrolyte solution was maintained to have near circum-neutral pH. During the life test, the cell voltage ranged from 4.0 to 5.5 V (Figure 5.10a) without a noticeable failure for 48 h of electrolysis. The impact of an increasing ohmic resistance for higher Bi levels was not obvious because of fluctuations in cell voltage that were associated with vigorous bubble generation and changes in electrode area exposed to solutions. The dissociation of the $Bi_xTi_{1-x}O_z$ layer is likely to be via dissolution rather than detachment since macro-

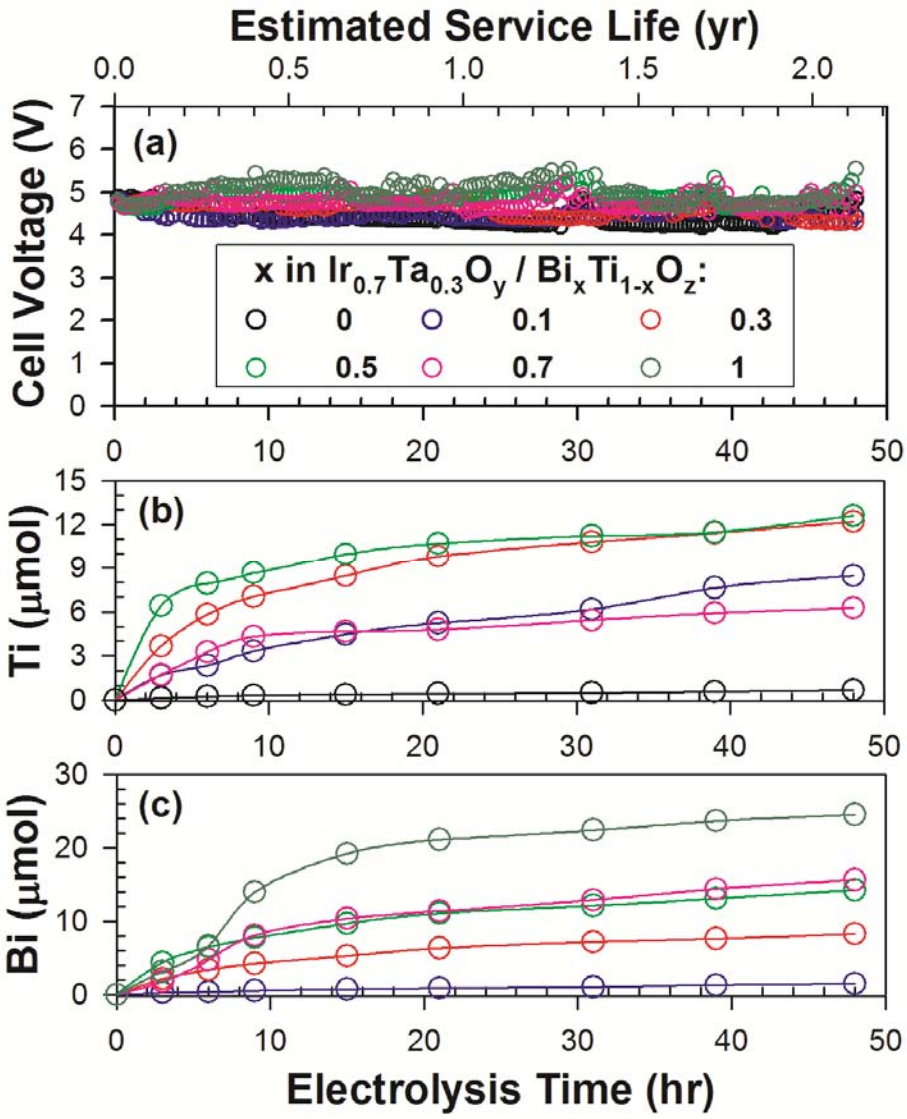

Figure 5.10. Variations of cell voltage (a) together with cumulative molar amounts of dissociated Ti (b) and Bi (c) during the course of galvanostatic electrolysis with $Ir_{0.7}Ta_{0.3}O_y/Bi_xTi_{1-x}O_z$ hetero-junction anodes with variable molar fraction (x); electrolyte: 1 M $NaClO_4$ (pH ~ 7), cathode: stainless steel, geometric surface area: 2×0.5 cm^2, current density: 1 A cm^{-2}. Estimated service life under operating current density of 300 A m^{-2} is shown in a parallel axis with electrolysis time (h) with proportionality to current density$^{1/1.7}$.

particles did not exist in visual observations of the electrolyte. The cumulative amounts of dissolved Bi (Figure 5.10c) increased faster with augmenting Bi content, which indicates that Bi components mitigate the stability of the $Bi_xTi_{1-x}O_z$ layer. According to the Pourbaix diagram of Bi,[44] the vicinal acidity produced by water discharge should be responsible for the dissolution of Bi_2O_3 to Bi(III) ions (Bi^{3+}, $BiOH^{2+}$, BiO^+), whereas higher oxides of Bi (Bi_4O_7, Bi_2O_4, and Bi_2O_5) are expected to require more acidic pH for dissolution. Destruction of the Ti lattice appeared to accompany the dissolution of Bi, as illustrated by the cumulative Ti concentration in Figure 5.10b. The highest amount of Ti released into the solution was observed for an anode with an equi-molar ratio of Ti to Bi ($x = 0.5$).

5.4. DISCUSSION

From an analogy with Hume-Rothery rules, Bi_2O_3 was not expected to constitute a homogeneous solid solution within the TiO_2 lattice, because of substantial differences in lattice structure (tetragonal for rutile TiO_2[19] and monoclinic for α-phase Bi_2O_3[23,45]) and effective radius of metal ions. In addition, the XRD intensity profiles of $Ir_{0.7}Ta_{0.3}O_y/Bi_xTi_{1-x}O_z$ anodes showed insignificant variations with respect to the fraction of Bi. Therefore, the microstructure of the outer layer is likely to be a mixed phase oxide crystal with a limited miscibility.[6,38] Given this assumption, the physico-chemical characteristics of the $Bi_xTi_{1-x}O_z$ layer should locally conform to the properties of TiO_2 and Bi_2O_3 individually for which the overall characteristics would depend on the molar mixing ratio. For example, the instability of Bi under (water discharge induced) acidic condition agrees with the phase transformation given by Pourbaix diagram of Bi_2O_3.[44]

The electrochemically active surface areas estimated by Q* were found to be primarily determined by physical surface area. As shown in Figure 5.11, the Q* of the anodes under investigation (Figure 5.5b) followed fairly well an inverse relationship with the physical lattice dimensions estimated by the XRD peaks in Figure 5.3 and the Scherrer equation. Regardless of the type of metal ions, the hydrous metal oxides can serve as electrochemically active sites as long as proper electron shuttles are electrically accessible.[30] This correlation in spite of the variation in surface composition indicates that the $Ir_{0.7}Ta_{0.3}O_y$ layer is the acting electron carrier in this potential window (0.2 to 1.0 V).[8,10] The half potentials of the symmetric voltamograms in Figure 5.6 were close to the redox potential of the Ir_2O_3/IrO_2 couple (E = 0.51 V, at pH 7). On a thermodynamic basis, the redox transitions of Ti_2O_3/TiO_2 (E = -0.47 V at pH 7) or Bi/Bi_2O_3 (E = -0.04 V at pH 7) are infeasible to drive the oxidation of surface hydroxyl group.

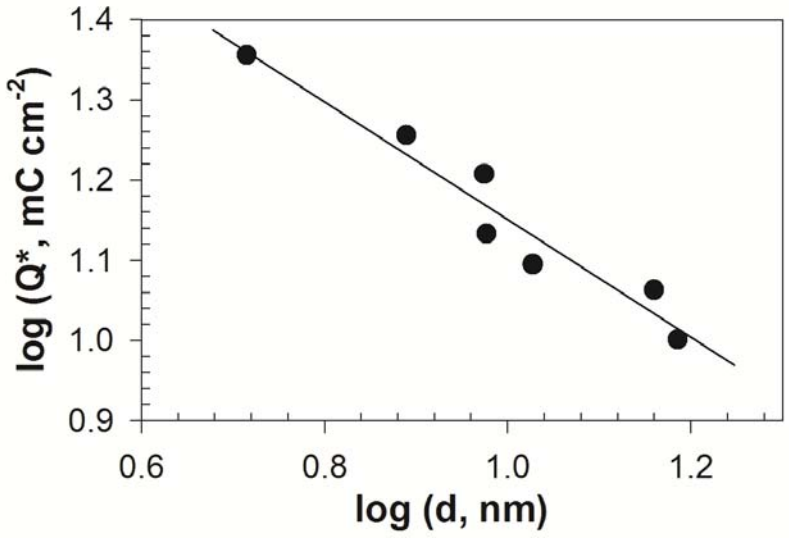

Figure 5.11. Relationship between Q* as a parameter of electrochemically active surface area and crystalline dimension estimated from XRD intensity by Scherer equation.

Moderate increases of η_{RCS} and $k^{obs}_{formate}$ with an increasing Bi fraction up to 0.3 should be primarily associated with the surface charge depending on the amphoteric properties of the metal oxides. The point of zero charge (pH_{pzc}) of Bi_2O_3 (9.4) is reported to be much greater than TiO_2 (5.1 – 6.4) or IrO_2 (3.3).[46] Thus, the surface of $Bi_xTi_{1-x}O_z$ layers should be more positively charged at higher Bi fraction, x. This change enhances the accumulation of anions (Cl^- and $HCOO^-$) in the electrical double layer. The magnitude of ClO_4^- adsorption in Figure 5.4c is consistent with this interpretation, given the monotonic increase in the characteristic IR peak area of ClO_4^- (at 1110 cm^{-1}) with the increase of x. In addition, Bi-doping increases the intensities of the Ti-OH bond under the molar fraction of Bi lower than 10%.[47,48] Alves *et al*.[9] also noted that substitution of TiO_2 with CeO_2 (pH_{pzc} ~ 8.1) increases the surface OH group concentration as measured by X-ray photoelectron spectroscopy. Stronger speciation of the -OH functionality towards protonated moieties, with corresponding IR signals either of >Ti-OH (3000 to 3600 cm^{-1}) or >Bi-OH (centered at 1400 cm^{-1}), would be beneficial to the hydroxyl radical formation. The electro-stationary [>MOx(·OH)] was estimated to be the highest for x of 0.1 or 0.3 (Figure 5.9), even though $[>MOx(\cdot OH)]_{SS}$ should implicitly include the partitioning constants of formate ion in our simple kinetic analysis.

Under a potential bias within the domain of water splitting, the $>MO_x(\cdot OH)$ site should be quenched by a redox transformation of transition metal (Ir or Bi) to produce $>MO_{x+1}$. Given several simplifying assumptions for the kinetics of formate degradation, the rate constants for eq 5.4 (k_3) could be estimated by rearrangement of the governing equation for $[>MO_{x+1}]$ under pseudo-steady-state conditions.

$$k_3 = \frac{k_4[>\mathrm{MO_{x+1}}]}{[>\mathrm{MO_x}(\cdot\mathrm{OH})]_{SS}} = \frac{\eta_{O_2} I}{2F} \times \frac{1}{A[>\mathrm{MO_x}(\cdot\mathrm{OH})]_{SS}} \quad (5.11)$$

where, η_{O2} is the current efficiency of OER and A is the geometric surface area of the electrode. The η_{O2} can be calculated from the charge balance equations. We also assume that $>MO_x(\cdot OH)$ and $>MO_{x+1}$ are exclusively responsible to $HCOO^-$ oxidation and OER, respectively; *i.e.*, eq 5.3 is relatively slow and productions of homogeneous reactive oxygen species (*e.g.*, H_2O_2, O_3, $O_2^{\cdot -}$) are negligible.

Figure 5.12 illustrates k_3 for $Ir_{0.7}Ta_{0.3}O_y/Bi_xTi_{1-x}O_z$ anodes which mostly increases together with the surficial Bi concentration. This finding suggests an oxidation of Bi(III) to Bi(IV) or Bi(V) can be an active electron sink for insertion of oxygen into the lattice. The behavior of Bi_2O_3 is analogous to that of electroactive IrO_2, since Zhang *et al.*[33] reported that an increasing Ir fraction in $Ir_xSi_{1-x}O_y$ anodes nonlinearly promotes the rate constant of higher oxide formation. The redox potential at pH 7 is 0.92 V for Bi_4O_7/Bi_2O_3 and 1.13 V for Bi_2O_4/Bi_4O_7 couple. The Bi(V) would reduce the kinetic barrier to oxide transition more effectively, as supported by the considerable increase of k_3 with E_a (2.5 V versus 3.0 V). On the contrary, in the absence of surficial Bi, the influence of E_a on k_3 value was not distinct, raising a possibility that dismutations of bound hydroxyl radical ($2>MO_x(\cdot OH) \rightarrow >MO_x + >MO_{x+1} + H_2O$)[8,17,49] might account for the higher oxides formation with Ir(IV)/Ir(VI) transition. The highest k_3 value was observed mostly for the $Ir_{0.7}Ta_{0.3}O_y$ layer, as expected by the redox potential of IrO_3/IrO_2 couple (0.94 V at pH 7) falling below that of Bi_2O_4/Bi_4O_7 couple. The kinetics of $>MO_x/>MO_{x+1}$ transition would

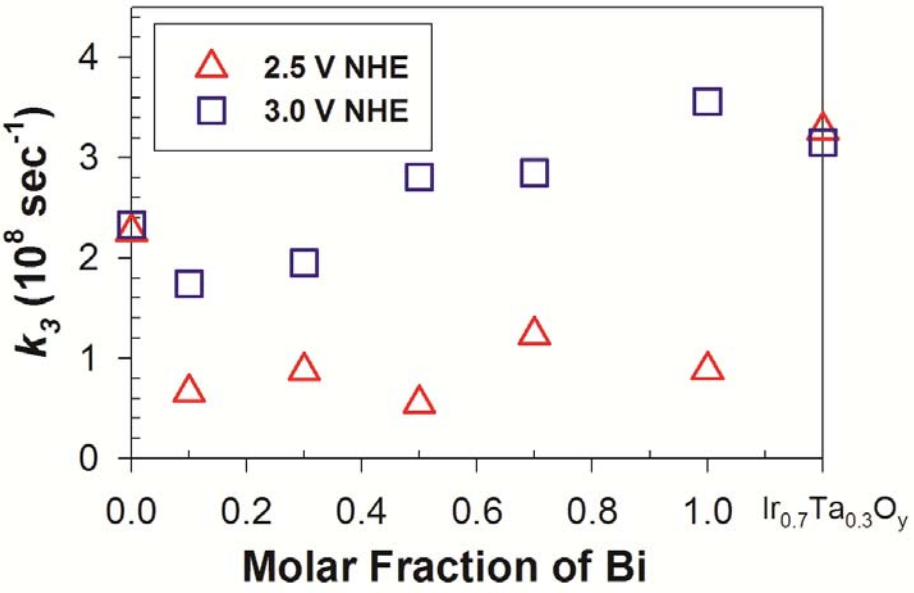

Figure 5.12. Estimated rate constant for transition from surface bound hydroxyl radical to higher oxide in 50 mM NaCOOH solutions.

also be influenced by concentrations of oxide ion vacancy in the lattice structure.[14] The magnitudes of k_3 estimated in this study (0.5 - 3.5 × 10^8 sec^{-1}) were in a similar order with $k_5[Cl^-]$ (2.2 × 10^8 sec^{-1}) or $k_7[HCOO^-]$ (1.6 × 10^8 sec^{-1}). The relative reaction rate of [>MO_x(·OH)] to form >MO_{x+1} in comparison with oxidizing electron donating substrates (Cl^- or $HCOO^-$) would be the primary determinant of the current efficiency, which was found to be affected by the surface compositions and E_a. The higher oxide formation driven by electro-active Bi would rationalize the behaviors of anodes with high Bi contents (x > 0.5); the decrease of η_{RCS} and $k^{obs}_{formate}$ along with x and E_a.

The dissociation of $Bi_xTi_{1-x}O_z$ layers would provoke a direct contact of the $Ir_{0.7}Ta_{0.3}O_y$ layer with the electrolyte and losses of Ir component, albeit the Ir concentrations in the electrolyte were always near the detection limit. Visual observation

of blackish deposits as well as EDS analysis confirmed precipitation of Ir, presumably in the form of $Ir(OH)_x$, on cathodes. Compared with the estimated total metal loading (*ca.* 25 μmol), the hetero-junction anodes with Bi fractions higher than 0.5 approached complete dissociation after 21 h of electrolysis. The corresponding service life was estimated to be *ca.* 1 year assuming operational current density and the factor of *m* to be 300 A m^{-2} and 1.7, respectively. For the other anodes with lower Bi concentrations (x = 0.1 and 0.3), the cumulative metal concentrations in the electrolyte did not reached their expected plateaus, indicating service lifes higher than 2 years. More importantly, the Ti concentration in electrolyte was negligible for $Ir_{0.7}Ta_{0.3}O_y/TiO_2$ anode throughout the experiments, demonstrating an outstanding stability in anodic environment. Even after the failure of the outer layer of the hetero-junction anodes, they can be regenerated with minimal cost by subsequent coating with oxide of earth-abundant and environmentally benign[19,45] Ti and Bi.

In conclusion, we demonstrated that surface modification of an $Ir_{0.7}Ta_{0.3}O_y$ anode with an over layer of $Bi_xTi_{1-x}O_z$ leads to an enhancement in current efficiency for reactive chlorine generation during the electrochemical oxidation of chloride ion. In particular, lower mole fractions of Bi in the surface layer (x = 0 – 0.3) yield higher current efficiency. Long-term operation can be achieved without the loss of Ir since the overlying $Bi_xTi_{1-x}O_z$ layer prevents the $Ir_{0.7}Ta_{0.3}O_y$ from direct contact with electrolyte, even though bismuth oxide is vulnerable to dissolution under anodic environment. Results of this study could lead to improvements in commercial electrochemical chlorine production or to advanced treatment of high-salinity wastewater treatment with a reduced energy input.

5.5. REFERENCES

(1) Menzel, N.; Ortel, E.; Mette, K.; Kraehnert, R.; Strasser, P. Dimensionally stable Ru/Ir/TiO_2-anodes with tailored mesoporosity for efficient electrochemical chlorine evolution. *Acs Catalysis* **2013,** *3* (6), 1324-1333.

(2) Hu, W.; Wang, Y. Q.; Hu, X. H.; Zhou, Y. Q.; Chen, S. L. Three-dimensional ordered macroporous IrO_2 as electrocatalyst for oxygen evolution reaction in acidic medium. *Journal of Materials Chemistry* **2012,** *22* (13), 6010-6016.

(3) Mamaca, N.; Mayousse, E.; Arrii-Clacens, S.; Napporn, T. W.; Servat, K.; Guillet, N.; Kokoh, K. B. Electrochemical activity of ruthenium and iridium based catalysts for oxygen evolution reaction. *Applied Catalysis B-Environmental* **2012,** *111*, 376-380.

(4) Panizza, M.; Cerisola, G. Direct and mediated anodic oxidation of organic pollutants. *Chemical Reviews* **2009,** *109* (12), 6541-6569.

(5) Martinez-Huitle, C. A.; Ferro, S. Electrochemical oxidation of organic pollutants for the wastewater treatment: direct and indirect processes. *Chemical Society Reviews* **2006,** *35* (12), 1324-1340.

(6) Comninellis, C.; Vercesi, G. P. Characterization of DSA-type oxygen evolving electrodes - Choice of a coating. *Journal of Applied Electrochemistry* **1991,** *21* (4), 335-345.

(7) Lee, Y.; Suntivich, J.; May, K. J.; Perry, E. E.; Shao-Horn, Y. Synthesis and activities of rutile IrO_2 and RuO_2 nanoparticles for oxygen evolution in acid and alkaline solutions. *Journal of Physical Chemistry Letters* **2012,** *3* (3), 399-404.

(8) Alves, V. A.; Dasilva, L. A.; Boodts, J. F. C.; Trasatti, S. Kinetics and mechanism of oxygen evolution on IrO_2-based electrodes containing Ti and Ce acidic solutions. *Electrochimica Acta* **1994,** *39* (11-12), 1585-1589.

(9) Alves, V. A.; da Silva, L. A.; de Castro, S. C.; Boodts, J. F. C. Surface characterization by UHV techniques and cyclic voltammetry of thermal IrO_2-based electrocatalysts containing TiO_2 and CeO_2. *Journal of the Chemical Society-Faraday Transactions* **1998,** *94* (5), 711-717.

(10) daSilva, L. A.; Alves, V. A.; daSilva, M. A. P.; Trasatti, S.; Boodts, J. F. C. Oxygen evolution in acid solution on IrO_2+TiO_2 ceramic films. A study by impedance, voltammetry and SEM. *Electrochimica Acta* **1997,** *42* (2), 271-281.

(11) Chen, X. M.; Chen, G. H.; Yue, P. L. Stable Ti/IrO_x-Sb_2O_5-SnO_2 anode for O_2 evolution with low Ir content. *Journal of Physical Chemistry B* **2001,** *105* (20), 4623-4628.

(12) Chen, S. Y.; Zheng, Y. H.; Wang, S. W.; Chen, X. M. Ti/RuO_2-Sb_2O_5-SnO_2 electrodes for chlorine evolution from seawater. *Chemical Engineering Journal* **2011,** *172* (1), 47-51.

(13) Hansen, H. A.; Man, I. C.; Studt, F.; Abild-Pedersen, F.; Bligaard, T.; Rossmeisl, J. Electrochemical chlorine evolution at rutile oxide (110) surfaces. *Physical Chemistry Chemical Physics* **2010,** *12* (1), 283-290.

(14) Comninellis, C. Electrocatalysis in the Electrochemical conversion/combustion of organic pollutants for waste-water treatment. *Electrochimica Acta* **1994,** *39* (11-12), 1857-1862.

(15) Trasatti, S. Electrocatalysis in the anodic evolution of oxygen and chlorine. *Electrochimica Acta* **1984,** *29* (11), 1503-1512.

(16) Rossmeisl, J.; Qu, Z. W.; Zhu, H.; Kroes, G. J.; Norskov, J. K. Electrolysis of water on oxide surfaces. *Journal of Electroanalytical Chemistry* **2007,** *607* (1-2), 83-89.

(17) Santana, M. H. P.; De Faria, L. A. Oxygen and chlorine evolution on RuO_2+TiO_2+CeO_2+Nb_2O_5 mixed oxide electrodes. *Electrochimica Acta* **2006,** *51* (17), 3578-3585.

(18) Kronawitter, C. X.; Vayssieres, L.; Shen, S. H.; Guo, L. J.; Wheeler, D. A.; Zhang, J. Z.; Antoun, B. R.; Mao, S. S. A perspective on solar-driven water splitting with all-oxide hetero-nanostructures. *Energy & Environmental Science* **2011,** *4* (10), 3889-3899.

(19) Hoffmann, M. R.; Martin, S. T.; Choi, W. Y.; Bahnemann, D. W. Environmental applications of semiconductor photocatalysis. *Chemical Reviews* **1995,** *95* (1), 69-96.

(20) Kesselman, J. M.; Weres, O.; Lewis, N. S.; Hoffmann, M. R. Electrochemical production of hydroxyl radical at polycrystalline Nb-doped TiO_2 electrodes and

estimation of the partitioning between hydroxyl radical and direct hole oxidation pathways. *Journal of Physical Chemistry B* **1997,** *101* (14), 2637-2643.

(21) Gujar, T. P.; Shinde, V. R.; Lokhande, C. D.; Han, S. H. Electrosynthesis of Bi_2O_3 thin films and their use in electrochemical supercapacitors. *Journal of Power Sources* **2006,** *161* (2), 1479-1485.

(22) Yuan, D.; Zeng, J.; Kristian, N.; Wang, Y.; Wang, X. Bi_2O_3 deposited on highly ordered mesoporous carbon for supercapacitors. *Electrochemistry Communications* **2009,** *11* (2), 313-317.

(23) Shuk, P.; Wiemhofer, H. D.; Guth, U.; Gopel, W.; Greenblatt, M. Oxide ion conducting solid electrolytes based on Bi_2O_3. *Solid State Ionics* **1996,** *89* (3-4), 179-196.

(24) Tahar, N. B.; Savall, A. Electrochemical degradation of phenol in aqueous solution on bismuth doped lead dioxide: a comparison of the activities of various electrode formulations. *Journal of Applied Electrochemistry* **1999,** *29* (3), 277-283.

(25) Tomita, K.; Petrykin, V.; Kobayashi, M.; Shiro, M.; Yoshimura, M.; Kakihana, M. A water-soluble titanium complex for the selective synthesis of nanocrystalline brookite, rutile, and anatase by a hydrothermal method. *Angewandte Chemie-International Edition* **2006,** *45* (15), 2378-2381.

(26) Gao, Y. F.; Masuda, Y.; Peng, Z. F.; Yonezawa, T.; Koumoto, K. Room temperature deposition of a TiO_2 thin film from aqueous peroxotitanate solution. *Journal of Materials Chemistry* **2003,** *13* (3), 608-613.

(27) Van de Velde, N.; Arin, M.; Lommens, P.; Poelman, D.; Van Driessche, I. Characterization of the aqueous peroxomethod for the synthesis of transparent TiO_2 thin films. *Thin Solid Films* **2011,** *519* (11), 3475-3479.

(28) Kraft, A.; Stadelmann, M.; Blaschke, M.; Kreysig, D.; Sandt, B.; Schroder, F.; Rennau, J. Electrochemical water disinfection - Part I: Hypochlorite production from very dilute chloride solutions. *Journal of Applied Electrochemistry* **1999,** *29* (7), 861-868.

(29) Hanaor, D. A. H.; Sorrell, C. C. Review of the anatase to rutile phase transformation. *Journal of Materials Science* **2011,** *46* (4), 855-874.

(30) Ardizzone, S.; Bianchi, C. L.; Cappelletti, G.; Ionita, M.; Minguzzi, A.; Rondinini, S.; Vertova, A. Composite ternary SnO_2-IrO_2-Ta_2O_5 oxide electrocatalysts. *Journal of Electroanalytical Chemistry* **2006,** *589* (1), 160-166.

(31) Connor, P. A.; Dobson, K. D.; McQuillan, A. J. Infrared spectroscopy of the TiO_2/aqueous solution interface. *Langmuir* **1999,** *15* (7), 2402-2408.

(32) Hu, J. M.; Zhang, J. Q.; Cao, C. N. Oxygen evolution reaction on IrO_2-based $DSA^{(R)}$ type electrodes: kinetics analysis of Tafel lines and EIS. *International Journal of Hydrogen Energy* **2004,** *29* (8), 791-797.

(33) Zhang, J. J.; Hu, J. M.; Zhang, J. Q.; Cao, C. N. IrO_2-SiO_2 binary oxide films: Geometric or kinetic interpretation of the improved electrocatalytic activity for the oxygen evolution reaction. *International Journal of Hydrogen Energy* **2011,** *36* (9), 5218-5226.

(34) Kotz, R.; Stucki, S. Stabilization of RuO_2 by IrO_2 for anodic oxygen evolution in acid-media. *Electrochimica Acta* **1986,** *31* (10), 1311-1316.

(35) Cooper, K. R.; Smith, M. Electrical test methods for on-line fuel cell ohmic resistance measurement. *Journal of Power Sources* **2006,** *160* (2), 1088-1095.

(36) Hou, Y. Y.; Hu, J. M.; Liu, L.; Zhang, J. Q.; Cao, C. N. Effect of calcination temperature on electrocatalytic activities of Ti/IrO_2 electrodes in methanol aqueous solutions. *Electrochimica Acta* **2006,** *51* (28), 6258-6267.

(37) Zhou, X. L.; Ye, Z. G.; Hua, X. Z.; Zou, A. H.; Dong, Y. H. Electrocatalytic activity and stability of Ti/IrO_2 + MnO_2 anode in 0.5 M NaCl solution. *Journal of Solid State Electrochemistry* **2010,** *14* (7), 1213-1219.

(38) Xu, J. Y.; Liu, G. Y.; Li, J. L.; Wang, X. D. The electrocatalytic properties of an IrO_2/SnO_2 catalyst using SnO_2 as a support and an assisting reagent for the oxygen evolution reaction. *Electrochimica Acta* **2012,** *59*, 105-112.

(39) Hameed, A.; Montini, T.; Gombac, V.; Fornasiero, P. Surface phases and photocatalytic activity correlation of Bi_2O_3/Bi_2O_{4-x} nanocomposite. *Journal of the American Chemical Society* **2008,** *130* (30), 9658-+.

(40) Trasatti, S. Progress in the understanding of the mechanism of chlorine evolution at oxide electrodes. *Electrochimica Acta* **1987,** *32* (3), 369-382.

(41) Park, H.; Vecitis, C. D.; Hoffmann, M. R. Electrochemical water splitting coupled with organic compound oxidation: The role of active chlorine species. *Journal of Physical Chemistry C* **2009,** *113* (18), 7935-7945.

(42) Muff, J.; Bennedsen, L. R.; Sogaard, E. G. Study of electrochemical bleaching of p-nitrosodimethylaniline and its role as hydroxyl radical probe compound. *Journal of Applied Electrochemistry* **2011,** *41* (5), 599-607.

(43) Neta, P.; Huie, R. E.; Ross, A. B. Rate constants for reactions of inorganic radicals in aqueous-solution. *Journal of Physical and Chemical Reference Data* **1988,** *17* (3), 1027-1284.

(44) Pourbaix, M., *Atlas of electrochemical equilibria in aqueous solutions*. 2nd English ed.; National Association of Corrosion Engineers: Houston, Tex., **1974**.

(45) Sarma, B.; Jurovitzki, A. L.; Smith, Y. R.; Mohanty, S. K.; Misra, M. Redox-induced enhancement in interfacial capacitance of the titania nanotube/bismuth oxide composite electrode. *ACS Applied Materials & Interfaces* **2013,** *5* (5), 1688-1697.

(46) Kosmulski, M. Compilation of PZC and IEP of sparingly soluble metal oxides and hydroxides from literature. *Advances in Colloid and Interface Science* **2009,** *152* (1-2), 14-25.

(47) Shamaila, S.; Sajjad, A. K. L.; Chen, F.; Zhang, J. L. Study on highly visible light active Bi_2O_3 loaded ordered mesoporous titania. *Applied Catalysis B-Environmental* **2010,** *94* (3-4), 272-280.

(48) Bagwasi, S.; Niu, Y. X.; Nasir, M.; Tian, B. Z.; Zhang, J. L. The study of visible light active bismuth modified nitrogen doped titanium dioxide photocatlysts: Role of bismuth. *Applied Surface Science* **2013,** *264*, 139-147.

(49) Da Silva, L. M.; Boodts, J. F. C.; De Faria, L. A. Oxygen evolution at RuO_2(x) plus Co_3O_4(1-x) electrodes from acid solution. *Electrochimica Acta* **2001,** *46* (9), 1369-1375.

Chapter 6

OUTLOOK FOR THE FUTURE

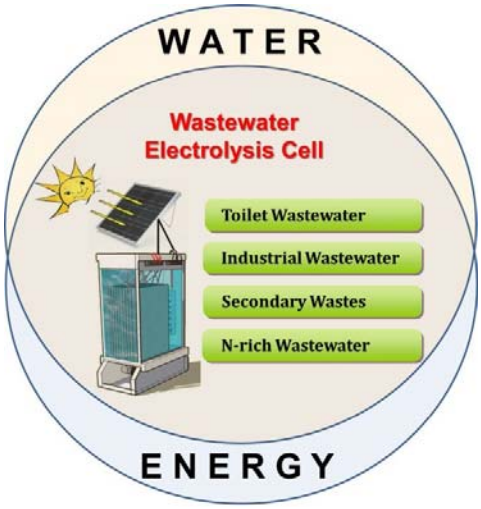

6.1. REACTION NETWORK IN WASTEWATER ELECTROLYSIS CELL

The wastewater electrolysis cell (WEC) for treatment of urea (Chapter 2[1]), domestic wastewater (Chapter 3[2]), and model toilet wastewater (Chapter 4[3]) showed evidence for the reaction pathway proposed in Figure 6.1. The higher oxide active sites on BiO_x/TiO_2 anode oxidize the Cl^- to RCS, which should be transported to bulk phase to oxidize organics to eventually CO_2. The ammonium ions (or other organic N-rich organics such as urea) are oxidized either to N_2 via breakpoint chlorination pathway or to nitrate ions by further oxidation of chloramines. The results in Chapter 2 and 3 demonstrated potential liberation of chlorine radicals ($Cl\cdot/Cl_2^{-}\cdot$) based on *iR*-compensated anodic potential (thermodynamic basis) and enhanced pseudo-first-order rate constants (kinetic basis).[1,2] Even under the generation of chlorine radicals in bulk phase, the contribution of free chlorine could not be

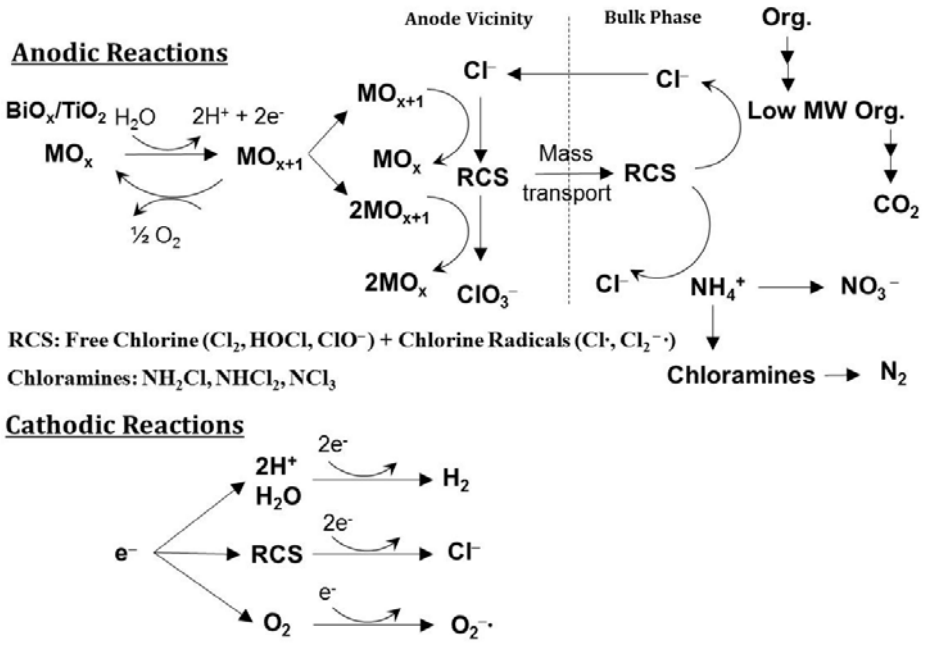

Figure 6.1. Reaction network in wastewater electrolysis cell.

ruled out, due to the facile disproportionation of chlorine radical to free chlorine. The speciation of electrochemically generated RCS was found to be primarily determined by the applied anodic potential and the chloride ion concentration, although a quantitative fractionation was beyond the scope of this study.

On the stainless steel cathodes, water and proton accept electrons to produce molecular hydrogen, while main scavenging reactions include reduction of RCS to chloride ion and molecular oxygen to superoxide radical. In particular, the reduction of RCS results in a null electrochemical cycle reducing the current efficiency both for the desired anodic (pollutants removal) and cathodic (molecular hydrogen generation) reactions.

A presumed facile transition of surface bound hydroxyl radical to higher oxide alleviated the contributions of direct oxidation on the multi-junction BiO_x/TiO_2 electrodes, prepared as in Table 1.1.[1-3] However, the electro-stationary surface concentration of hydroxyl radicals was greatly enhanced in the bilayer hetero-junction anode developed in this study (Chapter 5). Therefore, direct oxidation can be operative on the $Ir_{0.7}Ta_{0.3}O_y/Bi_xTi_{1-x}O_z$ anodes, as demonstrated by efficient degradations of the formate ion in 50 mM NaCOOH solutions (without chloride ion). With the presence of chloride ion, however, the overall reaction network would be still dominated by mediations of RCS, as in Figure 6.1. Since the molar concentrations of organics in domestic wastewater or human wastes would be much smaller than those of chloride ions, the direct oxidation of organics would be limited by mass transport. Nevertheless, significance enhancements in kinetic constants and current (energy) efficiency are expected when employing the $Ir_{0.7}Ta_{0.3}O_y/Bi_xTi_{1-x}O_z$ anodes in the wastewater electrolysis cell.

6.2. APPLICATION SCENARIOS OF THE WEC

6.2.1. Toilet Wastewater Treatment. Figure 6.2 shows an application scenario of a photovoltaic (PV) powered WEC system for treatment of wastewater from a public toilet in a developing world, based on the results in Chapter 4.[3] A volume balance estimated required the volume of the WEC to be 20 L for handling toilet wastewater from a 30 capita community. An existence of refractory organics in human excreta required a combination with biological pretreatment (septic tank). An energy balance for break-even 24 hours continuous operation predicted the area of the PV panel at 15 m^2. In more urbanized area, the WEC can also be connected to an existing electric grid, because the power requirement of the WEC operation (0.35 kW) is comparable with running household appliances.

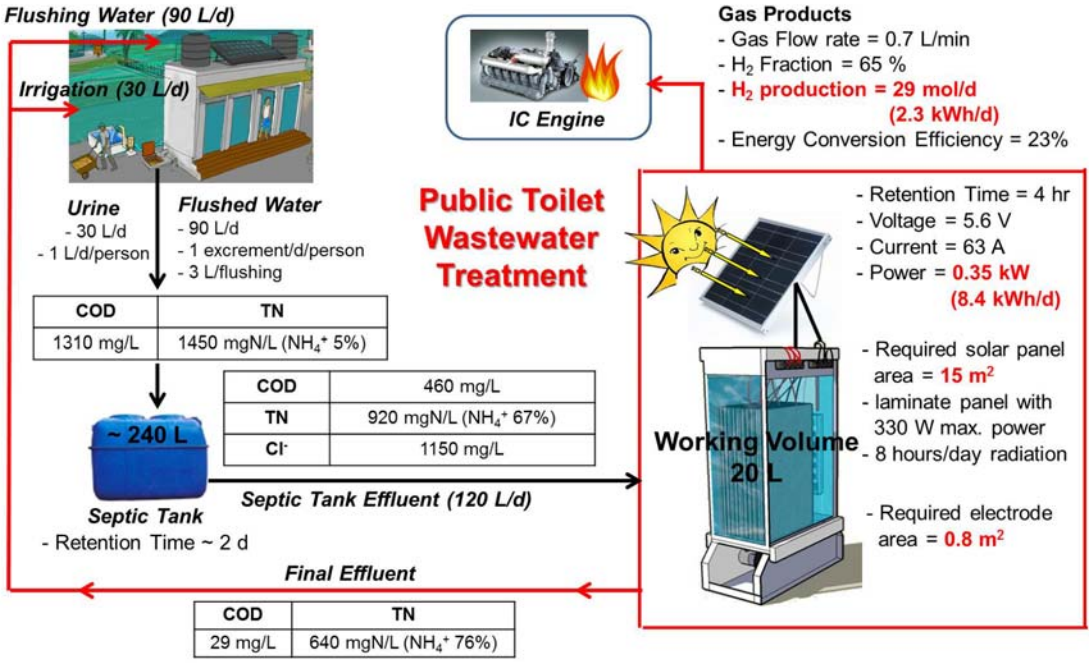

Figure 6.2. Application scenario of wastewater electrolysis cell for treatment of wastewater from a 30 capita public toilet.

US EPA[4] suggests reclaimed water quality for environmental reuse to satisfy BOD < 30 mg L^{-1}, total suspended solids (TSS) < 30 mg L^{-1}, coliform concentration < 200 CFU 100 mL^{-1}, and residual chlorine > 1 mg L^{-1}. The laboratory and scaled-up experiments (with hydraulic retention time less than 6 h) in Chapter 3 and 4 fully demonstrated the feasibility of effluent reuse for toilet flushing, irrigation, and stream flow recharge.[2,3] The mixed state molecular hydrogen produced with moderate levels of energy conversion efficiency can be utilized by running a H_2 internal combustion engine.

Consequently, beneficial contributions of the WEC are expected in terms of increased sanitation level, energy saving for wastewater delivery and treatment, alternative water resource by reusing effluents, and fuel production from water-splitting in select cases. When fully assembled a sufficient number of PV panels, a scaled-up PV-powered WEC should be easy to transport to various environments, including urbanized areas, peri-urban environments, and remote locations in the developing world that lack viable sanitation facilities.

6.2.2. Treatment of Other High Salinity Wastewater. The strong oxidation potentials of surface bound hydroxyl radicals and RCS make one envisage that analogous WEC setups can be used for treatment of various kinds of industrial wastewater and secondary waste from environment remediation facilities. Depending on the type of the wastewater, the WEC can be flexibly combined with other physical unit processes to boost the efficacy for remediation and energy storage.

One of the scenarios for industrial wastewater treatment is related with recent progress in Shale gas production. The current method of hydraulic fracturing results in a large

volume of wastewater (flowback water) which carries considerable amounts of suspended/dissolved solids, chloride ion, bromide ion, metals (Ca, Ba, and Sr), and oil/grease.[5,6] The brine wastewater has been usually treated by a municipal wastewater treatment plant, often causing a deterioration of effluent water quality due to the excessive pollutant loads. The high salinity of the flowback water should let the WEC suitable to an alternative treatment unit process, though the high solids concentration would require a pretreatment for solids/liquid separation. To this end, an electrochemical pretreatment unit with sacrificial anodes (Fe or Al metal) can provide an efficient solids/liquid separation by coagulation and flotation.[7] In this approach, the dissolving electrodes produce a range of coagulant species. The precipitates from charge neutralization and flocculation can be collected by sedimentation for a given duration or via collision with H_2 bubbles generated on the cathodes surface. Electrolysis is also a well-known technique for generating very fine gas bubbles at sizes smaller than 50 μm. It can be expected that the fine bubbles collide with and attach to the particles and float to the top of the reactor.[8] Therefore, so-called electroflotation merged with electrocoagulation (electro-coagulation-flotation, ECF) has been investigated for use in treatment of industrial wastewater.[7]

In addition, the WEC makes a perfect fit to treat the brine concentrate from reverse osmosis facilities for desalination or polishing effluents from wastewater or drinking water treatment plants.[9] The brine water generated in reverse osmosis of wastewater effluent contains biorefractory organics, chloride ion, and nitrate ion (as a byproduct of biological nitrification process). Although a reductive removal of nitrate was not investigated in this study, bimetallic cathodes (*e.g.*, Cu/Zn[10]) have been reported to show a strong activity for the reduction of nitrate ion to ammonium ion, which can be degraded to N_2, as thoroughly

discussed in Chapter 2.[1] The effluent from the WEC for treatment of the concentrates can be recycled back to the reverse osmosis unit, if potential chlorinated byproducts from the WEC are of significant concern. Based on the compatibility of the WEC with the reverse osmosis (or other filtration unit process such as nano-filtration), one can further imagine a compact and advanced wastewater treatment processes, which consists of an aerated bioreactor (converting organics to CO_2 and NH_4^+ to NO_3^-), a reverse osmosis for producing purified water, and the WEC to reduce the pollutant loadings of concentrated brine (converting biorefractory organics to CO_2 and NO_3^- to N_2).

The greater selectivity to N_2 in the electrochemical transformation of urea, as shown in Chapter 2,[1] allows for broader application of the WEC for remediation of N-rich wastewater (wastewater from livestock and fish-farm industry, landfill leachate, and anaerobic sludge digester effluents). The WEC is flexible enough to adjust the final products depending on the purposes; *i.e.*, an adjustment of current density or external reactive chlorine generation in a multi-component reactor can increase the yield of nitrate ion for fertilizer production.

6.3. REFERENCES

(1) Cho, K.; Hoffmann, M. R. Urea degradation by electrochemically generated reactive chlorine species: Products and reaction pathways. *Environmental Science & Technology* **2014,** *In Revision*.

(2) Cho, K.; Qu, Y.; Kwon, D.; Zhang, H.; Cid, C. A.; Aryanfar, A.; Hoffmann, M. R. Effects of Anodic Potential and Chloride Ion on Overall Reactivity in Electrochemical Reactors Designed for Solar-Powered Wastewater Treatment. *Environmental Science & Technology* **2014,** *48* (4), 2377-2384.

(3) Cho, K.; Kwon, D.; Hoffmann, M. R. Electrochemical treatment of human waste coupled with molecular hydrogen production. *RSC Advances* **2014,** *4* (9), 4596-4608.

(4) *Guidelines for water reuse*; EPA/600/R-12/618; United States Environmental Protection Agency: Washington, D.C., 2012.

(5) Warner, N. R.; Christie, C. A.; Jackson, R. B.; Vengosh, A. Impacts of Shale Gas Wastewater Disposal on Water Quality in Western Pennsylvania. *Environmental Science & Technology* **2013,** *47* (20), 11849-11857.

(6) Gregory, K. B.; Vidic, R. D.; Dzombak, D. A. Water Management Challenges Associated with the Production of Shale Gas by Hydraulic Fracturing. *Elements* **2011,** *7* (3), 181-186.

(7) Jiang, J. Q.; Graham, N.; Andre, C.; Kelsall, G. H.; Brandon, N. Laboratory study of electro-coagulation-flotation for water treatment. *Water Research* **2002,** *36* (16), 4064-4078.

(8) Cho, K.; Chung, C. M.; Kim, Y. J.; Hoffmann, M. R.; Chung, T. H. Electroflotation clarifier to enhance nitrogen removal in a two-stage alternating aeration bioreactor. *Environmental Technology* **2013,** *34* (19), 2769-2776.

(9) Bagastyo, A. Y.; Batstone, D. J.; Rabaey, K.; Radjenovic, J. Electrochemical oxidation of electrodialysed reverse osmosis concentrate on Ti/Pt-IrO2, Ti/SnO2-Sb and boron-doped diamond electrodes. *Water Research* **2013,** *47* (1), 242-250.

(10) Li, M.; Feng, C. P.; Zhang, Z. Y.; Shen, Z. L.; Sugiura, N. Electrochemical reduction of nitrate using various anodes and a Cu/Zn cathode. *Electrochemistry Communications* **2009,** *11* (10), 1853-1856.